

# Strong Magnon-Phonon Coupling in a Ferromagnetic Nanograting

Dissertation

zur Erlangung des akademischen Grades  
Doktor der Naturwissenschaften  
(Dr. rer. nat.)

vorgelegt  
der Fakultät Physik  
der Technischen Universität Dortmund

von

Felix Godejohann

Dortmund, 2020

Datum der Einreichung: Dortmund, 21. August 2020

Datum der Disputation: Dortmund, 10. December 2020

Prüfungskommission:

Prof. Dr. Manfred Bayer (1. Gutachter, TU Dortmund)

Prof. Dr. Andrew Rushforth (2. Gutachter, University of Nottingham)

Prof. Dr. Alexey V. Kimel (3. Gutachter, Radboud University Nijmegen)

Prof. Dr. Matthias Schneider

Priv.-Doz. Dr. Johannes Erdmann

# Abstract

The aim of this work is the development of a method to operate elementary spin excitations (magnons) in a ferromagnetic metal by means of elementary vibrational excitations of the lattice (phonons). The utilized magnon-phonon coupling was confirmed more than 50 years ago, but only recently the experimental approaches of ultrafast acoustics have made available the excitation and time-resolved detection of coherent phonons in the sub-THz frequency range. The most intriguing regime of the magnon-phonon coupling is the strong coupling regime, which guarantees a conversion of phonons to magnons and vice versa at unity fidelity. This regime is extremely difficult to achieve in ferromagnetic metals due to a typically weak magnon-phonon coupling and fast relaxation processes. In this work, we demonstrate a way to overcome these limitations and to achieve the regime of strong magnon-phonon coupling.

At first, the experimental setup is developed and assembled allowing the study of the magnon-phonon coupling in time domain. The state-of-the-art pump and probe setup is based on two femtosecond lasers synchronized in the scheme of asynchronous optical sampling and utilizes femtosecond laser pulses for excitation and monitoring coherent lattice and magnetic responses.

Secondly, we have thoroughly investigated a variety of coherent magnon dynamics in nanolayers of a ferromagnetic material called Galfenol (Fe,Ga), which possesses a large saturation magnetization and enhanced magnon-phonon coupling. We have demonstrated that a single magnon mode of a Galfenol nanolayer can have an effective Gilbert damping as small as 0.005 and frequencies higher than 100 GHz. In thick nanolayers, we are able to observe the small frequency splitting of exchange magnon modes, which is typically hidden in the transient signals due to quick dephasing.

At the third and main stage, we have utilized a lateral nanoscale patterning (nanograting) of a Galfenol nanolayer, in order to introduce two additional localized high-Q phonon modes ( $\sim 10$  GHz). By means of an in-plane external magnetic field, we control the frequency detuning between the magnon and phonons modes, while their spatial overlap is determined by the lateral pattern. We observe two bright manifestations of

---

the magnon-phonon coupling, i.e. resonant phonon driving and avoided crossing. The latter one clearly indicates the regime of strong magnon-phonon coupling with formation of a hybridized state known as magnon polaron. Theoretically, the magnon-phonon coupling is considered in the frame of coupled oscillators, whose coupling strength is determined by the spatial overlap of the interacting modes.

The presented experimental and theoretical results may aid in the development of energy-efficient transducers between magnonic and phononic systems.



# Zusammenfassung

Das Ziel der vorliegenden Forschungsarbeit ist die Entwicklung einer Methode, um elementare Spin-Anregungen (Magnonen) in ferromagnetischen Metallen mit Hilfe von elementaren Anregungen des Kristallgitters (Phononen) zu kontrollieren. Die verwendete Magnon-Phonon-Kopplung wurde zwar bereits vor 50 Jahren bestätigt; jedoch erst durch das Aufkommen der ultra-schnellen Akustik wurde es möglich, kohärente Phononen im sub-THz Bereich anzuregen und zeitlich aufgelöst zu messen. Das einflussreichste Regime der Magnon-Phonon-Kopplung ist das Regime der starken Kopplung, welches durch eine reversible Energiekonversion beider Systeme ausgezeichnet ist. Die Realisierung in ferromagnetischen Metallen ist jedoch extrem schwer, da diese eine schwache Magnon-Phonon-Kopplung und schnelle Relaxationsprozesse aufweisen. In dieser Arbeit zeigen wir, wie eine starke Kopplung dennoch erreicht werden kann.

Als erstes wurde ein Experiment entwickelt und aufgebaut, welches das Untersuchen der Magnon-Phonon-Kopplung im Zeitbereich ermöglicht. Das neuartige Anrege-Abfrage-Experiment besteht aus zwei Femtosekunden-Lasern, welche mit Hilfe des asynchronen optischen Abtastens (ASOPS) synchronisiert sind. Die Femtosekunden Laserpulse ermöglichen die Anregung und Detektion kohärenter Magnon- und Phonon-Dynamiken.

Als nächstes untersuchen wir Dynamiken von Magnonen in Nanometer-dicken Schichten bestehend aus einem ferromagnetischen Material namens Galfenol (Fe,Ga), welches sich durch eine große Sättigungsmagnetisierung und einer ausgeprägten Magnon-Phonon-Kopplung auszeichnet. Wir zeigen, dass eine einzelne Magnon-Mode in einer Galfenol-Nanoschicht einen effektiven Gilbert-Parameter von 0.005 und Frequenzen von mehr als 100 GHz haben kann. In dickeren Nanoschichten zeigen wir zudem die Frequenzaufteilung einzelner Magnon-Moden trotz derer schnellen Dephasierung.

Im Hauptteil verwenden wir eine Mikrometer-große Struktur (Nanogitter) in der Galfenol-Nanoschicht, um zwei langlebige Phonon-Moden ( $\sim 10$  GHz) mit spezifischen Polarisationen zu erzeugen. Mit Hilfe eines externen Magnetfeldes wird die Frequenzverstimmung zwischen lokalisierten Magnon- und Phonon-Moden kontrolliert, wobei die örtliche Überlappung der Moden durch das Nanogitter bestimmt ist. Im Experi-

---

ment messen wir zwei Manifestationen der Magnon-Phonon-Kopplung: die resonante Verstärkung durch Phononen und das sogenannte vermiedene Kreuzen. Letzteres zeigt das Regime der starken Magnon-Phonon-Kopplung und damit die Formation eines hybridisierten Zustandes, Magnon-Polaron genannt. Theoretisch wird die Magnon-Phonon-Kopplung im Modell gekoppelter harmonischer Oszillatoren untersucht, wobei die Kopplungsstärke durch den örtlichen Überlapp der gekoppelten Moden bestimmt ist.

Die experimentellen und theoretischen Resultate finden Anwendung in der Entwicklung von effizienten Energiewandlern zwischen magnonischen und phononischen Systemen.

# Contents

<b>1</b>	<b>Motivation</b>	<b>1</b>
<b>2</b>	<b>Theory of Transient Processes in Optically Excited Ferromagnetic Metal Layers</b>	<b>5</b>
2.1	Magnetic System . . . . .	6
2.1.1	Static Magnetization . . . . .	6
2.1.2	Landau-Lifshitz-Gilbert Equation . . . . .	10
2.2	Elastic System . . . . .	14
2.2.1	Static Strain and Stress . . . . .	14
2.2.2	Equation of Linear Elasticity . . . . .	17
2.3	Magneto-Elastic Coupling . . . . .	21
2.3.1	Static Magnetostriction . . . . .	21
2.3.2	Magneto-Elastic Waves in Bulk . . . . .	22
2.4	Model of Coupled Oscillators . . . . .	24
2.4.1	The Harmonic Oscillator . . . . .	24
2.4.2	Coupled Harmonic Oscillators . . . . .	25
<b>3</b>	<b>Experimental Setup and Preliminary Work</b>	<b>31</b>
3.1	Highly Magnetostrictive Galfenol (FeGa) . . . . .	32
3.2	Pump and Probe Setup using a Synchronized Laser System . . . . .	33
3.2.1	Pump and Probe Techniques . . . . .	33
3.2.2	The Laser System . . . . .	35
3.2.3	Experimental Realization using Two Different Excitation Geometries . . . . .	36
3.3	Preliminary Work . . . . .	41
3.3.1	Sample Characterization . . . . .	41
3.3.2	Optical Absorption Depth in Galfenol . . . . .	41
3.3.3	Comparison of Transient Reflection Measurements for Two Different Excitation Geometries . . . . .	42

<b>4</b>	<b>Optical Excitation of Multi- and Singlemode Magnetization Precession in Galfenol Nanolayers</b>	<b>47</b>
4.1	Sample Characterization . . . . .	48
4.2	Formation of Magnon Modes in Galfenol Nanolayers . . . . .	49
4.3	Observation of Multi-Mode Magnetization Precession in an Intermediate Galfenol Nanolayer . . . . .	51
4.4	Transition from Multi-Mode to Single-Mode Magnetization Precession in Galfenol Nanolayers . . . . .	56
4.4.1	Selective Excitation and Detection in Galfenol Nanolayers . . . . .	59
4.5	Characterization of Single-Mode Magnetization Precession in a 4 nm-thick Galfenol Nanolayer . . . . .	61
4.5.1	Observation of Brillouin oscillations in an Ultrathin Nanolayer . . . . .	66
<b>5</b>	<b>Strong Magnon-Phonon Coupling in a Ferromagnetic Nanograting</b>	<b>69</b>
5.1	Sample Characterization . . . . .	70
5.2	Localized Phonon Modes . . . . .	71
5.3	Characterization of Magnon-Phonon Resonances . . . . .	75
5.3.1	Experimental Evaluation of Unperturbed Phonon Lifetimes . . . . .	76
5.3.2	Selective Coupling of Optically Excited Magnon and Phonon Modes . . . . .	77
5.4	Angular Dependence of Localized Magnon Modes . . . . .	87
<b>6</b>	<b>Conclusion and Outlook</b>	<b>91</b>
	<b>List of Figures</b>	<b>95</b>
	<b>Bibliography</b>	<b>99</b>
	<b>Scientific Contributions</b>	<b>107</b>
	<b>Acknowledgments</b>	<b>109</b>
<b>A</b>	<b>Appendix</b>	<b>111</b>
A.1	Pump Pulse Characteristics . . . . .	111
A.2	MATLAB <sup>®</sup> Software for Remote Control and Data Analysis . . . . .	113
A.2.1	Software for Remote Control . . . . .	113
A.2.2	Software for Data Analysis . . . . .	115
A.3	Comparison of an Analysis in Time and Frequency Domain . . . . .	117
A.4	Analysis of Transient PMOKE Signals at 30, 110 and 140 mT . . . . .	118
A.5	Different Regimes of Coupling . . . . .	120
A.6	Polarization Dependence of the Reflection Signal . . . . .	121

# Chapter 1

## Motivation

The discovery of magnetism dates back more than 10 000 years ago. During this time, ancient Chinese and later ancient Greeks discovered a naturally occurring Iron oxide called magnetite, which can attract pieces of Iron. The following discovery that small fragments of magnetite automatically point to the direction of the (magnetic) north pole of the earth had a huge impact on ancient navigation and is known as a magnetic compass. Nowadays, the utilization of magnetic materials, especially the manipulation of the magnetization, is of crucial importance in our modern society. For almost 100 years, we have been utilizing magnetic materials for storing data, and until now the magnetic data recording remains dominant in information technology (IT) applications [1], [2], [3]. Despite the long and bright history of magnetic materials, many aspects of magnetism remain "terra incognita" for scientists. Hence, there is plenty of space for further research and development. A fundamental problem in processing large amounts of data is the accompanying huge energy consumption. This demands ultrafast and energy efficient manipulation of magnetic materials for high-density magnetic recording. Life sciences and medicine are rapidly exploring the nanometer scale ( $10^{-9}$  m) and, thus, require miniaturized sources of oscillating (ac) magnetic fields for magnetic imaging with highest possible resolution [4], [5] and <sup>1</sup>. Hence, there are many other demands and corresponding problems, which are in focus of modern magnetism.

Conventional magnetic applications utilize the steady state magnetization, while its motion of precession is considered only as a transient process accompanying the magnetization relaxation. Nowadays, the magnetization precession with characteristic frequencies in the GHz and sub-THz frequency range ( $10^9 - 10^{11}$  Hz) coincides with the frequency range for data transfer and data processing. Hence, it becomes a key tool for nanoscale magnetic concepts. For instance, the magnetization precession of a nanomagnet is a powerful source of an ac-magnetic field in free space [6]. Therefore, it is

---

<sup>1</sup>VIP+ project of the Bundesministerium für Bildung und Forschung - 'Realisierung eines Nanomagnetrons zur Erzeugung von sub-THz magnetischen Wechselfeldern für magnetische Resonanzspektroskopie - Nanomagnetron'

suggested as an assistant for ultra-high-density magnetic recording and high-resolution magnetic imaging. In a magnetic medium, the non-uniform precessing magnetization propagates in the form of a spin wave, whose elementary quantum is known as magnon. Spin waves/Magnons are considered as data carriers within a new direction of magnetism known as magnonics [7]. It is worth noting that the spin wave spectrum can be adjusted by spatial confinement with respective quantization [8], by the spatial periodicity of magnetic structures [9] as well as tuned by an external magnetic field. Thus, it provides magnon-based magnetic devices with very wide spectral tunability.

There are several ways to excite and control the magnetization precession, but energy-efficient and precise methods remain challenging for modern magnetism. The most used tool to control the magnetization is an external magnetic field. It can be an ultrashort (broadband) pulse, which tilts the magnetization rapidly out of its equilibrium orientation [10], or a monochromatic magnetic field of a microwave, which drives the magnetization precession at a certain frequency. The latter one is a basis for the technique of ferromagnetic resonance (FMR) being widely used for studying magnetic materials for more than 50 years. However, it is hardly adaptable for practical use at the nanoscale due to the need of bulky electromagnetic resonators and waveguides [11]. Hence, several alternative techniques have been rapidly developed within the last decade: The field of ultrafast optomagnetism utilizes ultrashort laser pulses, which instantly and locally affect the properties of a magnetic material [12]. The corresponding impact of the laser excitation on the magnetization may be considered as an ultrashort pulse of an internal "(magnetic) anisotropy field", which launches the precessional response of the magnetization. Another technique suitable for nanoscale applications utilizes a spin polarized current, which drives the magnetization precession, e.g. spin-transfer-torque nano-oscillators [6]. The main focus of this thesis is on the methods of ultrafast magneto-acoustics, which uses elementary vibrations of the crystal lattice (phonons) as a driving force for the magnetization precession [13], [14], [15], [16].

The coupling of the lattice and magnetization is known as magnetostriction since the discovery by James Joule in 1847 [17]. In 1958 Charles Kittel and a group of Soviet physicists predicted the effect of magneto-acoustic resonances (magnon-phonon resonances), when respective frequencies and wave vectors coincide [18], [19]. Later, the effect of magnon-phonon resonances was confirmed experimentally in ferrimagnetic garnets [20]. For a long time, these materials have remained the main object of magneto-acoustic studies due to a combination of low (accessible) magnon frequencies of several GHz and a weak damping for both magnons and phonons. Only recently the development of ultrafast acoustics made possible the extension of magneto-acoustic experiments to much higher frequencies with the aim to manipulate the magnetization precession in a much wider range of magnetic materials. Methods in the field of

---

ultrafast acoustics utilize femtosecond laser pulses for excitation of high-frequency coherent acoustic phonons in a form of a coherent wave packet (picosecond strain pulse) with frequencies of hundreds of GHz [21]. Phononic cavities and periodic structures, e.g. superlattices [14] and lateral gratings [15], [16], serve to filter out and spatially localize specific phonons with certain frequencies from the initially broadband excitation. Within the last decade, these methods were actively introduced into ultrafast and nanoscale magnetism. The magnetization precession excited by a picosecond strain pulse has been demonstrated in ferromagnetic semiconductors [22], ferromagnetic metals [21] and ferrimagnetic garnets [23]. Driving of the magnetization precession by monochromatic phonons has been realized in ferromagnetic phononic nanocavities [14], gratings [15], [16], and by means of spatially-modulated excitations (transient gratings) [24]. Nevertheless, these experiments have demonstrated only the one-way energy transfer from optically excited coherent phonons to coherent magnons. A reversible energy exchange between magnons and phonons is given by a formation of a hybridized state called a magnon polaron [25], [26]. The experimental evidence of the formation of a hybridized state still remains extremely challenging due to a typically weak magnon-phonon coupling and a quick dephasing of respective excitations at sub-THz frequencies<sup>2</sup>. The main motivation of this work is to overcome these limitations and to demonstrate the general approach suitable for a wide range of ferromagnetic materials including ferromagnetic metals, where these limiting factors are especially crucial.

The suggested approach is based on lateral patterning of a ferromagnetic structure, which localizes specific surface phonon and magnon modes and provides respective long lifetimes and spatial overlaps for a maximal efficient interaction. The ferromagnetic material chosen for the model experiment is a ferromagnetic metallic alloy of Iron and Gallium, known as Galfenol [28]. This novel functional material possesses enhanced magnon-phonon coupling and relatively long life times of excited magnon modes. At first, we characterize nanometer-sized layers made of Galfenol in order to demonstrate that the quick decay of the magnetization precession is due to dephasing of quantized magnon modes, where the ground magnon mode possesses the longest lifetime and a corresponding narrow spectral linewidth. Then, we examine the structure consisting of a lateral ferromagnetic nanograting (NG) produced by a focused ion beam in a Galfenol nanolayer. The introduced NG allows to achieve surface phonon modes with significantly long lifetimes. Spatial matching of the phonon and magnon modes determines the coupling strength and selects particular modes in the phonon and magnon spectra for hybridization [29]. The selective interaction allows us to solve the main problem of quick dephasing of the interacting excitations and to achieve sufficiently strong coupling. The experimental verification is realized by means of a state-of-the-art experimental setup for time-resolved detection of transient phonon and magnon

---

<sup>2</sup>The first observation of a magnon polaron in a metallic ferromagnet was reported last year [27].

kinetics.

The work at hand is organized as follows: Chapter 2 gives a general overview of the basic concepts used in ultrafast magneto-acoustics. Afterwards, the utilized all-optical pump and probe experiment is introduced in detail in chapter 3. This chapter also briefly discusses preliminary measurements, such as the optical penetration depth of the excitation pulse and the thermal transport in Galfenol nanolayers. Chapter 4 demonstrates a variety of optically excited precessional responses in Galfenol nanolayers. The nanolayers with varying layer thicknesses are characterized in section 4.1. The main experimental interest is in the dependence of magnetic responses on an in-plane applied magnetic field, which are discussed and modelled within the free energy density approach (sections 4.3 to 4.5). Chapter 5 presents magnon-phonon resonances of optically excited magnon and phonon modes in a shallow Galfenol NG. NG characteristics are introduced in section 5.1. The experimental observation of magnon polarons is given in section 5.3.2, where two magnon-phonon resonances are characterized separately and, finally, analyzed within the model of coupled harmonic oscillators. Afterwards in section 5.4, the magnetic field dependence of localized magnon modes is discussed for different angles of the in-plane applied external magnetic field. The last chapter 6 gives a brief conclusion and outlook of the main results in this work.



## Chapter 2

# Theory of Transient Processes in Optically Excited Ferromagnetic Metal Layers

This chapter will give a general overview of the basic concepts used in ultrafast magneto-acoustics. While the comprehension of the fundamentals of the magnetic (section 2.1) and acoustic system (section 2.2) is crucial for the understanding of more complicated physical phenomena, like the so-called magneto-elastic coupling (section 2.3 and 2.4) between them, it is also important to understand their ultrafast excitation and detection techniques. As written in the title, the reader will get an overview of the transient processes in optically excited ferromagnetic metal layers. So after finishing this chapter, the reader will understand, how the respective system is excited, how it develops in time and finally, how it is detected.

## 2.1 Magnetic System

In this study, we investigate magnetic nanostructures made of Galfenol, which is a ferromagnetic alloy of Iron and Gallium<sup>1</sup>. Galfenol is a crystalline metallic material, in which magnetic moments of magnetic ions are aligned by the exchange interaction mediated by free electrons. This type of exchange interaction is known as RKKY interaction and typical of all ferromagnetic metals, such as Iron, Nickel, Cobalt and many other alloys based on these materials [30]. At the used experimental conditions, the studied samples always remain far below Curie temperature and in the single-domain state. Thus, for description of the main magnetic properties we can use a continual approach, in which the magnetization,  $\mathbf{M}$ , i.e. the density of magnetic moments per unit volume, is a vector with a constant length equal to the saturation magnetization  $M_s$ . The equilibrium direction of  $\mathbf{M}$  is uniform or slightly varied inside the studied samples. Hence, it is convenient to utilize the normalized unit vector

$$\mathbf{m} = \frac{\mathbf{M}}{M_s} = \begin{pmatrix} m_x \\ m_y \\ m_z \end{pmatrix}. \quad (2.1)$$

### 2.1.1 Static Magnetization

Without any external influences and below Curie temperature, a ferromagnetic material is characterized by a spontaneous magnetization along certain directions of the crystal structure. In order to characterize the preferred magnetization directions, an applied external magnetic field  $\mathbf{B}$  is utilized. Figure 2.1 shows magnetization curves performed on Iron along different crystallographic directions. By applying an external magnetic field along a certain direction, the magnetization feels a torque towards the magnetic field direction. As it is seen in figure 2.1(a), the magnetization saturates for large magnetic fields, where the maximum value is determined by the saturation magnetization  $M_s$ . The non-isotropic magnetization curves in figure 2.1(a) arise due to the so-called magneto-crystalline anisotropy (MCA), which is introduced by the cubic lattice of Iron (see figure 2.1(b)). As it is seen in the figure, the energetically favourable direction for the magnetization is given by the [100]-crystallographic direction and is called easy magnetization axis (e.a.). The [111]-crystallographic direction indicates the least favourable direction and is referred to as hard magnetization axis (h.a.). Hence, in an anisotropic crystal the static magnetization tends to be directed along a certain direction.

---

<sup>1</sup>A detailed discussion about this material is given in section 3.1

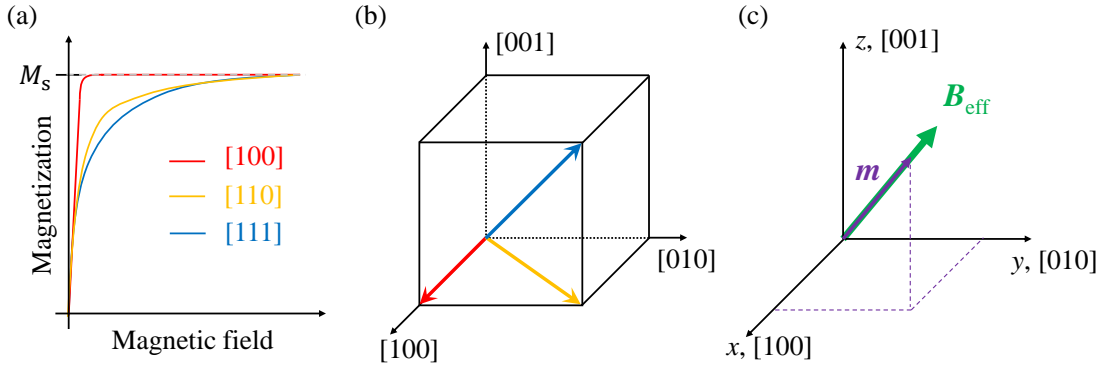


**Figure 2.1:** (a),(b) Magnetization curves for Iron along different crystallographic directions. The coloured arrows indicate the used magnetic field orientation. Adapted from [31]. (c) Used coordinate system containing an arbitrary effective magnetic field  $\mathbf{B}_{\text{eff}}$ , which determines the equilibrium direction of the magnetization  $\mathbf{m}$ .

In order to describe the equilibrium direction of the magnetization, a so-called effective magnetic field is introduced (see figure 2.1(c)): [32]

$$\mathbf{B}_{\text{eff}} = -\nabla_{\mathbf{m}} F(\mathbf{m}), \quad (2.2)$$

where  $F$  is the magnetic free energy density and

$$\nabla_{\mathbf{m}} = \begin{pmatrix} \frac{\partial}{\partial m_x} \\ \frac{\partial}{\partial m_y} \\ \frac{\partial}{\partial m_z} \end{pmatrix}. \quad (2.3)$$

In this work the free energy density (FED) is defined in magnetic units, i.e. in Tesla. With respect to the magneto-crystalline anisotropy shown in figure 2.1(a) a corresponding phenomenological magneto-crystalline term  $F_{\text{cubic}}$  to the FED can be defined. Under consideration of the crystal symmetry, the lowest, non-trivial solution of a serial expansion in  $m$  yields [33]

$$F_{\text{cubic}} = K_c(m_x^2 m_y^2 + m_y^2 m_z^2 + m_x^2 m_z^2), \quad (2.4)$$

where  $K_c$  is the cubic anisotropy coefficient in Tesla. In figure 2.2 the energy landscape of a material with  $K_c > 0$  is illustrated as an isosurface in three dimensions. The *holes* (energy minima) determine the favourable orientations of the crystal's magnetization (e.a.), e.g. the [100]-crystallographic direction. The *bumps* determine the least favorable orientations (h.a.), which are parallel to the room diagonals, e.g. the [111]-crystallographic direction. The physical origin of the MCA is explained by the spin-orbit interaction [34].

By introducing a certain shape to the ferromagnetic crystal, a shape anisotropy energy [32]

$$F_{\text{shape}} = -\mathbf{m} \cdot \mathbf{B}_{\text{demag}} \quad (2.5)$$

arises. The corresponding demagnetizing field  $\mathbf{B}_{\text{demag}}$  is determined by Maxwell's equations

$$\nabla_r \times \mathbf{B}_{\text{demag}} = 0, \quad (2.6)$$

$$\nabla_r \cdot (\mathbf{B}_{\text{demag}} + \mu_0 M_s \mathbf{m}) = 0, \quad (2.7)$$

where  $\mu_0$  is the vacuum permeability and

$$\nabla_r = \left( \begin{array}{c} \frac{\partial}{\partial r_x} \\ \frac{\partial}{\partial r_y} \\ \frac{\partial}{\partial r_z} \end{array} \right). \quad (2.8)$$

The shape anisotropy term can be arbitrarily complicated and will be important in chapter 5, where the case of nanogratings is considered. However, for thin films, where the surface normal is pointing in  $z$ -direction, the shape anisotropy term can be simply written as

$$F_d = B_d m_z^2 \quad (2.9)$$

and is characterized by the scalar demagnetizing field  $B_d = \frac{\mu_0 M_s}{2}$ . In equation 2.9, it can be seen that some energy is needed to move the magnetization  $\mathbf{m}$  out of the plane, i.e.  $m_z \neq 0$ . Therefore,  $\mathbf{m}$  is forced to lay in the layer plane, i.e.  $m_z = 0$ . Hence, the equilibrium static magnetization lies in the  $xy$  plane (see figure 2.3(a)).

In addition, thin ferromagnetic nanolayers are characterized by an in-plane uniaxial anisotropy, which increases with decreasing layer thickness [36]. Such in-plane uniaxial anisotropy is also typical of Gallenol nanolayers on GaAs substrates [37]. The FED of the uniaxial anisotropy reads

$$F_{\text{uniaxial}} = -K_u (\mathbf{m} \cdot \mathbf{s})^2, \quad (2.10)$$

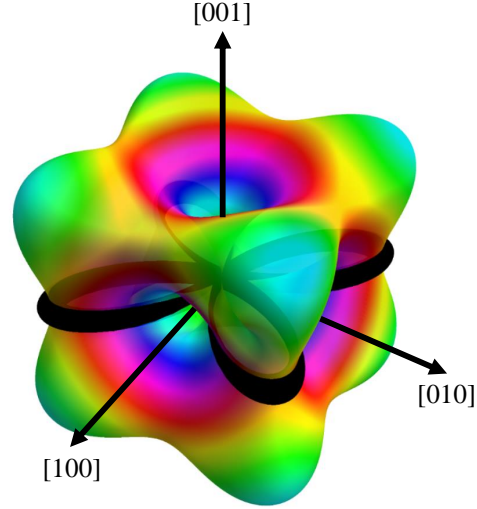


**Figure 2.2:** Visualization of an isosurface of the cubic anisotropy term in eq. 2.4 for  $K_1 > 0$ . Clearly indicated by the *holes* and *bumps* are the easy and hard axes of the ferromagnet. The black line shows the in-plane angular dependence of the energy surface possessing a four-fold symmetry. Adapted from [35].

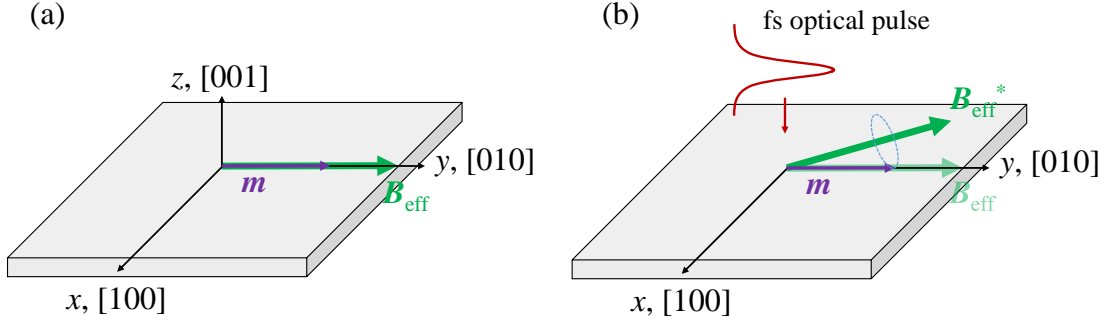


**Figure 2.3:** Excitation process of the magnetization precession in ultrathin ferromagnetic layers. (a) In the equilibrium the static magnetization  $\mathbf{m}$  lies along the effective magnetic field  $\mathbf{B}_{\text{eff}}$ , which is in the  $xy$  plane, eg. along the [010]-crystallographic direction. (b) After an instantaneous excitation, e.g. by an ultrashort optical pulse, a change of the equilibrium free energy density results in a new effective magnetic field  $\mathbf{B}_{\text{eff}}^* \approx \mathbf{B}_{\text{eff}}$ . For the sake of clarity, the in-plane change of  $\mathbf{B}_{\text{eff}}$  to  $\mathbf{B}_{\text{eff}}^*$  is exaggerated in this sketch. Due to the slow response of the magnetization on the introduced perturbation, a motion of precession around  $\mathbf{B}_{\text{eff}}^*$  is launched (blue circle).

where  $K_u$  is the uniaxial anisotropy coefficient and  $\mathbf{s}$  is a vector along an anisotropy direction. With respect to equation 2.10,  $\mathbf{s}$  determines energetically favorable orientations of  $\mathbf{m}$  parallel or anti-parallel to  $\mathbf{s}$ . The relative strength of the uniaxial anisotropy is given by  $K_u$ . In Galfenol nanolayers, the uniaxial anisotropy is typically smaller than the cubic anisotropy, i.e.  $K_u < K_c$  [38].

By applying an external magnetic field  $\mathbf{B}$ , another term given by the Zeeman energy

$$F_{\text{Zeeman}} = -\mathbf{m} \cdot \mathbf{B} \quad (2.11)$$

has to be considered.

In order to excite the magnetic system, the energy and, therefore, the effective magnetic field have to be perturbed out of their equilibrium. This can be realized by a modification of the magneto-crystalline anisotropy (MCA) via the absorption of a femtosecond (fs) optical pulse [12], [38]. In this case, temperature induced perturbations are characterized by changes of the cubic and uniaxial anisotropy coefficients  $\Delta K_c = \frac{\partial K_c}{\partial T} \Delta T$  and  $\Delta K_u = \frac{\partial K_u}{\partial T} \Delta T$ , respectively. Such a change in the MCA will lead to an in-plane change of  $\mathbf{B}_{\text{eff}}$  to the new effective magnetic field direction  $\mathbf{B}_{\text{eff}}^* \approx \mathbf{B}_{\text{eff}}$ , where the perturbation of  $\mathbf{B}_{\text{eff}}$  is assumed to be small; see figure 2.3(b). Due to the fact that the change of  $\mathbf{B}_{\text{eff}}$  is much faster than the reorientation of  $\mathbf{m}$ , the magnetization feels a

torque, which results in a damped motion of precession around  $\mathbf{B}_{\text{eff}}$ . Such dynamical response of the magnetization is described by the Landau-Lifshitz-Gilbert equation.

### 2.1.2 Landau-Lifshitz-Gilbert Equation

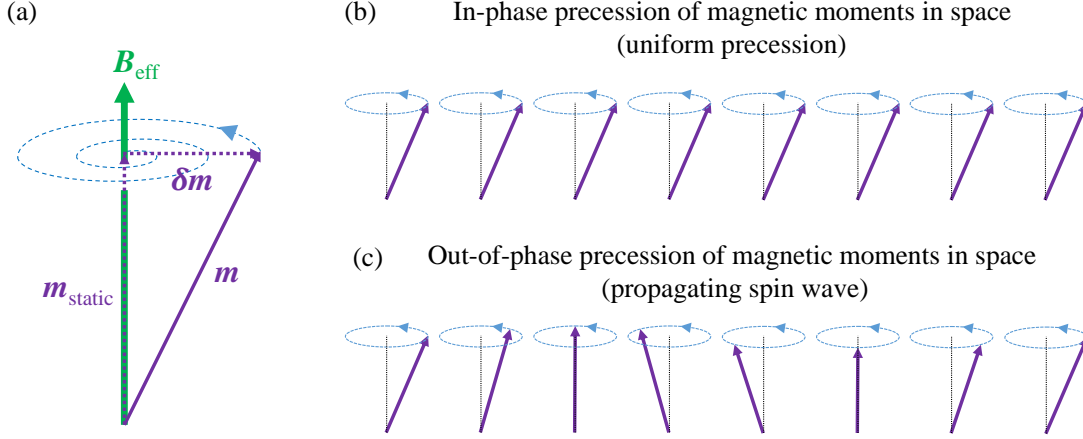


**Figure 2.4:** (a) Damped magnetization precession around the effective magnetic field  $\mathbf{B}_{\text{eff}}$ , where the static part of the magnetization is parallel to  $\mathbf{B}_{\text{eff}}$  and the dynamical part is perpendicular to  $\mathbf{B}_{\text{eff}}$ . (b) Uniform and (c) non-uniform magnetization precession. Latter is referred to as propagating spin wave.

In order to describe the transient response of the magnetization, the magnetization  $\mathbf{m} = \mathbf{m}_{\text{static}} + \delta\mathbf{m}$  is separated into a static part  $\mathbf{m}_{\text{static}}$  and a dynamical part  $\delta\mathbf{m}$ , where  $\delta\mathbf{m} \ll 1$  and, hence,  $\mathbf{m}_{\text{static}} \perp \delta\mathbf{m}^2$ . While the direction of the static part is determined by the direction of the effective magnetic field  $\mathbf{B}_{\text{eff}}$ , the overall kinetics of the magnetization is described by the Landau-Lifshitz-Gilbert (LLG) equation

$$\frac{d}{dt}\mathbf{m} = -\gamma'_e \mathbf{m} \times \mathbf{B}_{\text{eff}} + \alpha \mathbf{m} \times \frac{d}{dt}\mathbf{m}, \quad (2.14)$$

where  $\gamma'_e/2\pi \approx 28 \text{ GHz T}^{-1}$  is the gyromagnetic ratio of a free electron [39] and  $\alpha$  a unitless Gilbert damping parameter. An illustration of the damped motion of the dynamical magnetization is demonstrated in figure 2.4(a). The simplest motion of precession of an electron in a magnetic field  $B$  is known as Larmor precession and possesses the precession frequency  $\omega_L = \gamma'_e B$ , where  $\omega_L = 2\pi f_L$ .

---

2

$$\mathbf{m}^2 = \underbrace{\mathbf{m}_{\text{static}}^2}_{=1} + 2\mathbf{m}_{\text{static}} \cdot \delta\mathbf{m} + \underbrace{\delta\mathbf{m}^2}_{=0} \stackrel{!}{=} 1^2 \quad (2.12)$$

$$\Leftrightarrow \mathbf{m}_{\text{static}} \cdot \delta\mathbf{m} = 0. \quad (2.13)$$

The main interest in this work is on coherent responses of the magnetization, which is the collective motion of the magnetic moments. On the one hand, there is the uniform motion of all magnetic moments, which is known as ferromagnetic resonance (FMR) [40]; see figure 2.4(b). In magnetic layers with an in-plane applied magnetic field  $B$ , the precession frequency of the magnetic layer with saturation magnetization  $M_s$  is determined by the so-called Kittel formula [18]

$$\omega_{\text{Kittel}}(B) = \gamma'_e \sqrt{B(B + \mu_0 M_s)}. \quad (2.15)$$

On the other hand, nanometer-sized magnetic layers are characterized by the formation of spin waves (magnons) [8]. A spin wave is characterized by a fixed phase relation between each magnetic moment and is exemplarily illustrated in figure 2.4(c). The physical origin of the formation of spin waves is given by the RKKY interaction [30]. The RKKY interaction describes the coupling of d- or f-shell electron spins via conduction electrons. Therefore,  $\mathbf{m}$  holds a non-uniform distribution in space. For Iron, which possesses a body-centered cubic (bcc) lattice, the exchange free energy density can be written in a macroscopic approach as [32]

$$F_{\text{exchange}} = \frac{D}{2} [(\nabla_{\mathbf{r}} m_x)^2 + (\nabla_{\mathbf{r}} m_y)^2 + (\nabla_{\mathbf{r}} m_z)^2], \quad (2.16)$$

where  $D$  is the spin/exchange stiffness constant. Such exchange energy determines the precession frequency of spin waves according to  $\omega_m = \gamma'_e D k^2$  with spin wave vector  $\mathbf{k}$ . Hence, spin waves possess a quadratic dispersion relation. In case of plane spin waves, the dynamical magnetization can be written as

$$\delta \mathbf{m} = \delta \mathbf{m}_0 e^{i(\mathbf{k}\mathbf{r} - \omega_m t)}, \quad (2.17)$$

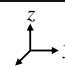
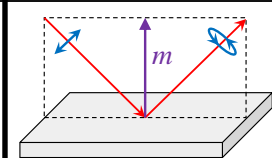
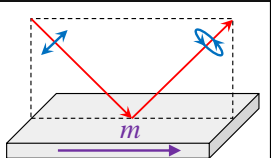
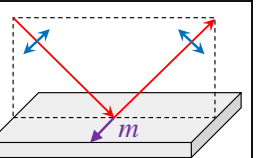
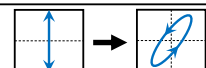
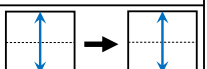
where  $\delta \mathbf{m}_0$  is the amplitude of the spin wave. The elementary quanta of spin waves are called magnons possessing an energy  $\hbar \omega_m$  and a linear momentum  $\hbar \mathbf{k}$ , where  $\hbar$  is the reduced Planck constant.

Damping mechanisms of the magnetization response are phenomenologically described by the Gilbert damping parameter  $\alpha$  in equation 2.14. A revealing discussion about overall magnon damping mechanisms is given in [41]. Considerable damping mechanisms in this work are the intrinsic spin-orbit coupling [42], eddy currents [43] and the extrinsic two-magnon scattering [44] and the presence of magnetic inhomogeneities [45]. The spin-orbit coupling is determined by the interaction of the electron's spin and its orbital momentum. This damping mechanism finally results in an energy transfer from the magnetic system to the lattice. The damping given by the spin-orbit coupling is especially a problem for magnetostrictive materials, where a strong spin-orbit coupling is wanted. Another important intrinsic damping mechanism is given by the formation

of eddy currents inside the magnetic material. This corresponding Gilbert damping parameter  $\alpha_{\text{eddy}} \propto h^2$  depends on the thickness of the magnetic layer  $h$  [41] and vanishes for the case of nanolayers, which are smaller than the skin depth, i.e.  $< 20$  nm for Iron [46]. An extrinsic damping mechanism is the two-magnon scattering, where a single magnon mode can scatter into two magnon modes and vice versa. The presence of magnetic impurities leads to an increased damping due to an increased dephasing of the magnetization precession by means of a non-uniformity of the magnetization distribution [47].

The detection of the magnetization precession in a metal can be realized optically by means of the magneto-optical Kerr effect (MOKE)[48]. Figure 2.5 illustrates three different methods for the detection of in- and out-of-plane magnetization components via a reflected optical beam. In the following, the sample's normal is directed along the  $z$ -direction. In figure 2.5(a) the polar MOKE (PMOKE) is presented, which detects the out-of-plane magnetization component ( $\delta m_z$ ) by means of a polarization rotation of the reflected beam. The change in polarization is described by the Kerr rotation angle

$$\theta_K(t) \propto \delta m_z(t). \quad (2.18)$$

Name	(a) Polar	(b) Longitudinal	(c) Transverse
 Geometry			
Detection	out-of-plane	in-plane	in-plane
Polarization change	Rotation/Ellipticity		None 
Measurement	Polarization change		Intensity change

**Figure 2.5:** Configurations for the detection of certain magnetization components via different MOKE. For all MOKE the geometry, the detected magnetization component and the influence on the probe light is shown. (a) The polar MOKE is characterized by a change of the probe pulse's polarization due to an out-of-plane magnetization component. (b) The longitudinal MOKE is also characterized by a change of the polarization plane, but detects the in-plane magnetization component perpendicular to the plane of incidence. (c) In contrast to the other MOKEs in (a) and (b), the transverse MOKE detects the in-plane magnetization component perpendicular to the plane of incidence via a change in the probe light's intensity. In case of a normal incidence of the probe pulse with respect to the sample's surface, only the PMOKE has a non-zero effect on the probe light. Adapted from [49].



The longitudinal MOKE (LMOKE) (see figure 2.5(b)) is also characterized by a rotation of the polarization plane, however, the in-plane magnetization component is detected, i.e.  $\delta m_{x,y}$ . The transverse MOKE (TMOKE), which is shown in figure 2.5(c), changes the reflected beam's intensity due to an in-plane magnetization component, i.e.  $\delta m_{x,y}$ .

In case of a normal-incident optical beam along the  $z$ -direction, only the PMOKE has to be considered. Due to a detection using a probe beam with finite optical absorption depth  $\zeta_{\text{pr}}$ , the actual detected magnetization in equation 2.18 is given by [38]

$$\delta m_z(t) = \int_0^d \delta m_z(z,t) e^{-\frac{z}{\zeta_{\text{pr}}}} dz. \quad (2.19)$$

For the investigation of the magnetization precession in nanostructures with arbitrary shapes, the simple relation shown in equation 2.18 is not valid anymore, so that the quadratic magneto-optical Kerr effect (QMOKE) has to be considered [50]. The QMOKE is characterized by a mixture of the shown MOKE in figure 2.5. Therefore, a reflected normal incident probe beam may not only be altered in its polarization, but also in its intensity.

## 2.2 Elastic System

Solid materials possess certain crystal structures, which determine well-defined atomic positions. In elastic materials, atoms are able to be reversibly displaced when being brought slightly out of their equilibrium positions. Such a reversible displacement is due to a back acting force on the displaced atom, which is described by Hooke's law. Due to a consideration of relative displacements with respect to equilibrium positions of the atoms, the so-called concept of strain is being used.

### 2.2.1 Static Strain and Stress

In general, the strain is a measure for the relative displacement to the equilibrium position of a certain particle in three dimensional space. When  $\mathbf{r}$  describes the particle's position and  $\mathbf{u}$  its displacement, displacement gradient elements  $\frac{\partial u_i}{\partial r_j}$  can be defined (see figure 2.6(a)). The symmetric part of the displacement gradient defines strain tensor elements for small displacements<sup>3</sup> [32]

$$\eta_{ij} = \frac{1}{2} \left( \frac{\partial u_i}{\partial r_j} + \frac{\partial u_j}{\partial r_i} \right), \quad i, j = x, y, z, \quad (2.20)$$

where the diagonal elements ( $i = j$ ) describe axial strain and the non-diagonal elements ( $i \neq j$ ) shear strain. The case of axial strain in an arbitrary slab is presented in figure 2.6(b), where the displacement is along the applied force (Cauchy strain).

In order to describe arbitrary forces across a certain unit area in three dimensions, a stress tensor can be defined, where its elements are given by

$$\sigma_{ij} = c_{ijkl} \eta_{kl}, \quad (2.21)$$

where  $c_{ijkl}$  are material dependent elasticity tensor elements. Figure 2.6(c) illustrates different stress tensor elements  $\sigma_{ij}$  acting on an infinitesimal cube in three-dimensional space. Regarding the elasticity tensor elements introduced in equation 2.21, a cubic crystal only possesses three different non-zero elements:  $c_{iiii} = c_{11}$ ,  $c_{iijj} = c_{12}$  and  $c_{ijij} = c_{44}$ , where  $i \neq j$  [32]. For materials discussed in this thesis the elasticity tensor elements are in the range of 100 GPa [52], [53].

With respect to the energy consideration in the previous section 2.1, also the stress

---

<sup>3</sup>The antisymmetric part of the displacement gradient, i.e.  $\frac{1}{2} \left( \frac{\partial u_i}{\partial r_j} - \frac{\partial u_j}{\partial r_i} \right)$ , defines rotations, which are not considered in this work.

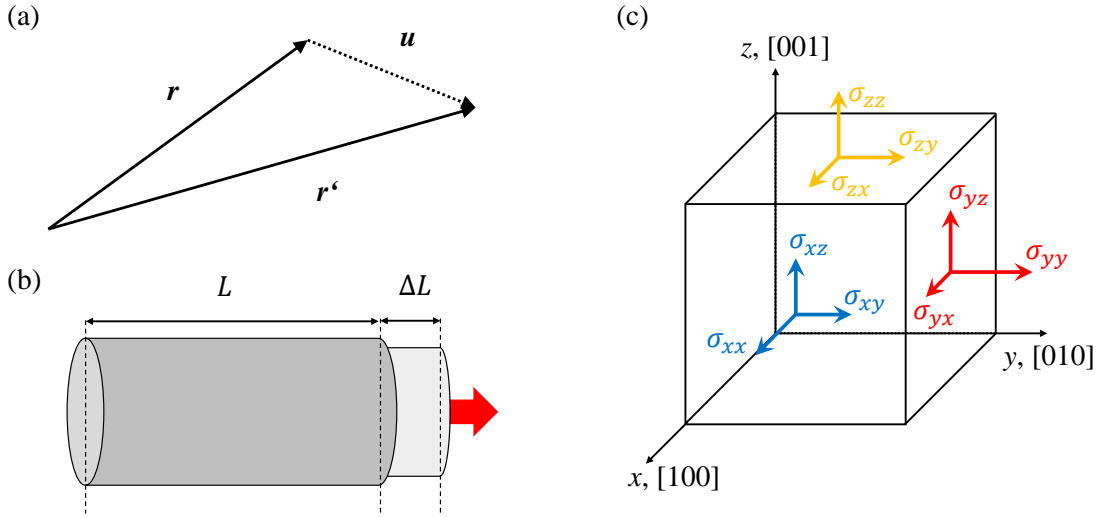


**Figure 2.6:** (a) Illustration of the displacement vector  $\mathbf{u}$  pointing from position  $\mathbf{r}$  to  $\mathbf{r}'$ . (b) Deformation of an arbitrary slab away from its equilibrium length  $L$  to a new length  $L + \Delta L$  due to an applied force (red arrow). The resulting strain reads  $\eta = \frac{\Delta L}{L}$  and is known as Cauchy strain. (c) Visualization of stress tensor elements  $\sigma_{ij}$  acting on an infinitesimal cube in three-dimensional space. Adapted from [51].

tensor elements in equation 2.21 can be described by an elastic free energy density  $F_{\text{el}}$  according to

$$\sigma_{ij} = \frac{\partial F_{\text{el}}}{\partial \eta_{ij}}. \quad (2.22)$$

The excitation out of equilibrium of the elastic system can be realized by means of temperature induced changes of the stress tensor elements. By considering a one-dimensional case along the  $z$ -direction, a thermal stress tensor element

$$\sigma_{zz}^{\text{th}} = -\beta_{\text{G}} C_1 T_1 \quad (2.23)$$

can be defined, where  $\beta_{\text{G}}$  is the Grüneisen parameter,  $C_1$  is the lattice heat capacity and  $T_1$  is the absolute lattice temperature.

In this work, the excitation out of equilibrium is realized by optical absorption of an ultrashort laser pulse by the electron system of a metallic layer [54] (see figure 2.7(a)). The laser pulse used for excitation is further referred to as pump pulse (see section A.1 for further information). The absorbed power of a normal-incident fs pump laser pulse with optical absorption depth  $\zeta_{\text{pu}}$ , energy density  $E_{\text{p,pu}}$  and pulse duration  $\tau_{\text{fs}}$  reads (see equation A.5)

$$P(z,t) = \sqrt{\frac{2}{\pi}} \frac{(1 - R_{\text{pu}}) E_{\text{p,pu}}}{\zeta_{\text{pu}} \tau_{\text{fs}}} \exp\left(-\frac{z}{\zeta_{\text{pu}}} - 2\frac{t^2}{\tau_{\text{fs}}^2}\right), \quad (2.24)$$

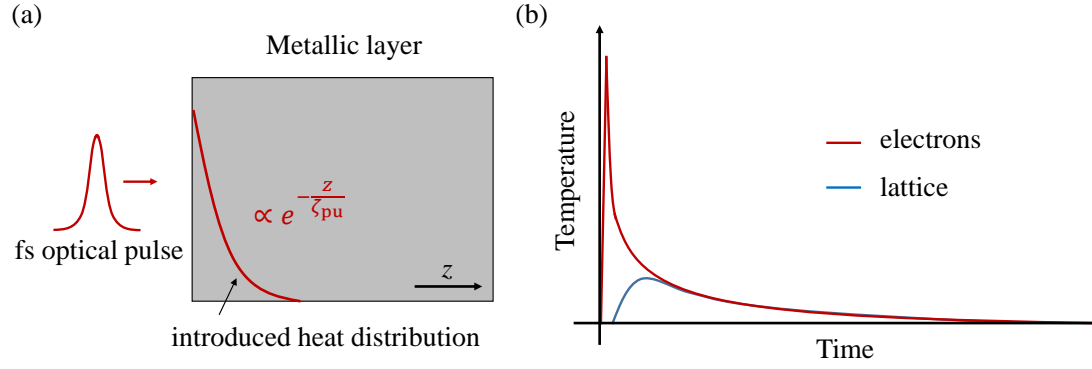


**Figure 2.7:** (a) Illustration of the absorbed fs pump pulse in a metal layer, which introduces a certain heat distribution inside the metallic layer. (b) Evolution of electron and lattice temperatures according to the two temperature model after an ultrafast excitation. Adapted from [56].

where  $R_{pu}$  is the pump pulse's reflection coefficient. Equation 2.24 can be assumed to be a  $\delta$ -like function in time. After the absorption and thermalization of the electrons via electron-electron scattering, the cooling of the electron system is realized by an energy transfer to the lattice [54]; see figure 2.7(b). Such energy transfer of the optically excited electrons to the lattice can be described by the two temperature model and can be written in the one-dimensional case along the  $z$ -direction as [55](Supplemental Material)

$$C_e \frac{\partial T_e}{\partial t} = \kappa_e \frac{\partial^2 T_e}{\partial z^2} - g(T_e - T_l) + P(z, t), \quad (2.25)$$

$$C_l \frac{\partial T_l}{\partial t} = g(T_e - T_l), \quad (2.26)$$

which determines the absolute temperatures of the lattice  $T_l$  and electrons  $T_e$ .  $C_e$  is the electron heat capacity,  $\kappa_e$  is the electron heat conductivity and  $g$  is the temperature-independent electron-lattice coupling factor. The fast energy transfer from the electron system to the lattice (several ps) results in a thermally induced stress

$$\sigma_{zz}^{th} = -\beta_G C_l T_l. \quad (2.27)$$

and, therefore, excites the elastic system out of its equilibrium.

### 2.2.2 Equation of Linear Elasticity

Using Hooke's and Newton's second law, the main equation of linear elasticity can be derived as [32]

$$\rho \frac{\partial^2 u_i}{\partial t^2} = \frac{\partial \sigma_{ij}}{\partial r_j} + \frac{\partial \sigma_{ij}^{\text{ex}}}{\partial r_j} \quad (2.28)$$

where  $\rho$  is the mass density and  $\sigma_{ij}^{\text{ex}}$  are external stress tensor elements. According to the excitation process discussed in the previous section, the only non-zero external stress tensor element is given by  $\sigma_{zz}^{\text{ex}} = \sigma_{zz}^{\text{th}}$  (equation 2.27).

The main equation of linear elasticity in equation 2.28 describes plane monochromatic elastic waves, whose displacement vector can be written as [32]

$$\mathbf{u}(\mathbf{r}, t) = \mathbf{u}_0(\mathbf{q}) e^{i(\mathbf{q}\mathbf{r} - \omega_{\text{ph}} t)} \quad (2.29)$$

where  $\mathbf{q}$  is the acoustic mode's wave vector. The modulation in time is described by the angular frequency  $\omega_{\text{ph}} = 2\pi f_{\text{ph}}$ , where  $f_{\text{ph}}$  is the frequency. The vector  $\mathbf{u}_0(\mathbf{q})$  describes the amplitude and polarization of the elastic wave. If  $\mathbf{u}_0$  is parallel or perpendicular to  $\mathbf{q}$ , the elastic wave is called longitudinal or transverse, respectively (see figure 2.8(a),(b)). The elementary quanta of elastic waves are called phonons possessing an energy  $\hbar\omega_{\text{ph}}$  and a linear momentum  $\hbar\mathbf{q}$ .

By considering the case of an isotropic medium and the limit of small wave vectors, i.e.  $q \ll 1$ , the sound velocities for pure longitudinal and transverse waves are  $v_l = \sqrt{\frac{c_{11}}{\rho}}$  and  $v_t = \sqrt{\frac{c_{44}}{\rho}}$ , respectively<sup>4</sup>. Next to longitudinal and transverse waves in bulk, elastic waves localized at the surface are of interest, as well. These types of waves were studied by Lord Rayleigh in 1885 and are known as surface acoustic waves (SAWs) or Rayleigh waves [57]. Rayleigh waves are characterized by an elliptic *rolling-like* particle movement, which consists of both longitudinal and transverse strain components; see figure 2.8(c). The amplitude of Rayleigh waves exponentially decreases with increasing distance from the surface (wave vector  $\mathbf{q}$  is complex). In chapter 5, spatial strain distributions of Rayleigh-like waves will be discussed in more detail in order to characterize certain localized modes inside a nanograting.

The experimental investigation of lattice dynamics in solids is realized by a change of the optical reflection coefficient and an accompanying change in the reflected intensity [59]. In case of a one-dimensional problem, which is sketched in figure 2.9,

<sup>4</sup>For an isotropic medium the non-zero elasticity tensor elements follow the relation,  $2c_{44} = c_{11} - c_{12}$  [32].

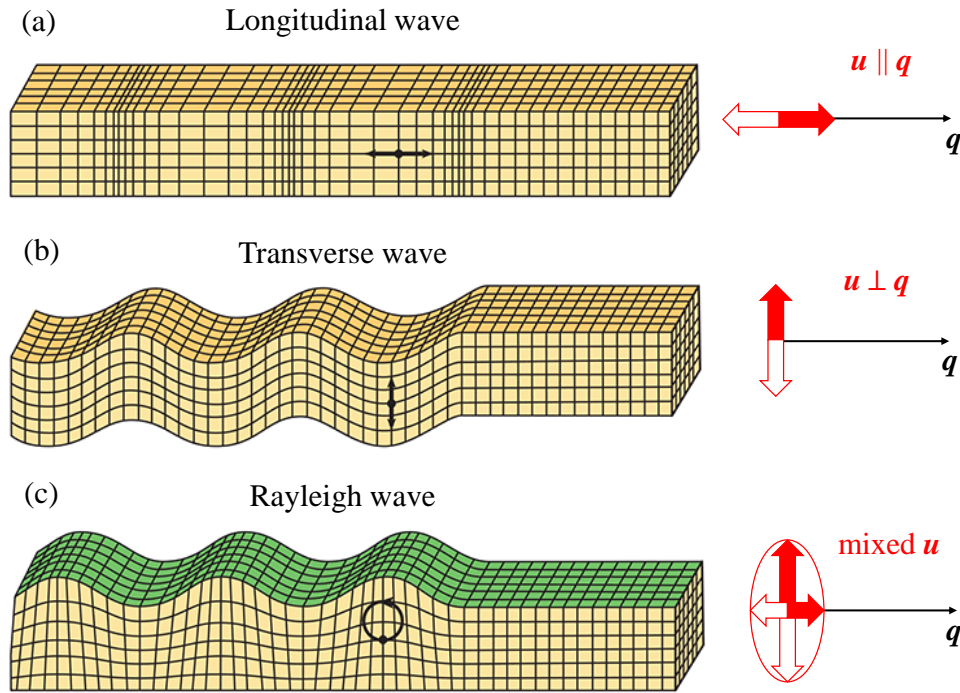


**Figure 2.8:** This figure illustrates different polarizations of elastic waves. (a) In case of a displacement, which is parallel to the direction of propagation, i.e.  $u \parallel q$ , the wave is called longitudinal. (b) If the displacement is perpendicular to the direction of propagation, i.e.  $u \perp q$ , the wave is called transverse. (c) In case of surface acoustic waves, so-called Rayleigh waves can be observed, which are characterized by an elliptical polarization with respect to the propagation direction. The green area indicates the surface. Adapted from [58].

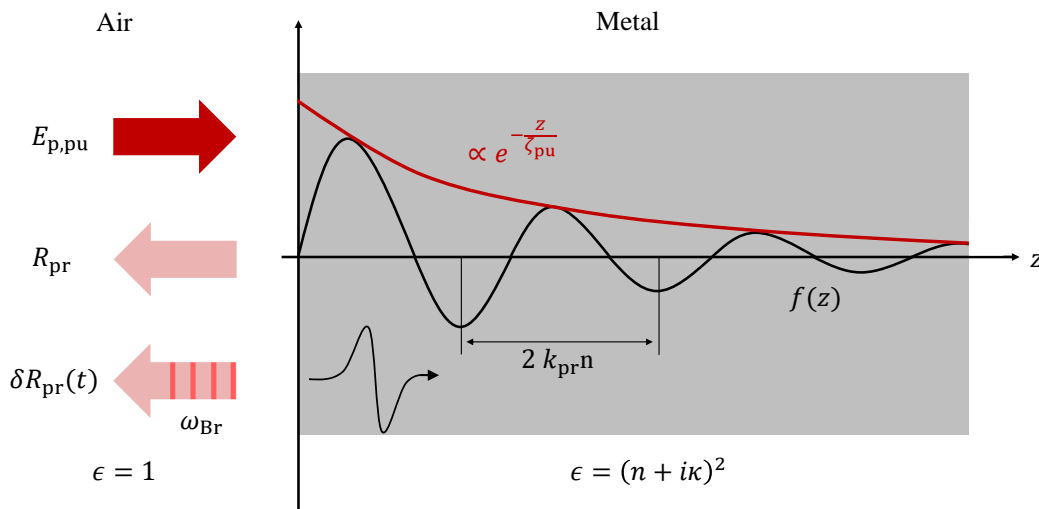


**Figure 2.9:** Detection of strain induced changes of an absorbed and reflected optical probe pulse in a metal. The spatial overlap of the strain and the sensitivity function (black graph) results in a change of the optical reflection coefficient  $\delta R_{pr}(t)$  with angular frequency  $\omega_{Br}$ . Characteristic features of the sensitivity function in equation 2.35 are indicated, as well.

the non-perturbed optical reflection coefficient of an optical laser beam (probe beam) between Air and a certain medium reads [60]

$$R_{\text{pr}} = \left| \frac{\bar{n} - 1}{\bar{n} + 1} \right|^2 = \left| \frac{\sqrt{\epsilon} - 1}{\sqrt{\epsilon} + 1} \right|^2, \quad (2.30)$$

where the permittivity

$$\epsilon = (n + i\kappa)^2 = \bar{n}^2. \quad (2.31)$$

depends on the complex refractive index  $\bar{n}$ .  $\bar{n}$  consists of the real refractive index  $n$  and the extinction coefficient  $\kappa = \frac{1}{2k_{\text{pr}}\zeta_{\text{pr}}} = \frac{\lambda_{\text{pr}}}{4\pi\zeta_{\text{pr}}}$ , where  $k_{\text{pr}} = \frac{2\pi}{\lambda_{\text{pr}}}$  is the probe light's wave number,  $\lambda_{\text{pr}}$  is the probe light's wavelength and  $\zeta_{\text{pr}}$  is the probe light's optical absorption depth. In three dimensions, the scalar permittivity introduced in equation 2.31 is a tensor with elements  $\epsilon_{ij}$ .

For any given strain components  $\eta_{ij}$  a perturbation of the equilibrium permittivity elements can be defined as [60]

$$\delta\epsilon_{ij} = \frac{\partial\epsilon_{ij}}{\partial\eta_{kl}}\eta_{kl} = p_{ijkl}\eta_{kl}, \quad (2.32)$$

where  $p_{ijkl}$  are complex photo-elastic tensor elements. For a cubic crystal there are only three non-zero elements:  $p_{iiii} = p_{11}$ ,  $p_{iijj} = p_{12}$  and  $p_{ijij} = p_{44}$ , where  $i \neq j$ .

Considering a one-dimensional scenario in  $z$ -direction, a non-zero  $\eta_{zz}$  perturbs the permittivity in equation 2.31 according to [59]

$$\delta\epsilon_{zz} = \frac{\partial\epsilon}{\partial\eta_{zz}}\eta_{zz} = 2(n + i\kappa) \left( \frac{\partial n}{\partial\eta_{zz}} + i \frac{\partial\kappa}{\partial\eta_{zz}} \right) \eta_{zz}, \quad (2.33)$$

where  $\frac{\partial n}{\partial\eta_{zz}}$  and  $\frac{\partial\kappa}{\partial\eta_{zz}}$  are photo-elastic coefficients. The perturbation of the permittivity results in a change of the probe pulse's optical reflection coefficient [59]

$$\delta R_{\text{pr}}(t) = \int_0^\infty f(z)\eta_{zz}(z,t)dz, \quad (2.34)$$

where the sensitivity function

$$f(z) = f_0 \left( \frac{\partial n}{\partial\eta_{zz}} \sin \left( \frac{4\pi n z}{\lambda_{\text{pr}}} - \phi \right) + \frac{\partial\kappa}{\partial\eta_{zz}} \cos \left( \frac{4\pi n z}{\lambda_{\text{pr}}} - \phi \right) \right) e^{-\frac{z}{\zeta_{\text{pr}}}}. \quad (2.35)$$

$f_0$  and  $\phi$  are the amplitude and the phase shift of the sensitivity function, which are defined in [59]. Equation 2.34 describes an overlap integral of the strain  $\eta_{zz}$  and the sensitivity function  $f(z)$ , where the sensitivity function describes properties of the probe

pulse; see figure 2.9.

Besides the excitation of coherent acoustic waves, the absorption of the fs pump pulse in equation 2.24 introduces a longitudinal bipolar strain pulse according to [60]

$$\eta_{zz}(z,t) = \eta_0 e^{-\frac{z}{\zeta_{pu}}} - \frac{\eta_0}{2} \left[ e^{-\frac{z+v_1 t}{\zeta_{pu}}} + e^{-\frac{|z-v_1 t|}{\zeta_{pu}}} \operatorname{sgn}(z - v_1 t) \right], \quad (2.36)$$

where  $\eta_0$  is the maximum strain amplitude, which is further defined in [60]. The ideal shape of the introduced strain pulse in equation 2.36 is rounded due to electron and thermal diffusion and the finite optical absorption depth of the probe pulse. A sketch of such strain pulse is found in figure 2.9. The excited strain pulse propagates along the  $z$ -direction through the sensitivity function of the probe pulse. The resulting transient change of the probe pulse's optical reflection coefficient can be written as [59]

$$\delta R_{pr}(t) \propto \cos(\omega_{Br} t - \phi') e^{-\frac{z}{\zeta_{pr}}}, \quad (2.37)$$

where the angular frequency

$$\omega_{Br} = \frac{4\pi n v_1}{\lambda_{pr}} \quad (2.38)$$

$$= 2k_{pr} n v_1. \quad (2.39)$$

describes so-called Brillouin oscillations and  $\phi'$  a phase shift. A sketch of the propagating strain pulse through the sensitivity function is given in figure 2.9.



## 2.3 Magneto-Elastic Coupling

### 2.3.1 Static Magnetostriction

The first identification of magnetostriction was experimentally done by James Joule in Iron samples in year 1847 [17]. The effect of magnetostriction is characterized by a volumetric change of a sample by means of an externally applied magnetic field [61]; see figure 2.10. For isotropic samples, a magnetostrictively induced strain  $\eta = \frac{\Delta L}{L}$  is described by a linear magnetostrictive constant

$$\lambda^{\text{ms}} = \frac{\Delta L}{L} = \eta. \quad (2.40)$$

For anisotropic samples in three dimensions, the magnetostrictive constant is a tensor with

tensor elements  $\lambda_{ij}^{\text{ms}}$ , which depend on the crystallographic direction. For saturated bcc Iron samples, the magnetostrictive constants along the [100]- and [111]-crystallographic directions are [62]

$$\lambda_{100} = 20.3 \cdot 10^{-6}, \quad (2.41)$$

$$\lambda_{111} = -21.1 \cdot 10^{-6}, \quad (2.42)$$

respectively. In terms of the free energy density approach, the magnetostrictive effect can be described by a magneto-elastic term according to [32]

$$F_{\text{m-el}} = b_1 \underbrace{(\eta_{xx}m_x^2 + \eta_{yy}m_y^2 + \eta_{zz}m_z^2)}_{\text{axial components}} + 2b_2 \underbrace{(\eta_{xy}m_xm_y + \eta_{yz}m_y m_z + \eta_{xz}m_x m_z)}_{\text{shear components}}, \quad (2.43)$$

where  $b_1$  and  $b_2$  are magneto-elastic constants for axial and shear strain, respectively. They are related to the magnetostrictive constants according to [63]

$$b_1 \propto \lambda_{100}(c_{11} - c_{12}), \quad (2.44)$$

$$b_2 \propto \lambda_{111}c_{44}, \quad (2.45)$$

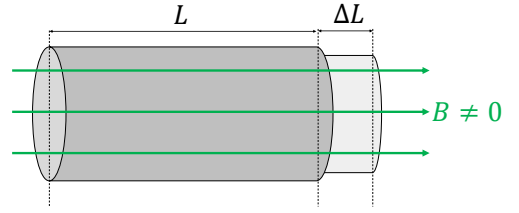


**Figure 2.10:** Illustration of the magnetostrictive effect. A magnetostrictive sample feels a strain  $\eta = \frac{\Delta L}{L}$  by means of an applied magnetic field. The introduced strain is described by a linear magnetostrictive constant  $\lambda^{\text{ms}} = \frac{\Delta L}{L}$ .

where  $c_{\alpha\beta}$  are the elasticity tensor elements, which have already been introduced in equation 2.21. Therefore, the influence of the magnetization on the lattice can be described by magneto-elastic stress tensor elements

$$\sigma_{ij}^{\text{m-el}} = \frac{\partial F_{\text{m-el}}}{\partial \eta_{ij}}. \quad (2.46)$$

### 2.3.2 Magneto-Elastic Waves in Bulk

By considering the Landau-Lifshitz-Gilbert (LLG) equation in 2.14 and the elastic equation of motion in 2.28, the introduced magneto-elastic stress in equation 2.46 results in a magneto-elastic coupling of both equations of motion. The simplest way to describe the formation of magneto-elastic waves is given by a bulk material, where only  $F_{\text{exchange}}$  (equation 2.16),  $F_{\text{Zeemann}}$  (equation 2.11) and  $F_{\text{m-el}}$  (equation 2.43) are considered. In the case of an externally applied magnetic field along the [100]-crystallographic direction, the dispersion relations for the coupled system can be written as [32]

$$\omega_1^2 - v_1^2 k^2 = 0, \quad (2.47)$$

$$(\omega_t^2 - v_t^2 k^2) (\omega_t \pm \omega_m) \pm \frac{\gamma'_e M_s b_2^2 k^2}{\rho \mu_0} = 0, \quad (2.48)$$

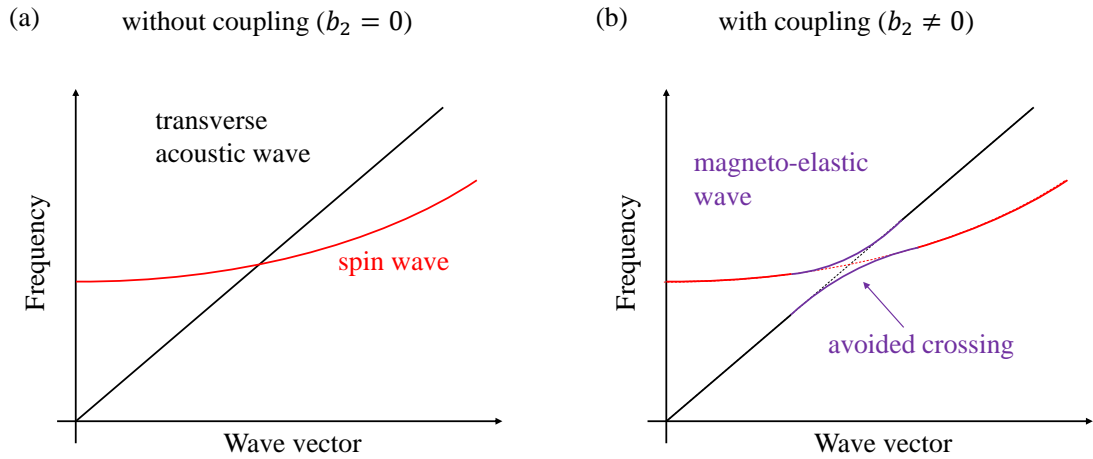
where  $\omega_{l,t}$  are angular frequencies of respective elastic waves and  $\omega_m = \gamma'_e B + \gamma'_e D k^2$  is the angular frequency of a spin wave. Equation 2.47 describes the dispersion relation of an uncoupled longitudinal ( $v_l$ ) elastic wave propagating along the magnetic field direction parallel to the [100]-crystallographic direction, i.e.  $\omega_1 = v_1 k$ . Equation 2.48 describes dispersion relations of coupled transverse ( $v_t$ ) elastic waves propagating along the same direction. These magneto-elastic waves are circularly polarized possessing opposite signs  $\pm$ . With respect to the direction of propagation, the signs correspond to clockwise and counter-clockwise polarized waves.

Figure 2.11 shows a sketch of the dispersion relations in equation 2.48 for an uncoupled<sup>5</sup> ( $b_2 = 0$ ) and coupled ( $b_2 \neq 0$ ) system. While the black and red dispersion curves illustrate uncoupled elastic and spin waves, the purple curves illustrate the dispersion relations of magneto-elastic waves. The cross section happens if both the modes' frequencies and wave vectors coincide. The coupling is indicated by an avoided crossing for the cross section of the uncoupled dispersion curves. The strength of the coupling and, therefore, the avoided crossing are determined by the magneto-elastic coefficient  $b_2$  in equation 2.48.

In the case of intermediate directions of the externally applied magnetic field, the previously uncoupled longitudinal elastic wave couples to the spin wave via the magneto-

<sup>5</sup>The dispersion relation in equation 2.48 becomes  $\omega_t = v_t k$ .

elastic constant  $b_1$ . Hence, dispersion relations arise, which contain both  $b_1$  and  $b_2$ . The resulting set of equations and corresponding dispersion relations can become arbitrarily complicated, especially when the material's shape is being modified. Therefore, a new approach is being utilized for the investigation of magnon-phonon coupling in ferromagnetic nanostructures.



**Figure 2.11:** Illustrative sketches of the dispersion relations for the cases of (a) uncoupled and (b) coupled elastic (black line) and spin waves (red line). For the case of a non-zero coupling coupled dispersion relations arise resulting in the formation of magneto-elastic waves (purple lines). An avoided crossing near the crossing point of both uncoupled dispersion relations is observed. Adapted from [32].

## 2.4 Model of Coupled Oscillators

A new approach for studying the magneto-elastic coupling was derived by Verba et al in 2018 [29]. They show mathematically that the magneto-elastic coupling is determined by the spatial overlap of the dynamical magnetization and the dynamical strain. They show that calculated spatial overlap integrals break down to a single number, which can be used as a coupling constant in the model of coupled harmonic oscillators. Hence, instead of the theoretical treatment of the coupled equations of motion, one only needs to know respective spatial profiles and has to calculate their overlap integrals. In order to have a direct relation between the frequency splitting of the avoided crossing and the coupling strength, the harmonic oscillator is described by a first-order differential equation. The following derivation is based on the explanation in [64].

### 2.4.1 The Harmonic Oscillator

A simple harmonic oscillator is given by a LC circuit, which is shown in figure 2.12(a). The first-order equations for the voltage  $V$  and current  $I$  are in Newton's notation [64]

$$V = LI\dot{\quad}, \quad (2.49)$$

$$I = -C\dot{V}, \quad (2.50)$$

where  $C$  describes the capacitor and  $L$  the inductor. These two coupled equations can be combined to a second-order differential equation of a harmonic oscillator [64]

$$\ddot{V} + \omega_0^2 V = 0, \quad (2.51)$$

$$\ddot{I} + \omega_0^2 I = 0, \quad (2.52)$$

where  $\omega_0^2 = \frac{1}{LC} = (2\pi f_0)^2$  describes the eigen angular frequency of the oscillating voltage and current. The transient voltage and current are described by oscillating functions, where both possess a  $\frac{\pi}{2}$ -phase shift to each other; see figure 2.12(b). By using this orthogonal relationship between the voltage and current, new complex amplitudes [64]

$$a_{\pm} = \sqrt{\frac{C}{2}} \hat{V} e^{\pm i\omega_0 t} \quad (2.53)$$

can be defined in the complex plane, where  $\hat{V}$  is the peak amplitude of the voltage.  $a_{\pm}$  describe positive- and negative-frequency components of the amplitude, where the energy in the circuit is given by  $W = |a_{\pm}|^2 = \frac{C}{2} |\hat{V}|^2$ . The introduced components of the amplitude result in two uncoupled first-order differential equations: [64]

$$\dot{a}_{\pm} = \pm i\omega_0 a_{\pm}. \quad (2.54)$$

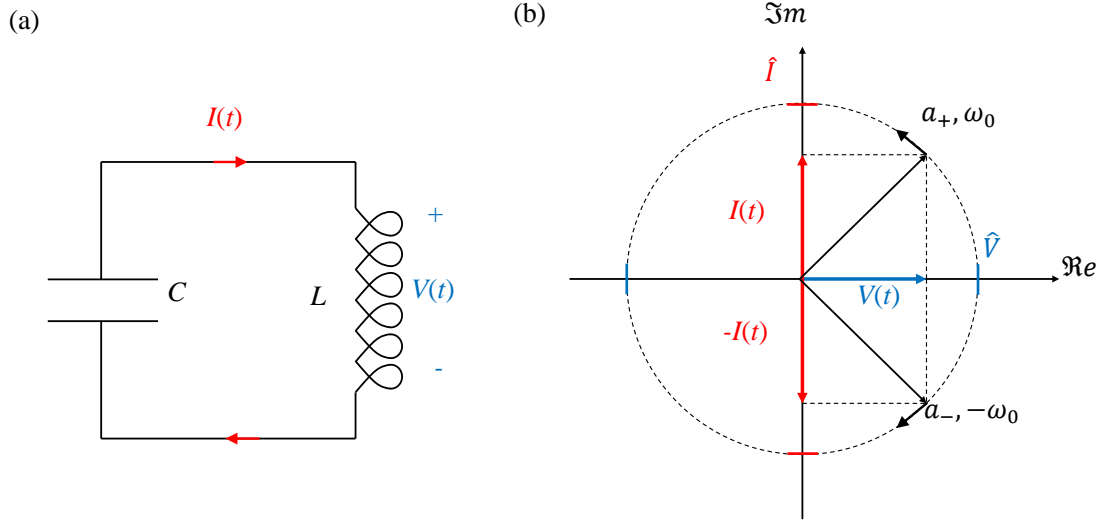


**Figure 2.12:** (a) Illustration of an LC circuit with capacitor  $C$  connected to an inductor  $L$ . The alternating voltage  $V(t)$  and current  $I(t)$  are indicated in red and blue, respectively. Adapted from [64]. (b) Visualization of the complex plane including the orthogonal functions for the voltage and current. The corresponding peak amplitudes are  $\hat{V}$  and  $\hat{I}$ . The newly defined amplitudes  $a_{\pm}$  and the corresponding frequencies  $\pm\omega_0$  are shown, as well.

For the further discussion of a system of coupled oscillators it is sufficient to consider only the positive-frequency component of the mode and the more intuitive frequency  $f_0 = \frac{\omega_0}{2\pi}$ , i.e.

$$\frac{1}{2\pi}\dot{a} - if_0a = 0. \quad (2.55)$$

### 2.4.2 Coupled Harmonic Oscillators

The coupling of two LC circuits, which are shown in figure 2.13(a), can be described by

$$\frac{1}{2\pi}\dot{a}_1 - if_1a_1 + iK_{12}a_2 = 0, \quad (2.56)$$

$$\frac{1}{2\pi}\dot{a}_2 - if_2a_2 + iK_{21}a_1 = 0, \quad (2.57)$$

where  $f_j = \frac{1}{2\pi\sqrt{L_jC_j}}$  defines respective eigen frequencies of the oscillators. The coupling constants  $K_{jl} = \frac{f_lC_K}{2\sqrt{C_jC_j}} \ll f_j$  describe weak perturbations of the two oscillators, which are given by the third capacitor  $C_K$  in figure 2.13(a)<sup>6</sup>.

<sup>6</sup>An example of a coupled mechanical system is given by two pendula, which are connected by a (weak) spring [65].

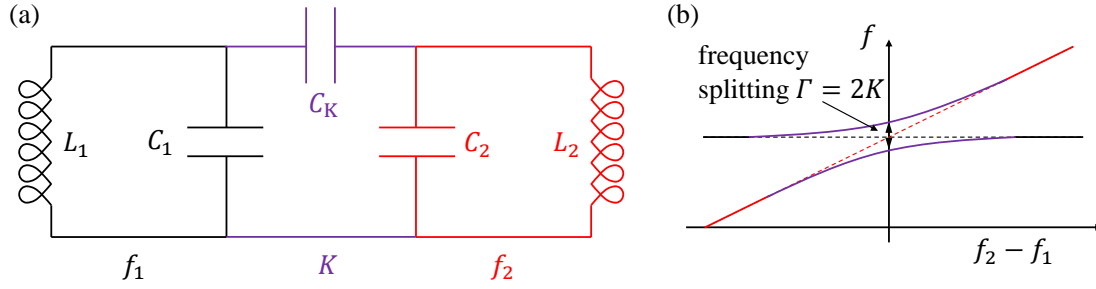


**Figure 2.13:** (a) Illustration of two symmetrically coupled LC circuits by means of a third capacitor  $C_K$ . The coupling constant, which is introduced by the third capacitor, is small compared to the eigen frequencies of the oscillators, i.e.  $K_{12} = K_{21} = K \ll f_{1,2}$ . (b) Sketched dispersion relations of uncoupled (black and red curves) and coupled (purple curves) oscillators. In this graph the frequency  $f_1$  is held constant, while the frequency  $f_2$  is linearly changed, where the crossing point is given by  $f_2 - f_1 = 0$ . According to the dispersion relation in equation 2.61, the coupled system results in an avoided crossing near the crossing point of the uncoupled oscillators.

In order to derive the dispersion relation of the coupled system, a Fourier transformation of equations 2.56 and 2.57 yield

$$if\tilde{a}_1 - if_1\tilde{a}_1 + iK_{12}\tilde{a}_2 = 0, \quad (2.58)$$

$$if\tilde{a}_2 - if_2\tilde{a}_2 + iK_{21}\tilde{a}_1 = 0, \quad (2.59)$$

where  $\tilde{a}_j(f) = \frac{1}{\sqrt{2\pi}} \int_{-\infty}^{\infty} dt e^{i2\pi ft} a_j(t)$ . This can be written in matrix notation as

$$\begin{pmatrix} i(f - f_1) & iK_{12} \\ iK_{21} & i(f - f_2) \end{pmatrix} \cdot \begin{pmatrix} \tilde{a}_1 \\ \tilde{a}_2 \end{pmatrix} = \begin{pmatrix} 0 \\ 0 \end{pmatrix}. \quad (2.60)$$

The dispersion relation for equation 2.60 is given by the zero-crossings of the characteristic polynomial and reads

$$(f - f_1)(f - f_2) = K_{12}K_{21}. \quad (2.61)$$

In resonance ( $f_1 = f_2 = f_0$ ) and for a symmetric coupling ( $K_{12} = K_{21} = K$ ), equation 2.61 reads

$$(f - f_0)^2 = K^2, \quad (2.62)$$

which, finally, yields the renormalized frequencies in resonance

$$f_{\pm} = f_0 \pm K. \quad (2.63)$$

As it can be seen in equation 2.63 and figure 2.13(b), the frequency splitting between both branches reads  $\Gamma = f_+ - f_- = 2K$ . This frequency splitting in resonance is also known as avoided crossing, where the purple curves in figure 2.13(b) show the avoided crossing for the coupled system. The same effect of avoided crossing can also be seen in figure 2.11(b) on page 23 for the case of magneto-elastic waves.

By considering an external excitation with amplitude  $A_j(t)$  of the  $j$ -th oscillator, equation 2.60 can be written as

$$\begin{pmatrix} i(f - f_1) & iK_{12} \\ iK_{21} & i(f - f_2) \end{pmatrix} \cdot \begin{pmatrix} \tilde{a}_1 \\ \tilde{a}_2 \end{pmatrix} = \begin{pmatrix} \tilde{A}_1 \\ \tilde{A}_2 \end{pmatrix}, \quad (2.64)$$

where  $\tilde{A}_j(f) = \frac{1}{\sqrt{2\pi}} \int_{-\infty}^{\infty} dt e^{i2\pi ft} A_j(t)$ . By using Cramers rule the spectral amplitudes of the coupled system can be calculated to

$$\tilde{a}_1(f) = \frac{\det \begin{bmatrix} \tilde{A}_1 & iK_{12} \\ \tilde{A}_2 & i(f - f_2) \end{bmatrix}}{\det \begin{bmatrix} i(f - f_1) & iK_{12} \\ iK_{21} & i(f - f_2) \end{bmatrix}} = \frac{i\tilde{A}_2 K_{12} - i\tilde{A}_1(f - f_2)}{(f - f_1)(f - f_2) - K_{12}K_{21}}, \quad (2.65)$$

$$\tilde{a}_2(f) = \frac{\det \begin{bmatrix} i(f - f_1) & \tilde{A}_1 \\ iK_{21} & \tilde{A}_2 \end{bmatrix}}{\det \begin{bmatrix} i(f - f_1) & iK_{12} \\ iK_{21} & i(f - f_2) \end{bmatrix}} = \frac{i\tilde{A}_1 K_{21} - i\tilde{A}_2(f - f_1)}{(f - f_1)(f - f_2) - K_{12}K_{21}}. \quad (2.66)$$

The discussed case of two coupled oscillators can be generalized to the case of  $j$  coupled oscillators. By considering coupling tensor elements  $K_{jl}$ , equations 2.56 and 2.57 can be generalized to

$$\frac{1}{2\pi} \dot{a}_j - if_j a_j + i \sum_l K_{jl} a_l = A_j. \quad (2.67)$$

In the case of exponentially damped oscillators (by means of some resistance in the circuits), time constants  $\tau_j$  can be defined, which describe the time when the respective amplitude is decreased to a factor of  $e^{-1}$  of the initial amplitude. The damping in time

corresponds to damping coefficients  $\gamma_j = \frac{1}{\tau_j}$ . Hence, equation 2.67 can be extended to [64]

$$\frac{1}{2\pi}\dot{a}_j - if_j a_j + \frac{\gamma_j}{2\pi} a_j + i \sum_l K_{jl} a_l = A_j. \quad (2.68)$$

By using the full width at half maximum (FWHM)  $\Delta f_j = \frac{\gamma_j}{\pi}$  of the spectral lines instead of the damping coefficients  $\gamma_j$  (see section A.3), equation 2.68 can be finally rewritten as

$$\frac{1}{2\pi}\dot{a}_j - if_j a_j + \frac{\Delta f_j}{2} a_j + i \sum_l K_{jl} a_l = A_j. \quad (2.69)$$

Due to the introduced spectral linewidth given by certain damping mechanisms, the observation of the frequency splitting may not be observable in the spectrum. Figure 2.14 illustrates two manifestations of coupled modes. In figure 2.14(a) the frequency splitting  $\Gamma = f_+ - f_-$  is larger than the respective linewidth  $\Delta f$  of the coupled modes resulting in an overall observed splitting in resonance. The resulting spectrum of the coupled modes is exaggeratedly sketched using a purple dotted line and clearly shows two separated peaks. In figure 2.14(b), however, the frequency splitting is less than the linewidth, which yields a combined spectrum possessing only one peak. Therefore, strongly coupled and weakly damped oscillating systems are needed for the observation of an avoided crossing.

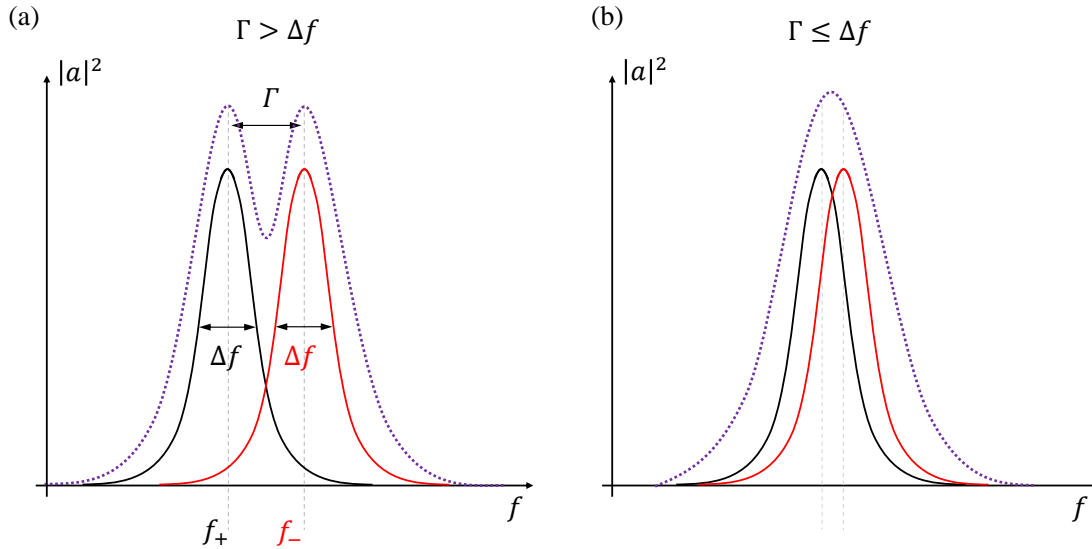


**Figure 2.14:** Illustrative sketches of different regimes of coupled oscillators. (a) Clearly resolved avoided crossing due to a frequency splitting  $\Gamma$ , which is larger than the linewidth  $\Delta f$  of both splitted modes with frequencies  $f_{\pm}$ , i.e.  $\Gamma > \Delta f$ . The exaggerated envelope (purple dotted line) sketches the overall spectrum containing both modes. (b) Hidden avoided crossing due to a small frequency splitting (or large linewidths) of both modes, i.e.  $\Gamma \leq \Delta f$ .



Quantitatively, the hybridization is described by the cooperativity

$$C = \frac{\Gamma^2}{\Delta f_1 \cdot \Delta f_2}, \quad (2.70)$$

where  $\Delta f_1$  and  $\Delta f_2$  are respective individual linewidths (FWHMs) of both interacting modes. The case of high cooperativity, i.e.  $C \gg 1$ , denotes the case of strong coupling, while a cooperativity  $C \approx 1$  corresponds to a moderate coupling regime. The different manifestations of a high or moderate cooperativity are also sketched in figure 2.14(a) and (b), respectively. An experimental evaluation of the coupling regime between specific magnon and phonon modes is given in chapter 5.



## Chapter 3

# Experimental Setup and Preliminary Work

This chapter will discuss the experimental part of this work. In section 3.1 the promising highly magnetostrictive material called Galfenol (Fe,Ga) will be introduced. The reader will get information about advantages of Galfenol compared to other magnetostrictive materials, e.g. Terfenol-D. The experimental setup is introduced in section 3.2 and contains information about transient pump and probe experiments for the detection of spin and lattice dynamics. Such transient tracing of the magnetization response is in contrast to the well-known ferromagnetic resonance (FMR) technique. The utilized state-of-the-art laser system is based on the asynchronous optical sampling (ASOPS) technique and enables the ability to detect oscillating signals in the complete GHz frequency range. In this manner, advantages of the ASOPS system are pointed out with respect to a conventional mechanical delay line. Finally, preliminary measurements are presented containing the evaluation of the optical absorption depth in Galfenol and the characterization of transient signals for two different excitation geometries.

### 3.1 Highly Magnetostrictive Galfenol (FeGa)

The strength of the magneto-elastic coupling in a certain material is determined by its magnetostrictive constants  $\lambda^{\text{ms}}$ ; see section 2.3.1. While the theoretical discussion in chapter 2 is mainly done for bulk Iron samples, the main experiments are performed on a highly magnetostrictive alloy of Iron (Fe) and Gallium (Ga) better known as Galfenol [28]. Galfenol possesses a large saturation magnetization  $\mu_0 M_s \approx 1.7 \text{ T}$  [67] and large Curie temperature  $T_C \approx 1000 \text{ K}$  [68]. The operation at room temperature is a huge advantage and enables the commercial usage of Galfenol-based devices. Galfenol was initially discovered by the Naval Surface Warfare Center (NSWC) Carderock in 1999 [68] and, nowadays, Galfenol-based devices can be found in a variety of applications, such as sensors and actuators [28].

As it is seen in figure 3.1, the amount of Gallium  $x$  in saturated Galfenol ( $\text{Fe}_{1-x}\text{Ga}_x$ ) samples alters both magnetostrictive constants  $\lambda_{100}^{\text{FeGa}}$  and  $\lambda_{111}^{\text{FeGa}}$ . Most of the shown measurements have been performed on furnace cooled and rapidly quenched Galfenol samples [66]. In this thesis  $\text{Fe}_{0.81}\text{Ga}_{0.19}$  samples are used, i.e.  $x \approx 19\%$ . The corresponding magnetostrictive constants are [66]

$$\lambda_{100}^{\text{FeGa}} \sim 200 \cdot 10^{-6}, \quad (3.1)$$

$$\lambda_{111}^{\text{FeGa}} \sim 20 \cdot 10^{-6}. \quad (3.2)$$

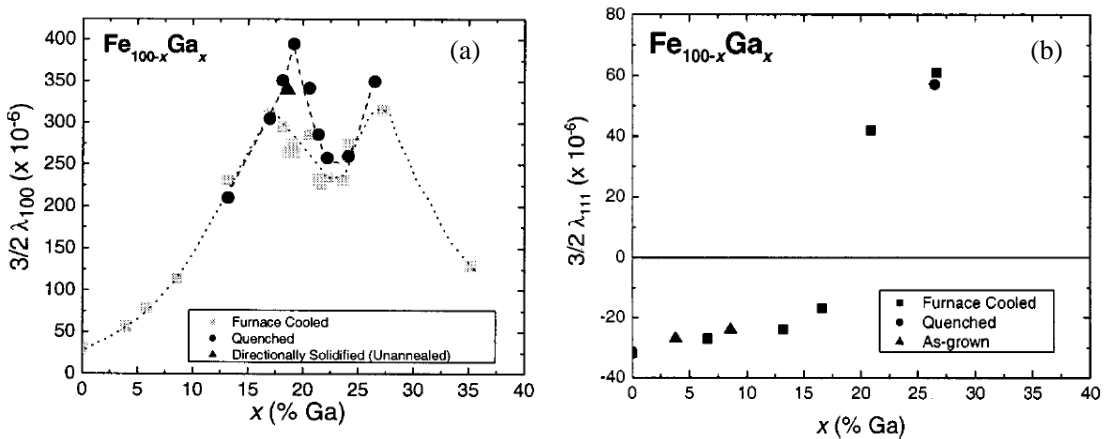


**Figure 3.1:** Magnetostrictive constants for different gallium concentrations. The measurements have been performed on furnace cooled and rapidly quenched Galfenol samples. Taken from [66].

In contrast to Terfenol-D (TbDyFe), which currently possesses the largest magnetostrictive constant

$$\lambda_{111}^{\text{TbDyFe}} > 1000 \cdot 10^{-6}, \quad (3.3)$$

Iron-based Galfenol has no drawbacks, like brittleness, high prices or the usage of rare-earth materials [69], [66],[70]. Another advantage of Galfenol compared to Terfenol-D is its small saturation field of several hundreds of mT [28].

In terms of the crystal structure, the increase of the amount of Gallium has impact on the cubic structure of Iron [71]. Therefore, not only the magnetostrictive constants change with the Gallium concentration, but also elastic and optical parameters. Such impact is further discussed in chapter 5.

## 3.2 Pump and Probe Setup using a Synchronized Laser System

### 3.2.1 Pump and Probe Techniques

The tracing of ultrafast dynamics of magnetic and elastic systems is performed by means of a pump and probe experiment. A conventional pump and probe setup consists of a pulsed laser beam, which is separated into two laser beams with the same repetition rate  $f_R$ . One laser beam is further referred to as pump beam and serves to excite the system out of equilibrium. The other laser beam is further referred to as probe beam and traces the dynamical response of the perturbed structure; see section 2.1 and 2.2. The time tracing is realized by means of a varying time delay  $\Delta t_R$  between the pulses of the pump and probe beam. Figure 3.2 illustrates such time delay, which is introduced by a variation of the optical path length of the probe beam by means of a mechanical delay line. The pump pulse is indicated in dark red and the varying probe pulses in red. A series of measurements at certain time delays results in a curve describing the dynamical response of a certain physical property (lower part of figure 3.2).

In contrast to the usage of a mechanical delay line, there is the asynchronous optical sampling (ASOPS) technique [72], [73]. The ASOPS technique is characterized by a synchronization of two pulsed laser beams with slightly different repetition rates  $f_i$ . One laser beam is denoted as master (usually the pump beam) and the other as slave (usually the probe beam). A synchronization unit, which detects both lasers, is used to realize a synchronization in time of a pump and probe pulse; see figure 3.3. The synchronization is realized electrically and is also used as a trigger source. The time

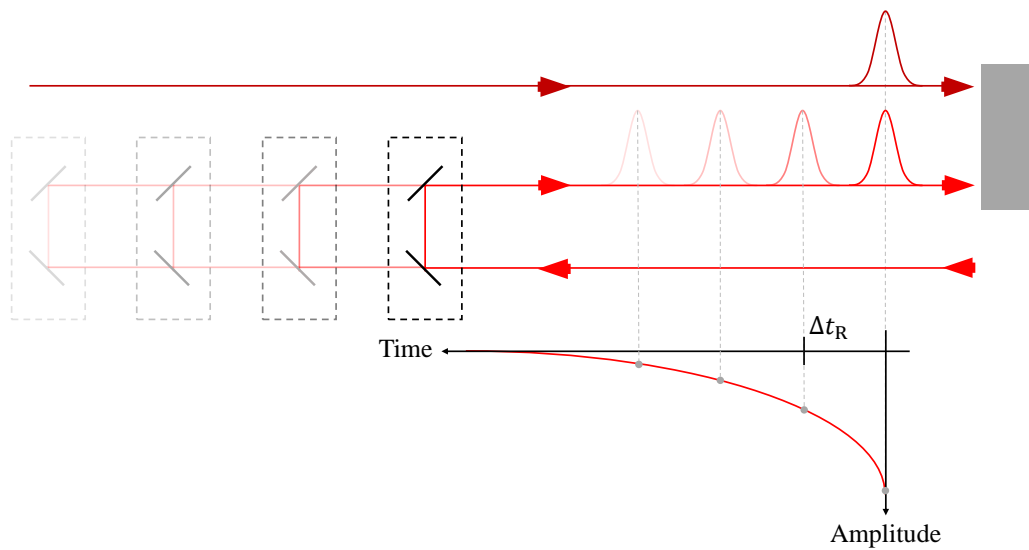


**Figure 3.2:** Illustration of a conventional pump and probe setup. A pulsed laser beam is separated into a pump beam (dark red) and probe beam (red). By varying the position of the mechanical delay line (vanishing box) the optical pulses in the probe beam are time delayed with respect to the pump pulse. The lower part of this figure illustrates that the detection of delayed probe pulses results in a graph, which traces the dynamics of a certain quantity, e.g. reflectivity.

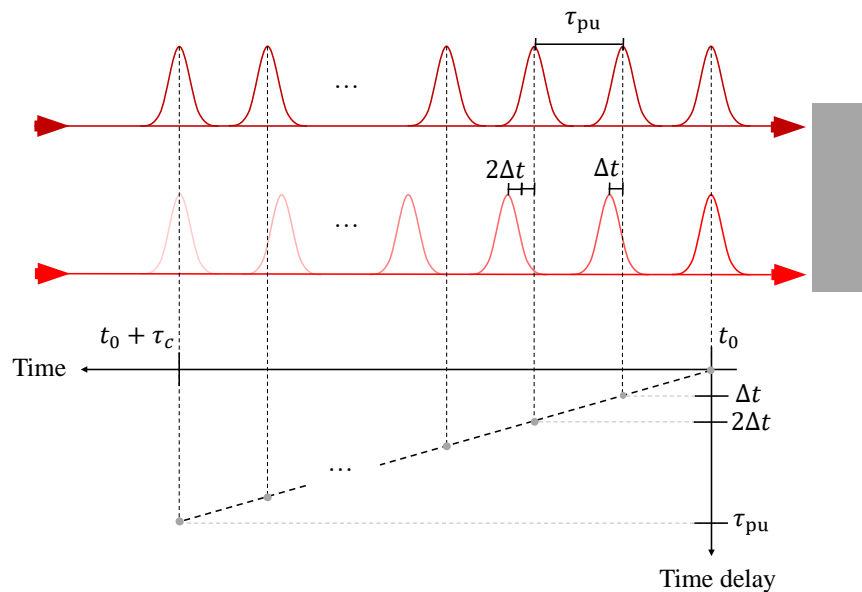


**Figure 3.3:** This figure shows an illustration of the ASOPS technique in a pump and probe setup. The time delay  $\Delta t$  is realized by an offset frequency  $f_o$  between the repetition frequencies of the pump and probe lasers. Hence, all probe pulses have fixed time delays to a the pump pulses. The time between two overlapping pulses is given by the circle time  $\tau_c = \frac{1}{f_o}$ .

delay  $\Delta t$  is introduced by means of slightly different repetition rates  $f_{\text{pu}}$ ,  $f_{\text{pr}}$  for the pump and probe beam, respectively and reads

$$\Delta t = \frac{f_o}{f_{\text{pu}}^2} \quad (3.4)$$

and is determined by the offset frequency  $f_o = f_{\text{pu}} - f_{\text{pr}}$ . Therefore, each probe pulse is delayed by a factor of  $\Delta t$  to the next pump pulse. The maximum delay time until the next transient overlap with a pump pulse is determined by the laser repetition rate/frequency. The number of time delays/pulses until the next overlap reads

$$N = \frac{f_{\text{pu}}}{f_o}. \quad (3.5)$$

The corresponding time for a so-called full circle is denoted as  $\tau_c = N \cdot \tau_{\text{pu}} = \frac{1}{f_o}$ . Therefore, it takes a time of  $\tau_c$  to measure the transient signal within the time window  $\tau_{\text{pu}}$ . This results in a scaling factor between the lab time and the real time. The scaling factor is the relation between the circle time and the repetition rates, i.e.  $\frac{\tau_c}{\tau_{\text{pu}}} = \frac{f_{\text{pu}}}{f_o} = N$ . Hence,  $N$  in equation 3.5 denotes the scaling factor between the lab and real time. The accumulation of many circles results in an increase of the signal-to-noise ratio.

### 3.2.2 The Laser System

The basic component for all experiments is given by a unique femtosecond fiber laser system produced by Toptica [73]. This laser system consists of two fiber lasers and a synchronisation unit (Laser Quantum) for the ASOPS technique. Both fiber lasers are Ti:Sa lasers with fixed wavelength at 780 nm (pulse width = 150 fs, maximal average power = 0.5 W) and 1045 nm (pulse width < 120 fs, maximal average power = 5 W), respectively. The repetition frequencies of the pump and probe lasers  $f_{\text{pu,pr}} \approx 80$  MHz ( $\tau_{\text{pu,pr}} \approx 12.5$  ns) and are remotely adjustable by changing the fibers' temperatures and, therefore, their lengths. The adjustable temperature range between both lasers is roughly 20 °C resulting in a maximum offset frequency of roughly 10 kHz ( $\tau_c \approx 0.1$  ms).

Technically, the synchronization is realized by having the probe laser as master ( $f_{\text{pr}}$ ) and the pump laser as slave ( $f_{\text{pu}} = f_{\text{pr}} - f_o$ ), which means that the pump pulses are delayed with respect to the probe pulses. A variation of the pump pulse is preferred, because a varying probe pulse could lead to an additional contribution to the measured signal. The maximum time window for transient measurements is given by the repetition rate  $\tau_{\text{pr}} = \frac{1}{80 \text{ MHz}} = 12.5$  ns. In this work an offset frequency of  $f_o = 800$  Hz is used, which corresponds to a relative time delay  $\Delta t \approx \frac{800 \text{ Hz}}{(80 \text{ MHz})^2} = 0.125$  ps (equation 3.4). Therefore, one complete circle consists of  $N \approx \frac{80 \text{ MHz}}{800 \text{ Hz}} = 10^5$  data points (equation 3.5) and has a duration  $\tau_c = \frac{1}{800 \text{ Hz}} = 1.25$  ms. Hence, there is a scaling factor of  $10^5$  between the real time (12.5 ns) and the lab time (1.25 ms =  $10^5 \cdot 12.5$  ns).

It should be emphasized that almost immediate measurement of the whole transient signal within several milliseconds is the main advantage of the ASOPS technique. It gives the ability to adjust the signal on the fly, because for experiments done in this work an accumulation of several 100 ms (80 circles) is enough to get a clean signal with a reasonable signal to noise ratio. This opens possibilities to observe the behaviour of a signal with changing different parameters, e.g. the magnetic field, sample position, position of the pump spot or the laser intensity. After optimizing all parameters in *live mode*, an averaging is needed to significantly reduce the noise level of the signal. Due to the very low relative noise level of the laser power, it is possible to achieve publishable signals within 5 min of averaging. Therefore, this type of pump and probe technique is much faster and less noisy than using a mechanical delay line.

However, one disadvantage may be the fixed repetition rate of 12.5 ns. In this case, it is only possible to investigate transient phenomena happening within this time range. Fortunately, there are laser systems available, which have adjustable repetition rates, so that pump and probe experiments with different time windows are possible, as well [74]. Besides adjustable repetition rates, it is also possible to reduce the repetition rate of the laser system by means of a pulse picker.

### 3.2.3 Experimental Realization using Two Different Excitation Geometries

A schematic of the experimental setup is shown in figure 3.4. The sample is fixed to a three-dimensional translation stage and lies between two poles of a water-cooled dipole electromagnet (GMW, 3480) with the sample surface being parallel to the applied magnetic field; see figure 3.4(bottom left). The electromagnet is controlled by a unipolar power supply (Ametek, XG 60-28), which is remotely controllable by a computer<sup>1</sup>. Using a Hall sensor, the actual magnetic field  $B$  within the 20 mm-wide gap has been measured for several currents. Taking a linear regression for magnetic fields  $< 600$  mT, the magnetic field

$$B(I)[\text{mT}] = 41.14 \text{ mT A}^{-1} \cdot I[\text{A}] \quad (3.6)$$

is set by applying a current  $I$  to the electromagnet. For higher magnetic fields, the mentioned relation becomes sub-linear, where the highest magnetic field is given by the maximum current of 28 A corresponding to a magnetic field of  $\approx 1$  T.

The laser system is shown in figure 3.4(top right). In this experiment the 1045 nm

---

<sup>1</sup>An additional switch has been fabricated, which is able to change the polarity at full current (max. 35 A); both remotely and locally by a mechanical switch.



laser is used as pump laser for the excitation of the sample and is indicated in a dark red color. In the very beginning the diameter of the pump laser beam is increased four times by means of a Newton telescope, which consists of two lenses with focal lengths of 200 mm and 50 mm, respectively. The same Newton telescope is used to initially increase the beam diameter of the 780 nm laser beam, which serves as probe laser. The probe laser beam is indicated in red in figure 3.4. The increase of both beam diameters is necessary to have as small laser spots as possible, when they are being focused onto the sample.

The probe beam is aligned in a confocal scheme (see figure 3.4(bottom)), whose main part is given by a non-polarizing beam splitter cube (NPBSC). Before the probe beam reaches the NPBSC, it passes an intensity attenuator and a combination of a half-wave plate and a Glan-Taylor prism in order to fix the probe beam's polarization to a vertical direction. Then, the NPBSC reflects half of the probe beam's intensity to the sample, while the other half passes the NPBSC. The reflected part of the probe beam is directed through a microscope objective (Mitutoyo, M Plan Apo NIR 20x) and, finally, focused to a spot with a radius of  $\approx 1 \mu\text{m}$  normal to the sample's surface (Voigt geometry). A half-wave plate between the NPBSC and the microscope objective is used to set the final probe polarization. The microscope objective itself has been mounted to a three-dimensional piezoelectric translation stage (Piezosystem jena, NV40 3CLE , Tritor 101

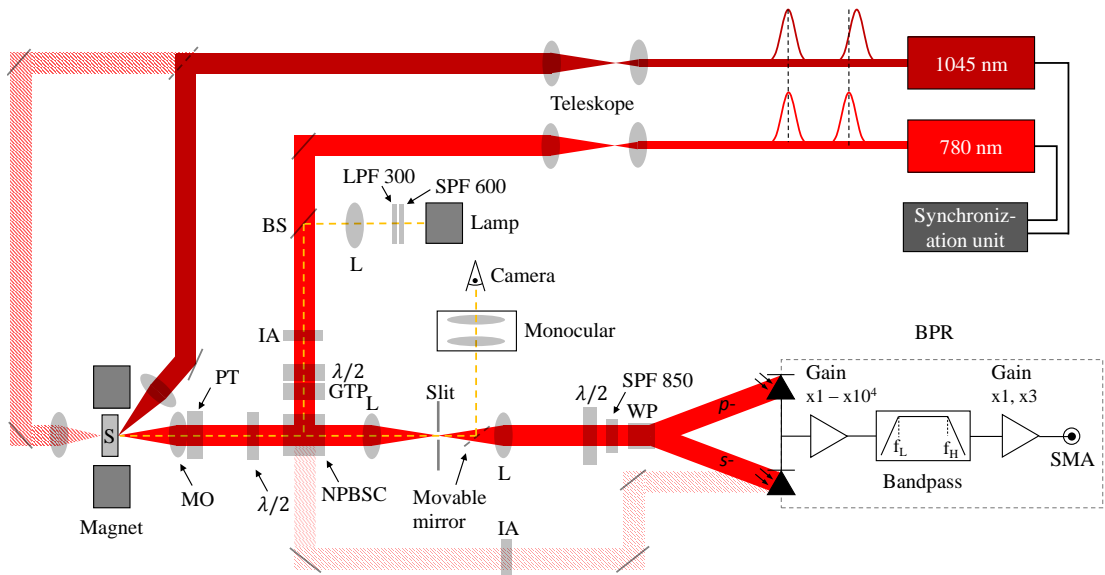


**Figure 3.4:** Schematic of the pump and probe setup: sample (S), microscope objective (MO), piezoelectric translator (PI), half-wave plate ( $\frac{\lambda}{2}$ ), nonpolarizing beam splitter cube (NPBSC), Glan-Taylor prism (GTP), lens (L), shortpass filter (SPF), longpass filter (LPF), beam splitter (BS), intensity attenuator (IA), balanced photo receiver (BPR). BPR schematic adapted from [75].

SG) in order to have a high spatial resolution of the probe beam position and a possibility to automatically scan in space. The reflected (and modulated) probe beam is collimated again by the microscope objective and (half of the intensity) is transmitted through the NPBSC to the detection part, which is mainly given by a balanced photo receiver (BPR) (Newport - Model 2107); see figure 3.4(bottom right).

The BPR consists of two silicon-based photodiodes followed by a three-stage transimpedance amplifier (current to voltage converter) [75]. In the first stage the differential signal is amplified by factors varying from 1 to  $10^4$ . The amplified signal is filtered by a band pass with a bandwidth determined by frequencies  $f_L$  and  $f_H$ . Both frequencies are adjustable from DC up to the MHz range. The last stage is given by another amplifier with amplification factors of 1 and 3.

The whole detection part is separated into two schemes: On the one hand, there is the detection of the PMOKE (see section 2.1.2) and on the other hand, there is the detection of changes in the reflection coefficient of the probe beam (see section 2.2.2). For PMOKE measurements the reflected and modulated probe beam finds its way through a half-wave plate and a Wollaston prism, where the probe beam is separated into two beams with perpendicular polarizations, but same intensities. These two beams are detected by the BPR measuring the rotation of the reflected probe pulse's polarization plane. Hence, due to the half-wave plate changes in the probe beam's polarization results in different intensities of the separated beams and, thus, a non-zero signal of the BPR. A short pass filter ( $< 850$  nm) between the half-wave plate and the Wollaston prism is used to avoid influences of the 1045 nm pump laser beam. As discussed in section 2.1.2, the mentioned technique is able to detect changes of the normal component of the dynamical magnetization ( $\delta m_z$ ).

In order to measure the change in the intensity of the reflected probe beam, no polarization optics are required in front of the BPR. In order to have a fast switch between both detection schemes, the polarization optics are not removed, but, the half-wave plate is turned in a way that behind the Wollaston prism all intensity of the probe beam is focused onto one photodiode of the BPR. The signal for the other photodiode is given by the transmitted probe beam through the NPBSC, which is indicated as a cut line in figure 3.4(bottom). The intensity of this unmodulated beam is adjusted by an intensity attenuator in order to have a perfect balance between both intensities. Hence, the differential signal for reflection measurements is given by the modulated and unmodulated probe beams' intensities.

The excitation is realized in two different schemes, which are shown in figure 3.4(left): On the one hand, there is the excitation from the frontside of the sample (solid dark

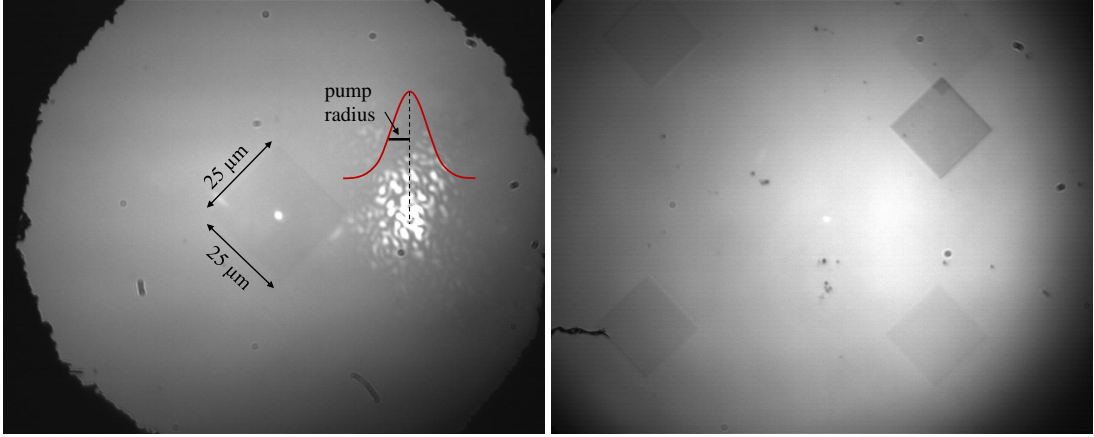


**Figure 3.5:** (left) Image of the sample’s surface containing a  $25 \times 25 \mu\text{m}^2$  big nanostructure and both focused pump and probe spots. The pump and probe spots possess radii of approximately  $5 \mu\text{m}$  and  $1 \mu\text{m}$ , respectively. For the sake of clarity, the pump beam is moved away from the probe beam. The scattered shape of the pump spot is due to its angle of incidence. In this case no direct light, but only scattered light reaches the detection beam line. (right) Image of several nanostructures with different depth. The depth can be roughly estimated by the contrast, where a relatively dark appearance relates to a deep structure. The small black dots indicate dust or defects in the surface of the sample.

red line), where both pump and probe beams find their incidence onto the same side of the sample. While the probe beam has normal incidence onto the sample, the pump pulse has an angle of incidence of  $45^\circ$  and is focused to a spot radius (half width half maximum) of  $\approx 5 \mu\text{m}$  via a lens with focal length of  $50 \text{ mm}$ . Figure 3.5(left) shows an image of the sample containing a nanostructure and the small probe spot in the center of the image and the large pump spot, which is shifted to the right side next to the probe spot. On the other hand, there is the excitation from the backside meaning that the pump pulse has normal incidence onto the opposite side as the probe pulse (cut dark red line in figure 3.4). In this case, the pump pulse is focused to a spot radius of roughly  $5 \mu\text{m}$  via a lens with focal length of  $40 \text{ mm}$ . The actual pump radii for both excitation geometries are evaluated in section A.1.

For visualization of the sample surface, a visualization scheme has been realized, which is shown in the center of figure 3.4. The corresponding beam line is indicated as a cut yellow line. The basic visualization scheme consists of a gooseneck lamp and a monocular (Edmund Optics, 0.75x to 3x with 20x eyepiece), which is connected to a webcam (Thorlabs, DCC1545M). The cold white light of the lamp passes two filters (long pass filter at  $600 \text{ nm}$  and short pass filter at  $1500 \text{ nm}$ ) in order to cut anti-reflected components of the NPBSC. By using a beam splitter the light of the lamp is introduced into the probe beam line. In order to use the confocal scheme as a microscope a movable mirror has to be introduced into the detection beam line. The lens in front of the slit

is used to convert the (reflected) image of the sample into an image on the webcam. In this case, both the lens and the monocular find their focal points in the same spot, which is given by the slit.

Two exemplary images for the frontside excitation geometry are shown in figure 3.5. The well focused spot of the probe beam lies in the center of both images in figure 3.5. The bright and scattered big spot of the pump beam is shifted away from the probe spot. The gray square in the center indicates a  $25 \times 25 \mu\text{m}^2$  big nanograting. Figure 3.5(right) shows an image with several nanostructures, where the magnification of the monocular has been decreased accordingly. After an alignment of all important parts, the movable mirror is removed and the detection is open again for reflection and PMOKE measurements.

For all experiments in this work, the first stage amplification of the BPR varies between  $10^2$  and  $10^4$ . The bandwidth is set to  $f_L = 100 \text{ Hz}$  and  $f_H = 10 \text{ MHz}$  throughout the whole experiment in order to avoid low-frequency contributions to the output signal. It has been checked that the measured signals given by the modulated probe beams are not effected by the used bandwidth<sup>2</sup>. The amplification of the stage-three amplifier is always set to 1. The approximate output voltage [75]

$$V_{\text{out}} = (P_{\text{pr}}^+ - P_{\text{pr}}^-) \cdot R_{\text{BPR}} \cdot G_{\text{BPR}} \quad (3.7)$$

is determined by the input optical powers  $P_{\text{pr}}^\pm$  in Watts on the right and left photodiodes, respectively.  $R_{\text{BPR}}$  denotes the photodetector's response factor in V/mW and  $G_{\text{BPR}}$  the amplifier's gain. The response factor for the 780 nm probe beam is approximately 0.33 V/mW [75]. The differential saturation power  $\Delta P_{\text{pr}} = P_{\text{pr}}^+ - P_{\text{pr}}^-$  for the lowest gain setting is 20 mW. Equation 3.7 is used to calculate the relative amplitude of a measured signal,  $\frac{\Delta P_{\text{pr}}}{P_{\text{pr}}^r}$ , which is given by the differential power  $\Delta P_{\text{pr}}$  and the power of the reflected probe beam  $P_{\text{pr}}^r$ . The performance of the BPR's bandwidth for a (maximal used) gain of  $1 \cdot 10^4$  is approximately 250 kHz (in lab time) [75]. The corresponding bandwidth performance in real time is  $10^5 \cdot 250 \text{ kHz} = 250 \text{ GHz}$ , which yields a real time resolution of  $\frac{1}{250 \text{ GHz}} \approx 4 \text{ ps}$ . Other used gains of  $10^2$  and  $10^3$  correspond to real time resolutions of  $\frac{1}{10^5 \cdot 8 \text{ MHz}} \approx 0.1 \text{ ps}$  and  $\frac{1}{10^5 \cdot 700 \text{ kHz}} \approx 1.4 \text{ ps}$ , respectively.

The accumulation of the data provided by the BPR (via SMA connector) is realized by an oscilloscope (Tektronix, DPO 5104), which is connected to a computer via USB. The trigger signal is provided by the synchronization unit of the ASOPS system. The horizontal time scale of the oscilloscope is set to 100  $\mu\text{s}$  per div, which gives a total (lab)

---

<sup>2</sup>Expected transient modulations of the probe beam are in the order of 10 GHz (real time). In this case corresponding frequencies in the lab time are  $\frac{10 \text{ GHz}}{10^5} = 100 \text{ kHz}$ , where  $10^5$  is the scaling factor in equation 3.5. Therefore, the transient signals are not affected by the used bandwidth of the BPR.

time window of  $10 \cdot 100 \mu\text{s} = 1 \text{ ms}$ . By considering the difference between lab and real time, the lab time window of 1 ms corresponds to a real time window of  $\frac{1 \text{ ms}}{10^5} = 10 \text{ ns}$ . The maximum real time window is given by the repetition rate of the laser, i.e. 12.5 ns. The vertical scale of the oscilloscope lies in the range of 2 to 20 mV, which depends on the signal to noise ratio for a single (non-accumulated) signal. The bandwidth and sample rate are set to 1 GHz and  $20 \frac{\text{MS}}{\text{s}}$ , respectively. The recording length is  $2 \cdot 10^4$  samples, which results in a real time resolution of 0.5 ps. The termination is  $50 \Omega$ . The horizontal delay mode is enabled so that the measured signal can be shifted horizontally in time in order to have a reasonable position of the signal's starting point. A typical measurement takes approximately one to five minutes depending on the intended signal to noise ratio. The final data accumulation and analysis is performed on the computer using MATLAB<sup>®</sup> (see section A.2).

### 3.3 Preliminary Work

#### 3.3.1 Sample Characterization

For all preliminary measurements a sample consisting of a 105 nm Galfenol ( $\text{Fe}_{0.81}\text{Ga}_{0.19}$ ) layer grown by magnetron sputtering on a (001) semi-insulating GaAs substrate is used and schematically shown in figure 3.6. In order to avoid oxidation of the Iron-based alloy, a 3 nm-thin Chromium (Cr) cap is evaporated onto the Galfenol layer.

#### 3.3.2 Optical Absorption Depth in Galfenol

In general, the optical absorption depth  $\zeta$  for light with wavelength  $\lambda$  in a certain material with extinction coefficient  $\kappa$  can be calculated by [60] (see section 2.2.2 for further information)

$$\zeta = \frac{\lambda}{4\pi\kappa}. \quad (3.8)$$

For pure Iron the extinction coefficients for the (1045 nm) pump and (780 nm) probe light are  $\kappa_{\text{Fe}} = 3.95$  and 3.32, respectively [76]. According to equation 3.8 corresponding optical absorption depth are 19 nm and 21 nm, respectively.

The experimental value for the optical absorption depth in Galfenol is obtained by measuring the transmission of a normal-incident pump beam through a 105 nm-thick Galfenol layer. The experiment and all necessary refractive indices for the 1045 nm pump beam are shown in figure 3.6<sup>3</sup>. Due to the vanishing extinction coefficient for the 1045 nm pump light in GaAs [77], there is no absorption inside the GaAs substrate. As-

<sup>3</sup>It is assumed that Galfenol and Iron have similar (complex) refractive indices.

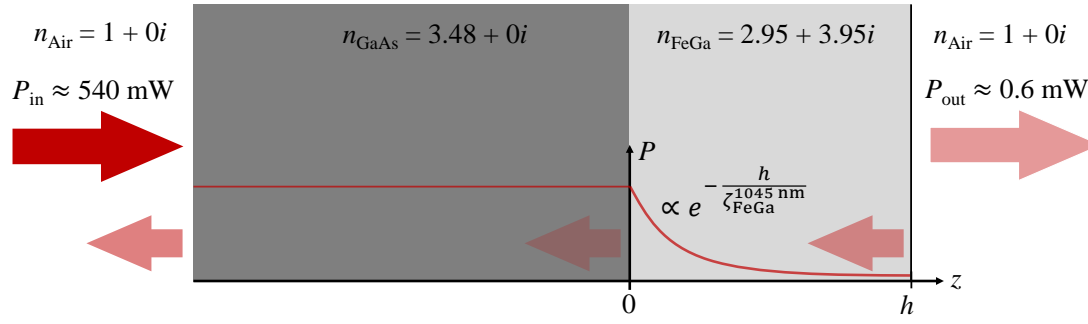


**Figure 3.6:** Schematic of the performed experiment to estimate the optical absorption depth for the 1045 nm pump light in Galfenol. The references of the presented complex refractive indices can be found in the text. The influence given by the 3 nm Cr cover is ignored. The slightly transparent arrows pointing to the left indicate occurring reflections of the incident beam at respective interfaces.

suming an exponential absorption behaviour in the Galfenol layer, the relation between the laser power before the sample,  $P_{\text{in}}$ , and after,  $P_{\text{out}}$ , reads

$$\frac{P_{\text{out}}}{P_{\text{in}}} = \left(1 - \left|\frac{n_{\text{Air}} - n_{\text{GaAs}}}{n_{\text{Air}} + n_{\text{GaAs}}}\right|^2\right) \left(1 - \left|\frac{n_{\text{GaAs}} - n_{\text{FeGa}}}{n_{\text{GaAs}} + n_{\text{FeGa}}}\right|^2\right) \left(1 - \left|\frac{n_{\text{FeGa}} - n_{\text{Air}}}{n_{\text{FeGa}} + n_{\text{Air}}}\right|^2\right) e^{-\frac{h}{\zeta_{\text{FeGa}}^{1045 \text{ nm}}}}, \quad (3.9)$$

where  $n_i$  are respective (real) refractive indices and  $h$  is the layer thickness. Hence, the optical absorption depth for the 1045 nm pump light in a 105 nm Galfenol layer can be evaluated to

$$\zeta_{\text{FeGa}}^{1045 \text{ nm}} \approx (20.7 \pm 0.4) \text{ nm} \quad (3.10)$$

and is in good accordance with the calculated values for pure Iron. Therefore, both pump and probe pulses possess an optical absorption depth of roughly 20 nm. The uncertainty in equation 3.10 was calculated using the (Gaussian) propagation of uncertainty.

### 3.3.3 Comparison of Transient Reflection Measurements for Two Different Excitation Geometries

As mentioned in section 3.2 and illustrated in figure 3.4 on page 37, the experimental setup provides two different excitation geometries: (1) The pump and probe pulses are focused onto the same side of the Galfenol layer (frontside excitation) or (2) the pump pulse is focused onto the other side of the sample as the probe pulse (backside excitation). The main difference between these two excitation geometries is in the thermal background of the transient reflection measurements, where exemplary measurements

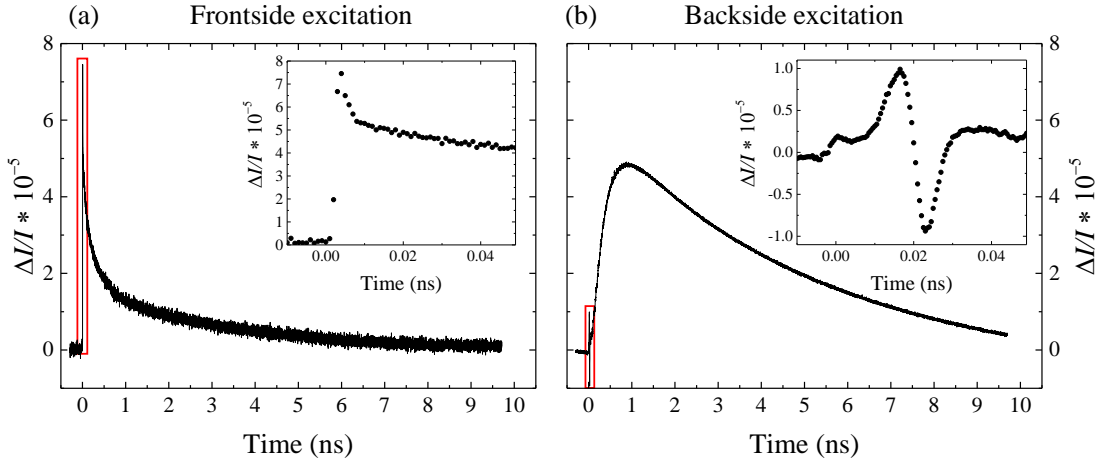


**Figure 3.7:** (a) Transient reflection signal for the case of an excitation from the frontside of the sample, where the pump pulse has an angle of incidence of  $45^\circ$ . A sharp increase is followed by an exponential decay of the reflection signal, which indicates the heat diffusion away from the probe spot. The inset shows a zoom of the sharp increase around  $t = 0$ , which corresponds to the temporal overlap of the pump and probe pulses. (b) This plot shows a transient reflection signal for an excitation from the backside of the Gallenol layer. After the excitation by the pump pulse ( $t = 0$ ) a longitudinal strain pulse is introduced and detected (inset). Afterwards, both an increase and decrease are observed, which indicate the heat transport to and away from the probe spot.

performed on the 105 nm-thick Gallenol layer are shown in figure 3.7.

In figure 3.7(a), a transient reflection signal corresponding to an excitation from the frontside is shown. The pump and probe powers in front of the sample are 300 mW and 5 mW, respectively. According to equation A.3 the corresponding energy densities per pulse are  $3.3 \text{ mJ/cm}^2$  and  $1.4 \text{ mJ/cm}^2$ , respectively<sup>4</sup>. The BPR amplifier is set to  $10^2$ . The reflected probe power  $P_{\text{pr}}^r \approx 0.8 \text{ mW}$ . In this measurement only one photo diode of the BPR is used instead of the differential scheme. As it is shown in equation 2.34, the change in the reflected intensity  $\frac{\Delta I}{I} = \frac{\Delta P_{\text{pr}}}{P_{\text{pr}}}$  is proportional to the change in reflection  $\frac{\Delta R}{R}$  and, therefore, to the strain in the sample. As seen in figure 3.7 and according to equation 3.7 the relative strain amplitude lies in the range of  $10^{-5}$ . The main characteristic feature in figure 3.7(a) is given by a sharp increase corresponding to the transient overlap of the pump and probe pulses. As theoretically discussed within the two-temperature model in section 2.2.1, the very first sharp in- and decrease of the transient signal corresponds to the excited electron system (see inset). After several ps the electron system has transferred the energy to the lattice, so that the main contribution to the signal is given by lattice temperature induced changes, where the exponential decay indicates thermal diffusion away from the probe spot.

<sup>4</sup>The pump spot radius is  $5 \mu\text{m}$  (section A.1) and the probe spot radius is approx.  $1 \mu\text{m}$ .

The reflection signal in figure 3.7(b) corresponds to the geometry of backside excitation. The pump power in front of the sample is 500 mW, while the probe power remains the same. According to equation A.3 the corresponding energy densities per pulse are 5.5 mJ/cm<sup>2</sup> and 1.4 mJ/cm<sup>2</sup>, respectively. In contrast to the previous measurement, this measurement utilizes the differential scheme for detection. Hence, the BPR gain is increased to 10<sup>3</sup> and the reflected probe power is now given by 2 · 0.8 mW, because both photodiodes are illuminated. As expected, the evaluated relative reflected intensity  $\frac{\Delta I}{I}$  lies in the same range as for frontside excitation, but with a better signal to noise ratio compared to the usage of a single photodiode.

The transient signal for backside excitation (figure 3.7(b)) starts with a longitudinal bipolar strain pulse, which is introduced by the absorbed fs pump pulse accordingly to the discussion in section 2.2.2. The strain pulse is marked by a red square in the main signal and more precisely shown in the inset using black dots. The ideal shape of the introduced strain pulse in equation 2.36 is rounded due to electron and thermal diffusion and the finite optical absorption depth of the probe pulse [60].

The strain pulse is followed by a slow increase of the reflection signal up to 1 ns and, then, a slow decrease back to zero. This curve indicates the thermal diffusion from the heated backside to the probed frontside of the 105 nm-thick Galfenol layer. A rough estimation of the characteristic heat diffusion time is given by the one dimensional heat equation [78] and can be written as

$$\tau_{\text{HD}} \approx \frac{h^2}{D}, \quad (3.11)$$

where  $h$  is the layer thickness,  $D = \frac{k_1}{C_1}$  is the thermal diffusivity,  $k_1$  is the thermal conductivity and  $C_1$  is the heat capacity [79]. Without considering any influences given by the pump and probe pulses, at room temperature  $C_1^{\text{Fe}} \approx 3.6 \times 10^6 \text{ J/m}^3/\text{K}$  [80] and  $k_1^{\text{Fe}} = 79.5 \text{ W m}^{-1} \text{ K}^{-1}$  [81], which yield a characteristic diffusion time of 0.5 ns. Thus, the expected heat diffusion time for a 105 nm Iron nanolayer is in the order of ns. Therefore, the observed shape indicates the heat diffusion from the backside to the frontside of the sample. The discrepancy between the observed and calculated diffusion time lies mainly in the simplified model used in equation 3.11. However, a different layer thickness or thermal diffusivity for Galfenol may also contribute to the discrepancy.

Figure 3.8(a) presents the pump power dependence of transient reflection signals for the case of backside excitation. The corresponding inset shows a zoomed fragment focusing on the detected longitudinal strain pulse. In the transient signals a clear increase of the amplitude is observed for increasing pump powers. Figure 3.8(b) presents the power



dependence of evaluated reflection amplitudes. On the one hand, the maximum of the whole reflection signal is taken and on the other hand, the positive amplitude of the strain pulse is used to estimate their power dependence. As expected a linear increase of the thermally induced strain is observed for large excitation densities. Thus, all experiments are performed in the linear regime of optically induced strain.

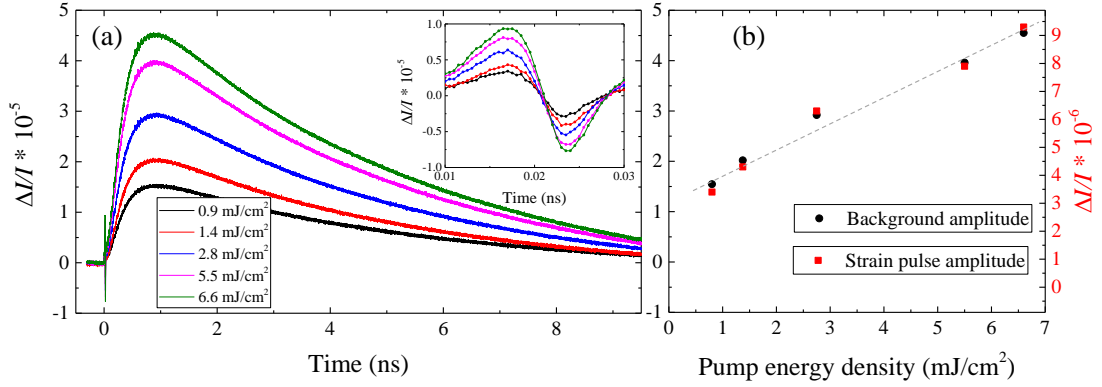


**Figure 3.8:** (a) Pump power dependence of transient reflection signals. (b) Pump power dependence of evaluated reflection amplitudes: The maximum of the whole reflection signal is indicated as black dots, while the positive amplitude of the strain pulse is indicated as red squares. The cut line is to guide the eye.



## Chapter 4

# Optical Excitation of Multi- and Singlemode Magnetization Precession in Galfenol Nanolayers

An active field in magnonics is the generation of coherent high-frequency and high-amplitude microwave signals at the nanoscale<sup>1</sup>. A promising solution is given by the magnetization precession of ferromagnetic nanolayers. In this case, the magnetization precession is used as a source for the generation of an oscillating magnetic field. A broadband excitation of the magnetization precession can be realized by means of picosecond magnetic field pulses [10], ultrashort laser pulses [12] and strain pulses [13]. The resulting response of the magnetization precession usually possesses a small amplitude and a broad spectrum with a corresponding small lifetime [38],[21]. Therefore, there is a great interest in the development of coherent high-frequency magnetic responses with long lifetimes in ferromagnetic materials.

This chapter demonstrates a variety of optically excited precessional responses in Galfenol nanolayers and the possibility of isolating a single precession mode using ultrathin nanolayers. The nanolayers with varying layer thicknesses are characterized in section 4.1. The following section 4.2 introduces the basic concept of localized magnon modes in ferromagnetic nanolayers using the free energy density (FED) approach. The main experimental interest is in the dependence of magnetic responses on an in-plane applied magnetic field, which are discussed and modelled within the FED approach (sections 4.3 to 4.5).

---

<sup>1</sup>An exemplary implementation can be found in the magnetic storage technology, especially in microwave-assisted magnetic recording (MAMR) [2].

## 4.1 Sample Characterization

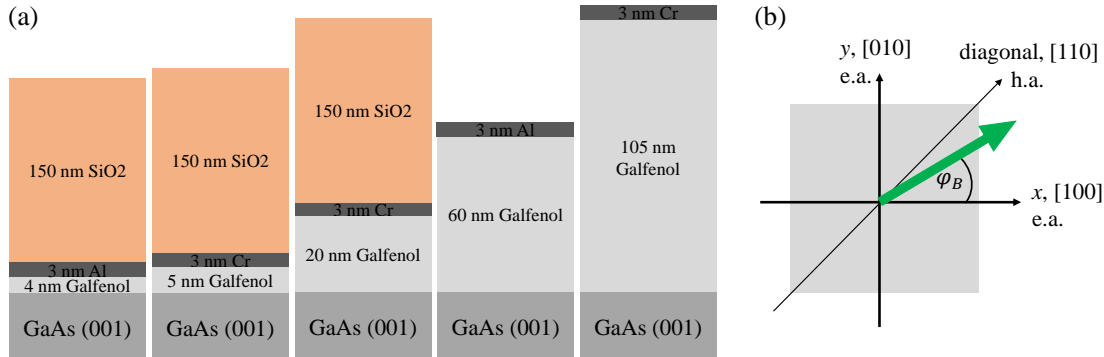


**Figure 4.1:** (a) Investigated Galfenol nanolayers with thicknesses of 4, 5, 20, 60 and 105 nm on semi-insulating GaAs substrates. For layer thicknesses  $\leq 20$  nm an additional 150 nm SiO<sub>2</sub> layer is used to increase the PMOKE. Different cap layers made of Al and Cr are used to avoid any oxidation of the underlying Galfenol layers. (b) In-plane crystallographic directions of the studied nanolayers, where respective easy and hard magnetization axes are indicated, as well. The magnetic field orientation is denoted by an angle  $\varphi_B$ .

The samples studied in this work are five Galfenol (Fe<sub>0.81</sub>Ga<sub>0.19</sub>) nanolayers with thicknesses  $h = 4, 5, 20, 60$  and 105 nm; see figure 4.1(a). The nanolayers have been grown by magnetron sputtering on (001) semi-insulating GaAs substrates and, hence, the Galfenol nanolayers are characterized by a growth axis along the [001]-crystallographic direction. All layers are covered by either a 3 nm-cap layer of Al (4 and 60 nm Galfenol layer) or Cr (other nanolayers) to prevent oxidation. A 150 nm SiO<sub>2</sub> cap is deposited on the Galfenol layers with thicknesses  $\leq 20$  nm for an amplification of the magneto-optical Kerr effect [82]. It has been checked experimentally that the SiO<sub>2</sub> cap does not affect the anisotropy parameters of the layers.

In the case of Galfenol nanolayers and in-plane applied magnetic fields, it is sufficient to consider only the plane perpendicular to the growth axis, i.e.  $xy$ -plane. Figure 4.1(b) illustrates the plane of interest with corresponding crystallographic directions indicated as easy (e.a.) and hard magnetization axes (h.a.), respectively; however, the shown symmetry of the cubic anisotropy is slightly altered by the contribution of the uniaxial anisotropy along the [110]-crystallographic direction (see equation 2.10). The uniaxial anisotropy is typical of thin Galfenol layers [37]. The relation between the crystallographic directions and the in-plane applied magnetic field is denoted by an angle  $\varphi_B$ . A magnetic field orientation along the [100]-crystallographic direction corresponds to  $\varphi_B = 0$ . Positive angles indicate a counter-clockwise rotation of the applied magnetic field.

## 4.2 Formation of Magnon Modes in Galfenol Nanolayers

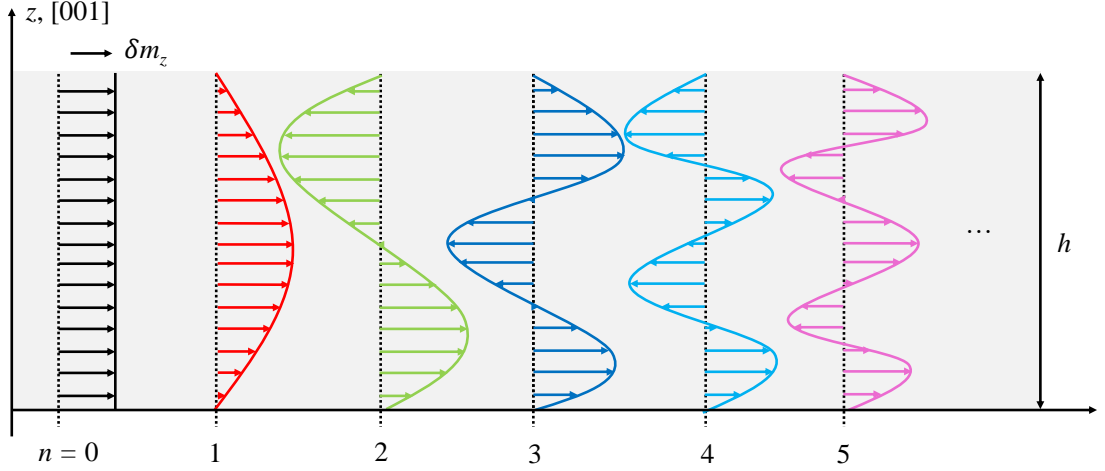


**Figure 4.2:** Formation of localized magnon modes due to spatial confinement in a ferromagnetic nanolayer for fixed boundary conditions. The lowest mode indicated by  $n = 0$  possesses a quasi uniform spatial distribution of the magnetization precession, but is slightly disturbed at the interfaces due to fixed boundary conditions.

Since, the theoretical work done by Kittel in 1958, it is known that the spatial confinement of ferromagnetic layers results in the formation of discrete magnon modes [8]. The formation of the magnon modes is determined by the boundary conditions at the layer surfaces and, especially, the layer thickness. For the studied Galfenol nanolayers of 5, 20 and 105 nm thickness, fixed boundary conditions are assumed, because the nanolayers are sandwiched between an antiferromagnetic Cr layer [83] and a GaAs substrate [84] (section 4.1). In addition, in this thesis also fixed magnetic boundary conditions are assumed for the other nanolayers with an Al cap. According to Kittel, for an intermediate layer thickness  $h$  with fixed boundary conditions, the allowed wave vectors are given by  $\cos(k_n h) = \pm 1$ , where  $n = 1, 2, \dots$  are magnon mode numbers. The corresponding wave vectors can be explicitly written as

$$k_n = \frac{\pi n}{h}. \quad (4.1)$$

An illustration of several modes is presented in figure 4.2. Figure 4.2 indicates that the spatial profiles of localized magnon modes are mainly determined by the spatial dimensions of the nanolayers. The lowest mode ( $n = 0$ ) is characterized by a quasi uniform distribution, which may be disturbed close to the surface<sup>2</sup> [85]. The arising high-order

<sup>2</sup>The disturbance of the magnetization is described by a so-called surface anisotropy  $F_{\text{surf}}$  [8]. Fixed and free boundary conditions are described by the relation between the exchange energy and the surface energy, i.e.  $F_{\text{exchange}} \ll F_{\text{surf}}$  (fixed) and  $F_{\text{exchange}} \gg F_{\text{surf}}$  (free), respectively [85]. If the exchange

magnon modes can be considered as standing spin waves, which are localized along the  $z$ -direction of the nanolayer.

Besides the wave vector, a spin wave is characterized by a corresponding precession frequency. The precession frequencies  $f_n$  of the localized modes are defined by the free energy density of the Galfenol nanolayers  $F^{\text{layer}}$  containing certain anisotropy contributions, such as the magneto-crystalline anisotropy (MCA). By considering the exchange interaction with spin stiffness constant  $D$ , an approximation for the precession frequencies is given by [86]

$$f_n = \gamma_e \sqrt{F_{\varphi\varphi}^{\text{layer}} \cdot F_{\theta\theta}^{\text{layer}} + (F_{\varphi\varphi}^{\text{layer}} + F_{\theta\theta}^{\text{layer}}) \cdot Dk_n^2}, \quad (4.2)$$

where  $F_{\varphi\varphi}^{\text{layer}} = \frac{\partial^2 F^{\text{layer}}}{\partial \varphi^2}$  and  $F_{\theta\theta}^{\text{layer}} = \frac{\partial^2 F^{\text{layer}}}{\partial \theta^2}$  describe second-order derivatives of the free energy density at the equilibrium orientation of the magnetization.  $\gamma_e = \frac{\gamma'_e}{2\pi} \approx 28 \text{ GHz T}^{-1}$  is the gyromagnetic ratio of a free electron [39]. In case of a strong external magnetic field, equation 4.2 can be written as

$$f_n = \gamma_e \sqrt{F_{\varphi\varphi}^{\text{layer}} F_{\theta\theta}^{\text{layer}}} \sqrt{1 + \frac{F_{\varphi\varphi}^{\text{layer}} + F_{\theta\theta}^{\text{layer}}}{\sqrt{F_{\varphi\varphi}^{\text{layer}} F_{\theta\theta}^{\text{layer}}}} Dk_n^2} \quad (4.3)$$

$$\approx f_0 + \gamma_e \beta D k_n^2. \quad (4.4)$$

Hence, the initial equation 4.2 can be separated into two parts: A part which is independent of the wave vector and a part which depends on the wave vector  $k_n$ . The wave vector-independent part describes the precession frequency of the uniform mode and reads

$$f_0 = \gamma_e \sqrt{F_{\varphi\varphi}^{\text{layer}} \cdot F_{\theta\theta}^{\text{layer}}}. \quad (4.5)$$

This mode is always present for any layer thickness and is also known as Kittel mode. The second part of equation 4.4 denotes the contribution given by the spatial confinement. By considering the allowed wave vectors (see equation 4.1), the frequency splitting between a certain magnon mode with the uniform mode reads

$$f_n - f_0 \approx \gamma_e \beta D \left( \frac{\pi n}{h} \right)^2. \quad (4.6)$$

Hence, for large layer thicknesses  $h$  the frequency splitting becomes very small. If the frequency splitting becomes smaller than the linewidths of the considered modes, the magnon modes can be considered as degenerated; as it is expected for the non-

---

energy is larger than the surface energy, previously fixed boundary conditions can be altered to free boundary conditions [85].

confined case.  $\beta = \frac{F_{\varphi\varphi}^{\text{layer}} + F_{\theta\theta}^{\text{layer}}}{2\sqrt{F_{\varphi\varphi}^{\text{layer}} F_{\theta\theta}^{\text{layer}}}}$  is a field-dependent coefficient and approaches unity for large magnetic fields.

Besides the influence of the magneto-crystalline anisotropy on the precession frequency, the Gilbert damping parameter  $\alpha$  in the LLG equation in 2.14 is also affected by the magneto-crystalline anisotropy. This leads to an experimentally observed effective Gilbert damping parameter [87]

$$\alpha_{\text{eff}} = \frac{1}{2\pi f \tau_{\text{eff}}} = \frac{\alpha \gamma_e}{2f} \left( F_{\theta\theta}^{\text{layer}} + F_{\varphi\varphi}^{\text{layer}} \right), \quad (4.7)$$

where  $\tau_{\text{eff}}$  is the effective lifetime of the magnetization precession. The expression in equation 4.7 is important to compensate the experimentally observed values for the influence by the MCA.

To conclude, ferromagnetic nanolayers are characterized by quantized spin waves, i.e. magnons. For ultrathin layers the degeneracy of the precession frequencies is lifted and discrete magnon modes appear (figure 4.2). The resulting precession frequencies  $f_n$  are determined by equation 4.2 and respective wave vectors  $k_n$ . The wave vectors in the studied Galfenol nanolayers are determined by fixed boundary conditions and the layer thickness  $h$ .

### 4.3 Observation of Multi-Mode Magnetization Precession in an Intermediate Galfenol Nanolayer

The main sample in this section is given by an 105 nm Galfenol layer sandwiched between a Cr layer and a GaAs substrate. The optical excitation is realized from the frontside of the sample, where the energy density of the fs pump pulse is 0.3 mJ/cm<sup>2</sup> so that no demagnetization occurs [88](SupplementalMaterial). The detection scheme is given by a balanced photo receiver, which is used to trace the polar optical Kerr effect (PMOKE). The energy density of the fs probe pulse is 0.5 mJ/cm<sup>2</sup> and the probe pulse's linear polarization is vertical (parallel to [010]-crystallographic direction)<sup>3</sup>.

Figure 4.3(a) demonstrates a characteristic transient PMOKE signal of the 105 nm Galfenol nanolayer at  $B = 200$  mT and  $\varphi_B = -22^\circ$ . While the PMOKE signal is measured within a time window of 10 ns, the figure only shows a fraction of roughly 2.5 ns. The presented signal is characterized by an immediate response to the ultra-fast excitation and an expected damped oscillating behaviour; which is related to the

---

<sup>3</sup>It was checked for smaller probe energy densities that the utilized large energy density does not affect the overall results.

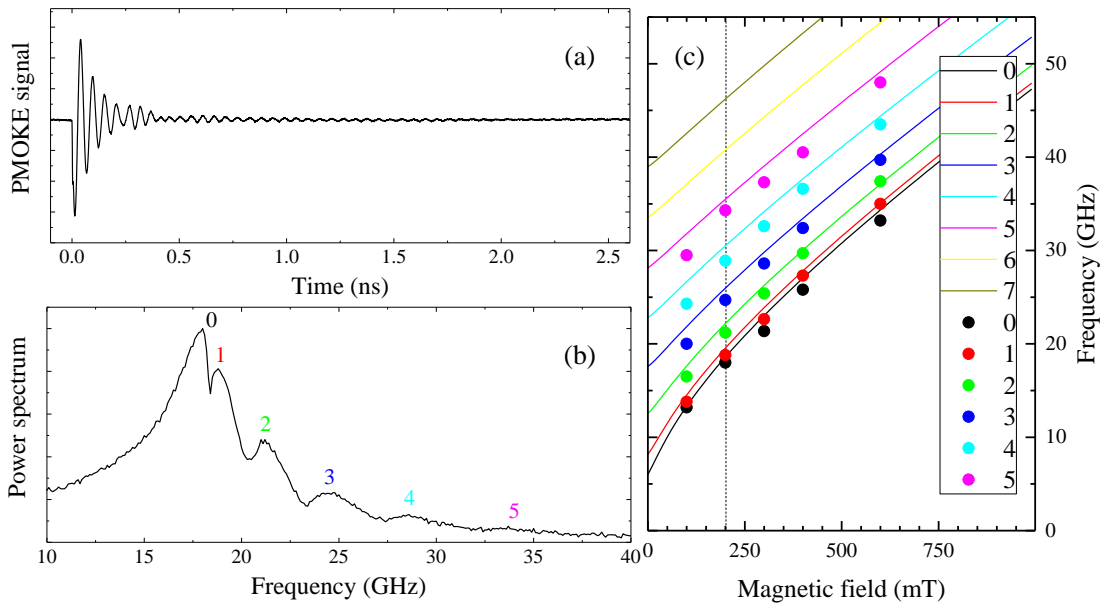


**Figure 4.3:** (a) Transient PMOKE signal at  $B = 200$  mT and  $\varphi_B = -22^\circ$ . (b) Power spectrum of the signal in (a), where the full time window of 10 ns is taken. (c) Magnetic field dependence of the observed magnon mode frequencies (coloured dots) and calculated precession frequencies using equation 4.2 and the free energy density in equation 4.8.

magnetization precession. The immediate response itself is induced by a modification of the magneto-crystalline anisotropy (MCA) [38]. The rapid decay of the initial amplitude of roughly 0.5 ns gives hint at a broad magnon spectrum and is consistent with previously reported results for Galfenol nanolayers [38],[21]. However, a closer look at the signal's amplitude shows beating, which indicates the presence of more than one frequency. A corresponding power spectrum (Fast Fourier transform)<sup>4</sup> of the full 10 ns time range is shown in figure 4.3(b). The power spectrum of the transient PMOKE signal indicates the presence of several overlapping modes, which can be identified as localized (high-order) magnon modes (see coloured numbers). The identification is done via the FED approach and is carefully discussed in the next paragraph. The power spectrum in figure 4.3(b) is characterized by at least six magnon modes, where for high precession frequencies the spectral amplitudes become smaller and the spectral lines become broader. Smaller spectral amplitudes for higher modes indicate a decrease in the respective excitation efficiency. A corresponding broadening of the spectral lines indicates smaller lifetimes. The behaviour of different lifetimes is related to magnon decay mechanisms, which are discussed in section 2.1.2. Possible damping mechanisms for a broadening for higher precession frequencies are the spin-orbit coupling or the two-magnon scattering [44], [89]. The two-magnon scattering as possible damping

<sup>4</sup>The relation between the transient signal and its power spectrum is discussed in detail in the appendix in section A.3.



mechanism is further investigated for an ultrathin nanolayer later in section 4.5.

The identification of the observed magnon modes is realized using the free energy density approach, especially equation 4.2. Figure 4.3(c) presents the magnetic field dependence of the evaluated magnon frequencies as coloured dots. Every colour indicates a certain mode inside the magnon spectrum; see figure 4.3(b). All modes possess a similar magnetic field dependence with a frequency offset, which is given by the frequency splitting due to the spatial confinement (see equation 4.6). The shown coloured lines are calculated precession frequencies using the free energy density approach, especially equation 4.2. The corresponding free energy density reads [38]

$$\begin{aligned}
 F^{\text{layer}} = & -\mathbf{m}\mathbf{B} \\
 & + K_1(m_x^2m_y^2 + m_x^2m_z^2 + m_y^2m_z^2) \\
 & - K_u(m_x + m_y)^2 \\
 & + B_d m_z^2.
 \end{aligned} \tag{4.8}$$

The used parameters are  $h = 105$  nm,  $K_1 = 18$  mT,  $K_u = 1.8$  mT,  $D = 23$  mT/nm<sup>2</sup>, which are in good accordance with previously reported values [38],[67]. The non-zero  $K_1$  and  $K_u$  indicate an influence by both the cubic and uniaxial anisotropy, respectively. In order to determine the anisotropy parameters  $K_i$ , the angular dependence of the quasi uniform mode's frequency is being investigated. Figure 4.4(a) shows an experimentally obtained angular dependence at  $B = 200$  mT (black dots). A quantitative analysis is presented by the calculated black line using equation 4.2 with the same parameters as for the previous analyses, i.e.  $K_1 = 18$  mT and  $K_u = 1.8$  mT. The butterfly-like

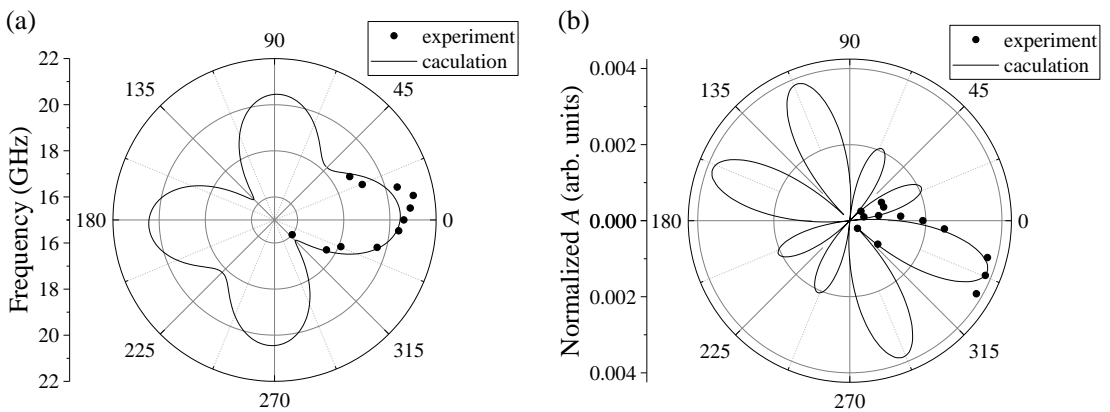


**Figure 4.4:** Angular dependencies of the precession (a) frequency and (b) amplitude of the lowest mode of a 105 nm-thick Galfenol layer at a magnetic field strength of 200 mT. The theoretical curves (black lines) are calculated using the free energy density approach.

shape of the calculated curve nicely indicates the disturbed fourfold symmetry of the cubic anisotropy by the uniaxial anisotropy along the [110]-crystallographic direction. The influence of the uniaxial anisotropy is also seen in the precession amplitude of the quasi uniform mode. A corresponding angular dependence is presented in figure 4.4(b). Due to the uniaxial anisotropy, different experimentally obtained amplitudes for  $\varphi_B = -22^\circ$  and  $+22^\circ$  are observed. The amplitude of the magnetization precession can be phenomenologically estimated to<sup>5</sup>

$$A(\varphi_B, B) \approx \frac{\frac{\Delta K_1}{2} \sin 4\varphi_B - \Delta K_u \cos 2\varphi_B}{\sqrt{B(B + \mu_0 M_s)}}, \quad (4.9)$$

where  $\Delta K_1 = \frac{\partial K_1}{\partial T}$  and  $\Delta K_u = \frac{\partial K_u}{\partial T}$  are temperature induced changes of respective anisotropy coefficients  $K_1$  and  $K_u$ . The black line in figure 4.4(a) presents the absolute value of equation 4.9. The maximum experimentally obtained amplitude of the PMOKE signal is being observed for  $\varphi_B = -22^\circ$ , which indicates a larger temperature induced change of  $K_1$  than  $K_u$ . Therefore, we estimate the anisotropy changes to  $\Delta K_1 = -3.7$  mT and  $\Delta K_u = -1.2$  mT (in comparison to the estimations in [38]). The measured PMOKE amplitudes are being normalized to the calculated curve in order to show the qualitative accordance of the angular anisotropy; especially the influence by the uniaxial anisotropy.

Another important characteristic of transient PMOKE signals in the 105 nm Gallenol layer is presented in figure 4.5(a). The presented PMOKE signal is similar to the already discussed one in figure 4.3(a), whereas the focus lies on the long living tail, which is marked by red lines in figure 4.5(a). The inset shows the tail of the signal starting from 0.75 ns, where the contributions by the other modes have been clearly vanished. The corresponding power spectrum is given in figure 4.5(b). While the whole PMOKE signal contains several magnon modes, the spectrum of the tail only possesses one narrow line with a single frequency. In order to quantify the lifetime of the tail, a regression using a damped sine function can be used:

$$\Delta m_z(t) = A e^{-\gamma_{\text{eff}} t} \sin(2\pi f t + \Psi), \quad (4.10)$$

where  $A$  is the maximum Kerr rotation amplitude,  $\gamma_{\text{eff}}$  is the effective damping parameter,  $f$  is the frequency and  $\Psi$  a phase. The effective parameters arise due to the influence given by the MCA (see equation 4.7). The effective damping parameter  $\gamma_{\text{eff}} = \frac{1}{\tau_{\text{eff}}} = \pi \Delta f_{\text{eff}}$  defines the effective signal's lifetime  $\tau_{\text{eff}}$  and the effective full width at half maximum (FWHM) of the spectral line in the power spectrum,  $\Delta f_{\text{eff}}$ <sup>6</sup>. The ef-

<sup>5</sup>Equation 4.9 is an estimation for small  $\Delta K_i$  and no demagnetization. Both requirements are satisfied for the used pump energy density [88](SupplementalMaterial).

<sup>6</sup>A detailed derivation is given in the appendix in section A.3.

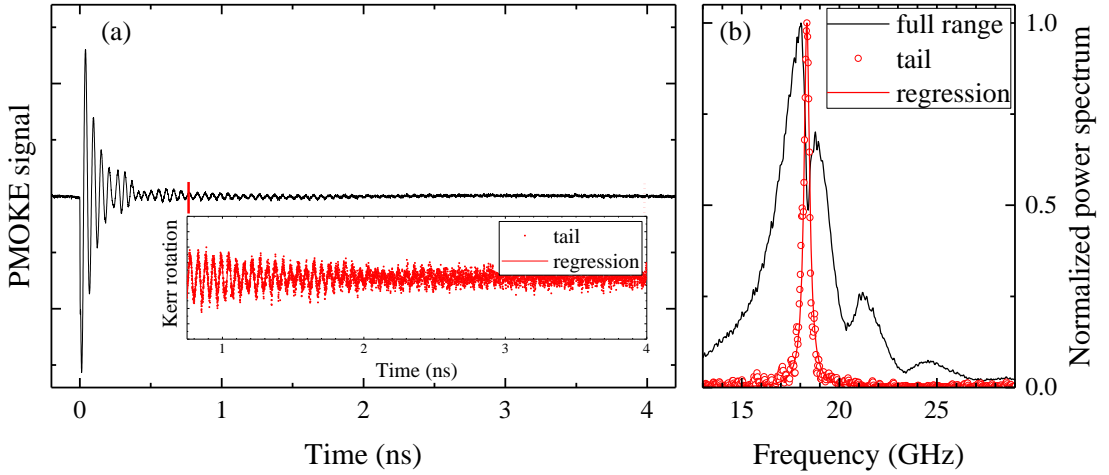


**Figure 4.5:** (a) TR-PMOKE measurement of a 105 nm Galfenol layer at  $\varphi_B = -22^\circ$  and  $B = 200$  mT (black line). (b) Normalized power spectra of the signals shown in (a).

fective FWHM is further referred to as effective linewidth. The regression of the tail is presented in the inset in figure 4.5(a), while a corresponding power spectrum is shown in red in figure 4.5(b). The evaluated frequency is  $f \approx 18.3$  GHz. The effective linewidth reads  $\Delta f_{\text{eff}} \approx 0.34$  GHz and corresponds to a lifetime of roughly  $\frac{1}{\pi \cdot 0.34 \text{ GHz}} \approx 1$  ns. The corresponding effective Gilbert damping parameter reads  $\alpha_{\text{eff}} = \frac{1}{2\pi f \tau_{\text{eff}}} = \frac{\Delta f_{\text{eff}}}{2f} \approx 0.01$ . This is in accordance with earlier experiments on optically excited ferromagnets, where  $\alpha_{\text{eff}} > 0.01$  [12],[90],[91]. In addition, figure 4.5(b) shows a frequency shift of the red spectrum compared to the lowest mode of the black spectrum. This frequency shift is due to a transient temperature change in the Galfenol nanolayer. As it is seen in figure 3.7 on page 43, the temperature changes drastically within the first ns and, therefore, also the magneto-crystalline anisotropy components, which determine the precession frequencies of the nanolayer [38].

To conclude, the 105 nm Galfenol nanolayer is characterized by localized discrete, but overlapping, magnon modes. In this experiment up to six magnon modes are being observed, where the lowest mode possesses the longest lifetime of roughly 1 ns with a corresponding effective linewidth of 0.34 GHz. The magnetic field dependence of all observed magnon modes is well described by the free energy density approach, where the angular dependence clearly shows the contribution of the magneto-crystalline anisotropy. In general, even higher magnon modes are expected, however, possessing very small precession amplitudes and broad linewidths.

#### 4.4 Transition from Multi-Mode to Single-Mode Magnetization Precession in Galfenol Nanolayers

This section focuses on the transition to ultrathin Galfenol layers with thicknesses of only several nm. These ultrathin samples have a 150 nm SiO<sub>2</sub> cap in order to amplify the magneto-optical Kerr effect [82]. The experimental configuration is the same as in the previous section. The magnetic field is set to  $B = 100$  mT and  $\varphi_B = -22^\circ$ <sup>7</sup>.

Figure 4.6(a) shows a comparison of several normalized PMOKE signals, which were being measured on a 4 (black), 5 (red), 20 (green), 60 (blue) and 105 nm (light blue) Galfenol nanolayer. The corresponding power spectra are shown in 4.6(b). The PMOKE

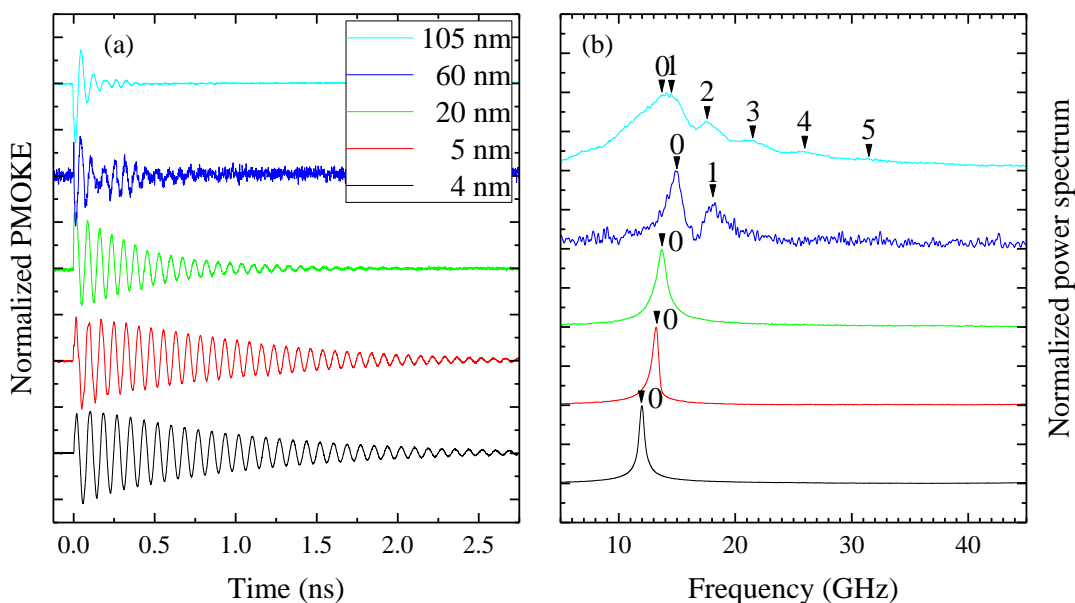


**Figure 4.6:** Comparison of (a) normalized PMOKE signals and (b) their power spectra for different Galfenol layers at  $B = 100$  mT and  $\varphi_B = -22^\circ$  except for the 60 nm layer, where  $\varphi_B \approx 0^\circ$ . For layer thicknesses  $\leq 20$  nm only one mode is present, while for the other layers at least one additional mode is present in the TR-PMOKE signal.

signal for the 105 nm nanolayer is similar to the previously discussed ones and possesses up to six magnon modes, which are indicated by black arrows. The lowest almost fully overlapping modes with  $n = 0$  and 1 appear as a single broad line in the power spectrum in figure 4.6(b) (light blue colour). By decreasing the layer thickness by roughly one half to 60 nm, the corresponding nanolayer possesses only two modes (blue colour). For this layer thickness, the degeneracy between the lowest magnon modes is lifted significantly, i.e.  $n = 0$  and 1. This is in accordance with equation 4.6, where a larger frequency splitting is expected for smaller layer thicknesses. For even thinner nanolay-

<sup>7</sup>Except for the 60 nm-thick nanolayer, where  $\varphi_B \approx 0^\circ$

ers, i.e.  $h \leq 20$  nm, finally, only a single mode contributes to the PMOKE signals. The single mode precession for a layer thickness of roughly 20 nm is in accordance with earlier reports [21],[89]. Hence, the single mode PMOKE signals are characterized by narrow ferromagnetic resonances with long lifetimes. Table 4.1 summarizes calculated values for the effective Gilbert damping parameters of the lowest mode of all discussed Galfenol layers. To do so, transient regressions following eq. 4.10 are used to fit the transient PMOKE signals. Due to the rich spectrum of nanolayers with  $h \geq 60$  nm, only the respective tails are being analyzed similar to the analysis in figure 4.5<sup>8</sup>. The evaluated effective Gilbert damping parameters are similar to earlier reported damping parameters in optically excited ferromagnetic layers [12],[90],[91]; where  $\alpha_{\text{eff}} > 0.01$ . However, table 4.1 clearly also shows  $\alpha_{\text{eff}} < 0.01$ . The evaluated values, which are

Thickness (nm)	$f$ (GHz)	$\Delta f_{\text{eff}}$ (GHz)	$\alpha_{\text{eff}} = \frac{\Delta f_{\text{eff}}}{2f}$
4	$17.1125 \pm 0.0003$	$0.3081 \pm 0.0006$	0.008
5	$18.2573 \pm 0.0006$	$0.384 \pm 0.001$	0.011
20	$18.751 \pm 0.001$	$0.677 \pm 0.002$	0.018
60	$20.129 \pm 0.006$	$0.15 \pm 0.01$	0.001
105	$18.332 \pm 0.003$	$0.344 \pm 0.005$	0.009

**Table 4.1:** Evaluated frequencies, linewidths and effective Gilbert damping parameters for different nanolayers corresponding to figure 4.6(a). In case of the presence of several magnon modes only the tail of the corresponding signal is taken. The difference in frequency and the linewidth of the 60 nm-thick layer are explained by a use of  $\varphi_B \approx 0$ , instead of  $\varphi_B = -22^\circ$  and need to be confirmed in additional measurements.

below 0.01, are close to the smallest damping parameters observed in ultrathin Iron layers grown on (001) GaAs substrates [92] or recently on ultrathin Galfenol layers on MgO substrates [89] by means of the FMR technique. However,  $\alpha_{\text{eff}} < 0.01$  have not been reported so far in experiments using ultrafast optical excitation in ferromagnetic materials. The small  $\alpha_{\text{eff}} \approx 0.001$  for the 60 nm is an interesting small value, however, it has to be verified in additional measurements. Besides the tails of the intermediate nanolayers, the ultrathin layers ( $h \leq 20$  nm) are characterized by a broadening of the effective linewidth with increasing layer thicknesses. The broadening of the effective linewidth is due to an increased dephasing of the magnetization precession by means of a non-uniformity of the magnetization distribution along the quantization axis [47], e.g. due to impurities. An additional feature is the increase of the single-mode's precession frequency for larger nanolayer thicknesses. Such frequency change is determined by the layer thickness and its corresponding value of the saturation magnetization (see Kittel formula in equation 2.15): an increase of the layer thickness is accompanied by an increase of the saturation magnetization [67].

<sup>8</sup>For the case of the 60 nm layer, the time windows starts at 0.5 ns, while for the 105 nm layer the single mode regime starts at approx. 0.75 ns.

In the following, a comparison of the magnetic field dependencies of all observed magnon modes' precession frequencies is presented (see figure 4.7). While the coloured dots indicate experimental dependencies, the coloured lines indicate calculated dependencies using the free energy density approach (equation 4.2) and the parameters in table 4.2. Starting from the left side of this figure, the known magnetic field dependence for the

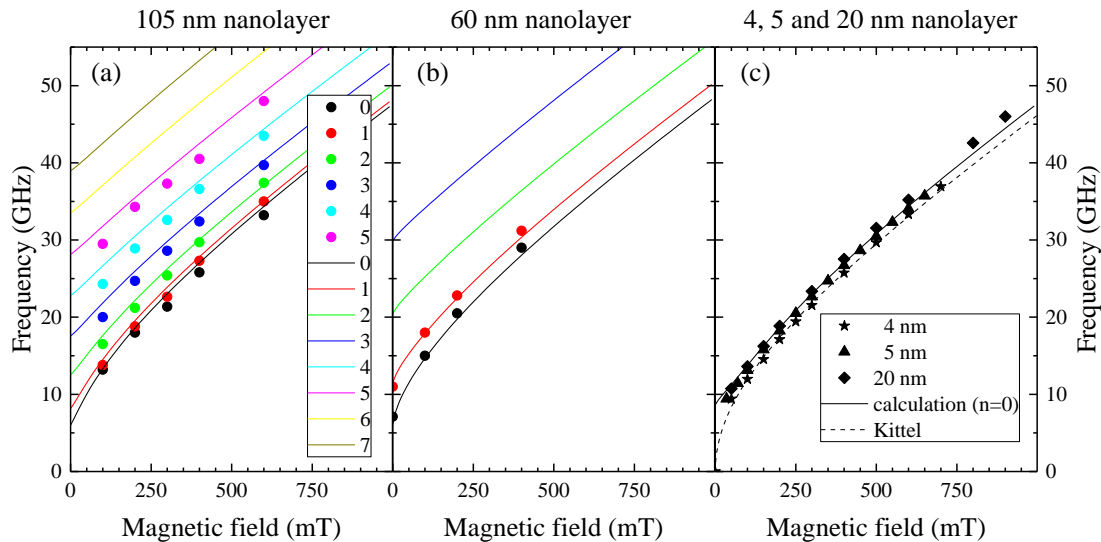


**Figure 4.7:** Comparison of magnetic field dependencies of certain magnon modes for all investigated Galfenol layers (symbols). Moreover, calculated curves using the free energy density approach are presented (lines). The used parameters for the calculation can be found in table 4.2. (a) Evaluated and calculated high-order magnon modes in the 105 nm layer. (b) For the 60 nm layer only two precession frequencies are observed. Calculated, but non-detectable high-order magnon modes are presented, as well. (c) Evaluated single magnon modes for layer thicknesses  $\leq 20$  nm (black symbols). All modes follow the magnetic field dependence of the calculated uniform mode ( $n = 0$ ) of the 4 nm nanolayer. Calculated high-order magnon modes of the 4 nm nanolayer are far above the shown frequency range.

105 nm-thick layer is shown again for the sake of completeness. As before, it contains observed and calculated magnon modes. The middle figure corresponds to the 60 nm layer and contains the magnetic field dependence of only two observable modes. It is important to mention that in this case,  $\varphi_B \approx 0$  and the PMOKE signal possesses only small precession amplitudes (see equation 4.9). Therefore, the observation of higher magnon modes is expected for  $\varphi_B \approx -22^\circ$  and also indicated by calculated coloured lines. The roughly twice-smaller 60 nm layer clearly shows an increased frequency splitting of the two lowest modes compared to the 105 nm layer due to the increased spatial confinement. The right part of figure 4.7 shows the magnetic field dependence of single precession modes for layer thicknesses  $\leq 20$  nm. All layers possess similar precession frequencies for the investigated magnetic field range. The black line corresponds to the calculated precession mode for the 4 nm-thick nanolayer, where expected high-order magnon modes possess much larger frequencies and are far above the shown frequency

Layer (nm)	$K_1$ (mT)	$K_u$ (mT)	$\mu_0 M_s$ (T)	$D$ (mT/nm <sup>2</sup> )
4	15	3	1.72	15
60	18	5	1.8	23
105	18	5	1.8	23

**Table 4.2:** Parameters for all considered layers, which are used for the calculated curves in figures 4.3(c), 4.4, 4.7, 4.9 and 4.10. The fitting parameters for the 4 nm-thick nanolayer are listed for the sake of completeness; however, they are carefully being discussed in the next section.

range of interest. The dashed black line corresponds to the simple Kittel formula (see equation 2.15), which describes the ferromagnetic resonance (FMR) of a ferromagnetic layer. As expected, the Kittel formula describes very well the observed single-mode precession frequencies of the ultrathin Galfenol nanolayer.

#### 4.4.1 Selective Excitation and Detection in Galfenol Nanolayers

The excitation of single- and multi-mode magnetization precession is qualitatively explained by the introduced thermal distribution of an absorbed fs optical pulse. The single-mode excitation is realized by means of layer thicknesses  $h$ , which are smaller than the optical penetration depth of the pump pulse  $\zeta_{\text{pu}}$ , i.e.  $h < \zeta_{\text{pu}}$ . In this case, the thermal distribution can be considered as homogeneous along the  $z$ -direction in the nanolayer; see solid red temperature distribution in figure 4.8(right). In addition, the 4, 5 and 20 nm nanolayers made of Iron yield heat diffusion times of approx. 1, 2 and 20 ps indicating an instantaneous thermal diffusion (see equation 3.11). Hence, a homogeneous thermal distribution allows no sign-changing profiles of the excited modes and results in a single-mode precession for ultrathin nanolayers  $\leq 20$  nm [12].

The excitation of multi-mode magnetization precession is realized by means of a non-homogeneous thermal distribution in the nanolayer. Such non-homogeneous distribution is introduced in nanolayers with a larger layer thickness than the optical absorption depth of the pump pulse, i.e.  $h > \zeta_{\text{pu}}$ . This results in a strong excitation near the surface of the nanolayer, which efficiently excites high-order magnon modes (see figure 4.8). The excitation of high-order magnon modes is due to the effective wave vector of the excitation, which is indicated as cut line in figure 4.8. The relation between the layer thickness  $h$  and the optical absorption depth  $\zeta_{\text{pu}}$  is a rough estimation for the excitation of the highest magnon mode number  $n_{\text{max}} = \frac{h}{\zeta_{\text{pu}}}$ . For the nanolayers with 4, 5, 20, 60 and 105 nm thickness, the relation yields  $n_{\text{max}} = \frac{h}{\zeta_{\text{pu}}} \approx 0, 0, 1, 3$  and 5, respectively, where a zero indicates only a single mode precession. This rough estimation describes surprisingly well the observed magnon mode numbers in figures 4.6 and 4.7. However, a more precise quantitative analysis deals with the spatial overlap between the optically induced temperature distribution and the dynamical magnetization. A

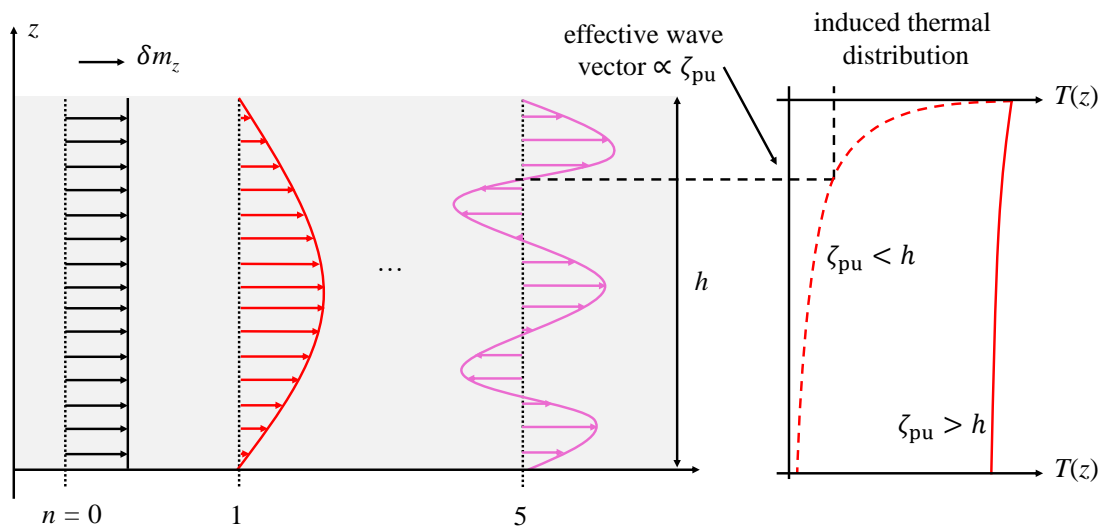


**Figure 4.8:** Visualization of the selective excitation of high-order magnon modes in metallic nanolayers. The optical absorption depth of the pump pulse  $\zeta_{pu}$  can be considered as an effective wave vector, which selectively excites localized magnon modes with specific wave vectors.

theoretical consideration of the spatial overlap between optically induced strain and the dynamical magnetization is given in [93]. An analogue consideration can be used to discuss the detection of single and high-order magnon modes by the probe pulse. In this case, the relation between the optical absorption depth of the probe pulse and the layer thickness has to be considered.

Besides the investigation of different layer thicknesses, different pump or probe wavelengths  $\lambda$  may be used to achieve different optical absorption depths  $\zeta \propto \lambda$  (see equation 3.8). In this case, second harmonic generation (SHG) can be utilized in order to significantly decrease respective wavelengths, which leads to smaller optical absorption depths and corresponding different responses of the magnetization precession in metallic nanolayers.

One advantage of the utilized optical excitation compared to the widely used ferromagnetic resonance (FMR) technique is the excitation of both even and odd magnon modes in the nanolayer. In the case of the FMR technique only odd modes are excited due the usage of the homogeneous distribution of the applied oscillating magnetic field [87]. The homogeneous distribution of the magnetic field possesses vanishing spatial overlap integrals with sign-changing profiles of even magnon modes. Hence, only odd magnon modes are excited by means of the FMR technique.



To conclude, ultrathin nanolayers with thicknesses  $\leq 20$  nm are characterized by a single magnetization precession. The transition from a multi-mode excitation to a single-mode excitation is clearly seen for different layer thicknesses in figures 4.6 and 4.7. The single-mode excitation occurs for layer thicknesses smaller than the optical absorption depth of the pump pulse and is characterized by a homogeneous temperature distribution in the nanolayer. The multi-mode excitation, however, appears due to a non-homogeneous temperature distribution and allows the excitation of sign-changing profiles, i.e. high-order magnon modes. The frequency splitting between the high-order magnon modes is determined by the layer thickness (see equation 4.6).

## 4.5 Characterization of Single-Mode Magnetization Precession in a 4 nm-thick Galfenol Nanolayer

This section focuses on the magnetic field and angular dependence of the single-mode magnetization precession in a 4 nm Galfenol nanolayer. The comprehensive study of these dependencies allows to obtain corresponding anisotropy parameters, as it was done for the 105 nm layer in section 4.3. The experimental configuration has not changed with respect to the previous measurements; i.e. pump energy density is  $0.3 \text{ mJ/cm}^2$ .

An analysis of the magnetic field dependence of the precession frequency is presented in figure 4.9(a). The dots indicate evaluated precession frequencies using the ASOPS technique, while the obtained value at  $B = 3 \text{ T}$  is being measured using an optical

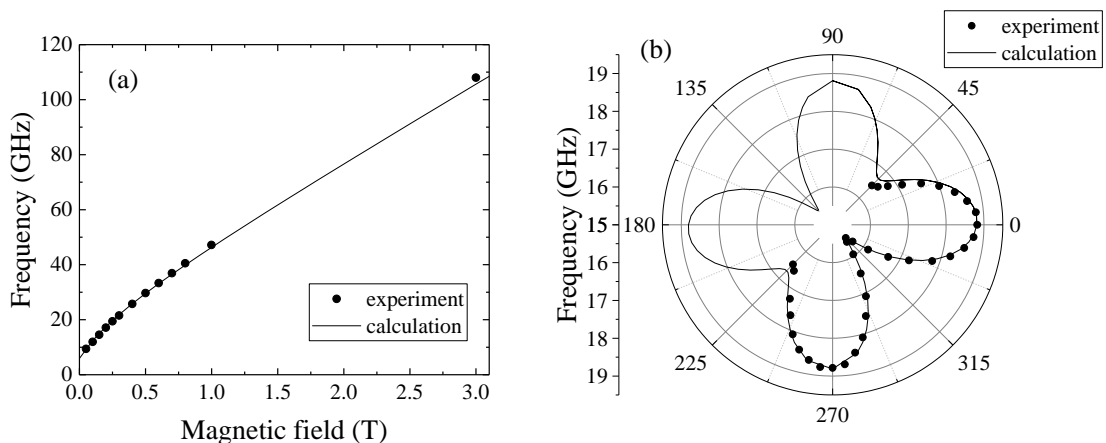


**Figure 4.9:** (a) Magnetic field dependence of the precession frequency. A calculation using the free energy density approach  $\varphi_B = -22^\circ$  is shown, as well (black line). (b) Angular dependence of the precession amplitude of a 4 nm Galfenol layer at a magnetic field strength of  $B = 200 \text{ mT}$ . The theoretical curve is calculated using the free energy density approach. The parameters used in this calculation are presented in table 4.2.

cryostat with a superconducting solenoid. In the latter case, the sample temperature is set to 150 K and a regenerative amplifier RegA (wavelength 800 nm, repetition rate 100 kHz) is used as a source for the pump and probe pulses. In order to monitor the temporal evolution of the magnetization, a standard mechanical scanning delay line is used. The precession frequency of roughly 100 GHz is currently the highest observed frequency in time-resolved experiments in metallic ferromagnets<sup>9</sup>. The black line is calculated using the free energy density approach in equation 4.2 and the following parameters:  $K_1 = 15$  mT,  $K_u = 3$  mT,  $\mu_0 M_s = 1.72$  mT and  $D = 15$  mT/nm<sup>2</sup>, which are in good agreement with previously reported values [38],[67]<sup>10</sup>. As it was done for the analysis of the 105 nm Galfenol nanolayer, the used anisotropy parameters are evaluated using the in-plane angular dependence of the precession frequency at  $B = 200$  mT (figure 4.9(b)). The presented angular dependence corroborates the four-fold symmetry of the cubic anisotropy, which is affected by the uniaxial anisotropy along the [110]-crystallographic direction. Such butterfly-like shape is similar to the one observed for the 105 nm Galfenol nanolayer in figure 4.4(a) on page 53.

Besides the changes of the precession frequency, the precession amplitude is significantly affected by the magnetic field strength and orientation, as well. Figure 4.10(a) presents the magnetic field dependence of the evaluated precession amplitude at  $\varphi_B \approx -22^\circ$ . The precession amplitude significantly decreases with an increasing magnetic field strength. As already discussed for the 105 nm layer in section 4.3, a theoretical model

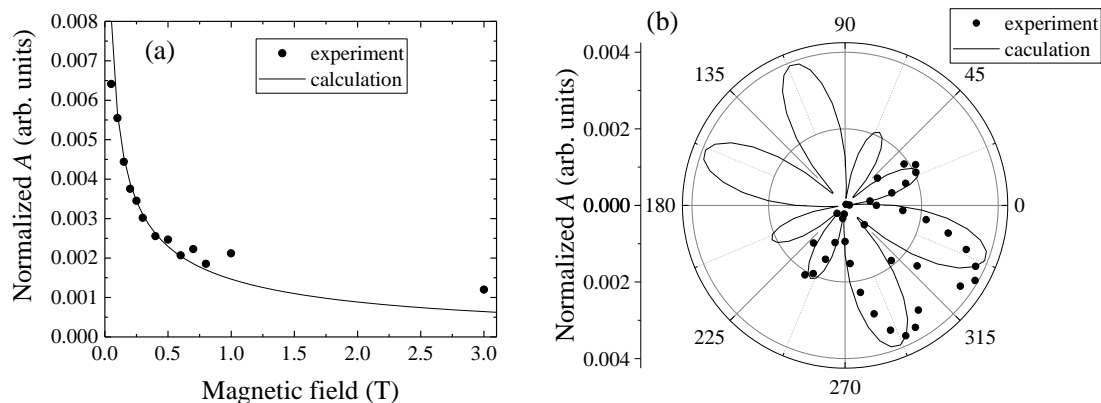


**Figure 4.10:** (a) Magnetic field dependence of the precession frequency at  $\varphi_B \approx -22^\circ$ . The black curve is calculated using equation 4.9, where  $\Delta K_1 = -3.7$  mT. (b) Angular dependence of the precession amplitude of a 4 nm Galfenol layer at a magnetic field strength of  $B = 200$  mT. The theoretical curves are calculated using the free energy density approach. The parameters used in this calculation are presented in table 4.2.

<sup>9</sup>Simulations in [94] show that in general precession frequencies in the THz frequency range are possible at 1 T.

<sup>10</sup>These parameters are also listed in table 4.2 on page 59 together with the fitting parameters for other investigated nanolayers.

describing the precession amplitude  $A(\varphi_B, B)$  is given in equation 4.9. For a qualitative analysis the evaluated precession amplitude is normalized to the calculated black curve<sup>11</sup> (equation 4.9), where the  $\Delta K_1$  is estimated to  $-3.7$  mT [38]. A good accordance between the experimental data and the theoretical curve is clearly observed. Therefore, we claim the observation of even larger precession frequencies in Galfenol nanolayer, finally reaching the THz frequency range.

The angular dependence of the precession amplitudes at  $B = 200$  mT is shown in figure 4.10(b). The angular dependence again reflects the four-fold symmetry of the cubic anisotropy, which is affected by the uniaxial anisotropy along the [110]-crystallographic direction. A decrease of the precession amplitude along the corresponding axes is clearly observed for the experimentally evaluated amplitudes, which reflects similar  $\Delta K_i$  as for the 105 nm Galfenol nanolayer. The theoretical line is being calculated using the free energy density approach, where the used parameters are:  $\mu_0 M_s = 1.72$  T,  $\Delta K_1 = -3.7$  mT and  $\Delta K_u = -0.8$  mT. The experimentally evaluated values are normalized to the theoretical curve accordingly.

A comprehensive analysis of the evaluated effective linewidth is given in the following part. Figure 4.11(a) shows evaluated  $\Delta f_{\text{eff}}$  of the single precession mode in a 4 nm Galfenol nanolayer. A linearly increasing effective linewidth is clearly seen for large magnetic fields. This behaviour is well-known in Iron multilayers [95] and related to Gilbert-like damping terms, such as purely intrinsic damping due to spin-orbit coupling [42] and eddy currents [43]. The latter one can be neglected due to a ultrathin iron-based nanolayer of only 4 nm thickness, which is much smaller than the skin depth of about 20 nm [46], [41]. An important extrinsic damping mechanism in this work is the two-magnon scattering [44], [96]. The inset of figure 4.11(a) shows the frequency dependence of the FMR peak-to-peak linewidth  $\mu_0 \Delta H \propto \Delta f_{\text{eff}}$  of a 16 nm Galfenol layer on a MgO(100) substrate [89]. According to the main figure a linearly increasing linewidth is being observed, as well, which indicates similar damping mechanisms in both nanolayers.

An unexpected additional feature in figure 4.11(a) is observed for magnetic fields  $\leq 200$  mT, where a decrease in the effective linewidth is observed. This effect is probably related to a thermally-induced non-linearity in the magnetization precession [97]. As already discussed for the 105 nm Galfenol nanolayer in figure 4.5, the transient change in the lattice temperature has a non-negligible influence on the anisotropy parameters and, therefore, on the precession frequency. As a result, the uniform mode of the 105 nm Galfenol nanolayer possesses different frequencies in the beginning and

---

<sup>11</sup>A similar normalization is done for the angular dependence of the precession amplitude in figure 4.10(b).

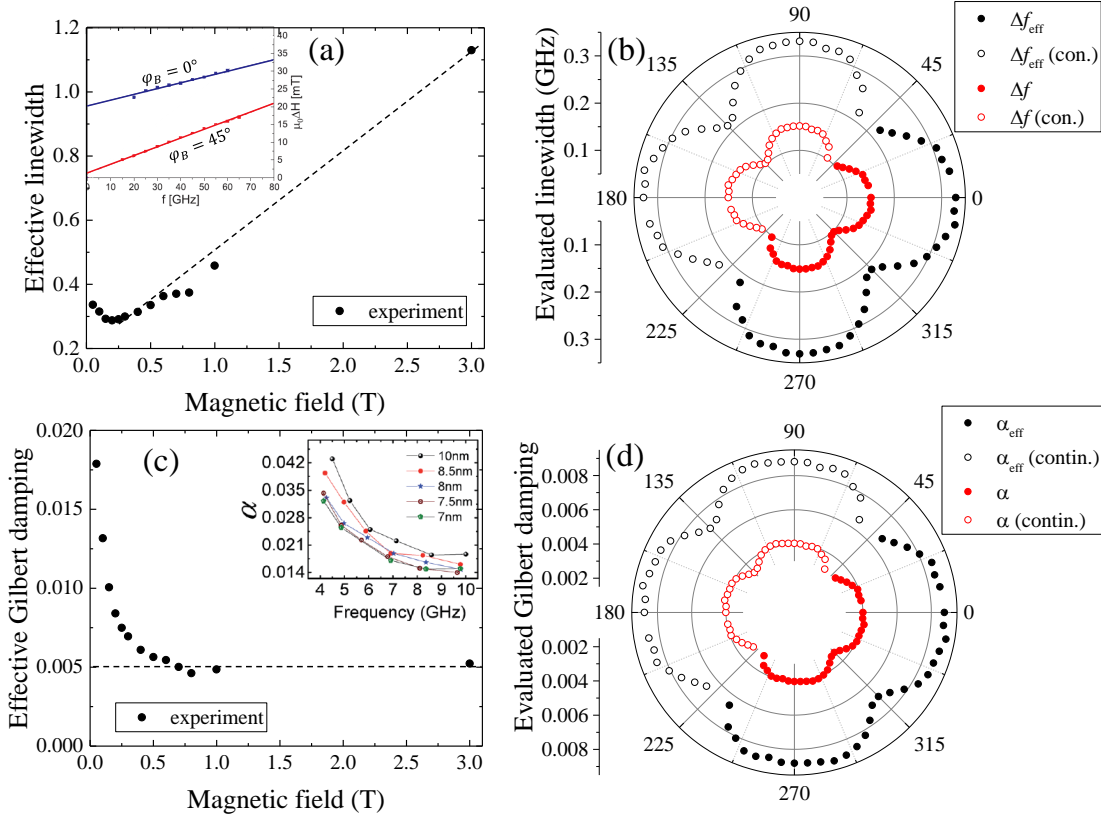


**Figure 4.11:** (a) Magnetic field dependence of the effective linewidth  $\Delta f_{\text{eff}}$  at  $\varphi_B = -22^\circ$ . The inset shows the frequency dependence of the FMR linewidth  $\mu_0\Delta H \propto \Delta f_{\text{eff}}$  in a 16 nm Gallenol layer by means of FMR spectroscopy; adapted from [89] (b) Angular dependence of  $\Delta f_{\text{eff}}$  and  $\Delta f$ . (c) Magnetic field dependence of the effective Gilbert damping parameter  $\alpha_{\text{eff}}$ . The inset shows the frequency dependence of evaluated Gilbert damping parameters for different ultrathin ferromagnetic multilayers [47]. (d) Angular dependencies of  $\alpha_{\text{eff}}$  and  $\alpha$  of a 4 nm Gallenol layer.

in the tail of the respective PMOKE signal. A similar temperature induced change of the magnetization precession occurs in the 4 nm nanolayer. A phenomenological explanation for the change in the lifetime is given by temperature induced changes of the anisotropy parameters  $K_i$ . For small magnetic fields, where  $B < K_i$ , the precession frequency  $f \propto K_i$  is mainly determined by the anisotropy parameters  $K_i$  and, therefore, strongly affected by thermally induced changes of  $K_i$  (see equation 4.2). Such transient change of the magnetization precession results in a broadening of the linewidth of the respective mode. For large magnetic fields, i.e.  $B > K_i$ , however, the precession frequency  $f \propto B$  is mainly determined by the external magnetic field  $B$  and, therefore, not much affected by the temperature of the solid. A possible explanation for a temperature dependent change in the linewidth is given by the two-magnon scattering with thermal magnons.

The in-plane angular dependence of  $\Delta f_{\text{eff}}$  is shown in figure 4.11(b) and possesses a

four-fold symmetry. In order to compensate for the influence by the MCA, equation 4.7 is used to calculate the compensated linewidth  $\Delta f^{12}$ . It is clearly seen that the MCA only affects the absolute values of linewidth by a factor of  $\approx 2$ , but not its four-fold symmetry. The observed anisotropy is known for Iron nanolayers on GaAs substrates and indicates extrinsic damping mechanisms, because a purely intrinsic Gilbert damping is isotropic and possesses no angular dependence [98]. A possible explanation for the angular dependence is given by the two-magnon scattering [95]. Recently, a similar angular dependence has been observed in a 16 nm Galfenol layer on a MgO substrate [89], where a direct link is given to the mechanism of two-magnon scattering.

Figure 4.11(c) presents the magnetic field dependence of the effective Gilbert damping parameter  $\alpha_{\text{eff}} = \frac{\Delta f_{\text{eff}}}{2f}$ . A clear decrease of  $\alpha_{\text{eff}}$  is observed for an increasing magnetic field strength; however, a saturation appears at  $\alpha_{\text{eff}} \approx 0.005$ . The saturation effect is due to both a linearly increasing linewidth  $\Delta f_{\text{eff}}$  and a linearly increasing precession frequency  $f$  (see figure 4.11(a) and 4.9(a)). Therefore, we suppose that for high magnetic fields the damping becomes purely intrinsic for ultrathin Galfenol nanolayers on GaAs substrates, however a contribution by the two-magnon scattering cannot be excluded completely [99]. A similar observation in Galfenol nanolayers on MgO substrates and in ferromagnetic multilayers have been recently reported in [89] and [47], respectively. For the sake of completeness, figure 4.11(b) presents the in-plane angular dependence of the experimentally observed effective Gilbert damping parameter  $\alpha_{\text{eff}}$  and respective calculated  $\alpha$ , which are strongly related to the angular dependence of  $\Delta f_{\text{eff}}$ ,  $\Delta f$  in figure 4.11(b).

To conclude, the observed magnetization precession of the 4 nm Galfenol nanolayer is well-described within the free energy density approach using two anisotropy contributions to the MCA, i.e. cubic anisotropy and uniaxial anisotropy. The fitted anisotropy parameters are similar to earlier mentioned parameters for Galfenol nanolayers. The experimentally observed effective Gilbert damping of  $\alpha_{\text{eff}} \approx 0.005$  is close to the smallest effective Gilbert dampings observed in metallic ferromagnets. The observed precession frequency of about 100 GHz at  $B = 3$  T is currently the largest precession frequency observed in metallic ferromagnets. It is likely that for very large magnetic fields the observed Gilbert damping is purely intrinsic and that it should be possible to observe THz precession frequencies. The anisotropic angular dependence of the effective Gilbert damping parameter at  $B = 200$  mT indicates a contribution by two-magnon scattering.

---

<sup>12</sup>Equation 4.7 can be adapted using  $\alpha = \frac{\Delta f}{2f}$ .

### 4.5.1 Observation of Brillouin oscillations in an Ultrathin Nanolayer

In the case of ultrathin nanolayers, where the penetration depth of the probe pulse is larger than the thickness of the ferromagnetic layer, an additional detection of the substrate is expected. Figure 4.12 shows a PMOKE signal at  $B = 3$  T and  $\varphi_B = -22^\circ$  with its corresponding power spectrum. Both the transient signal and the power spectrum indicate the contribution of more than one frequency. A regression using a sum of

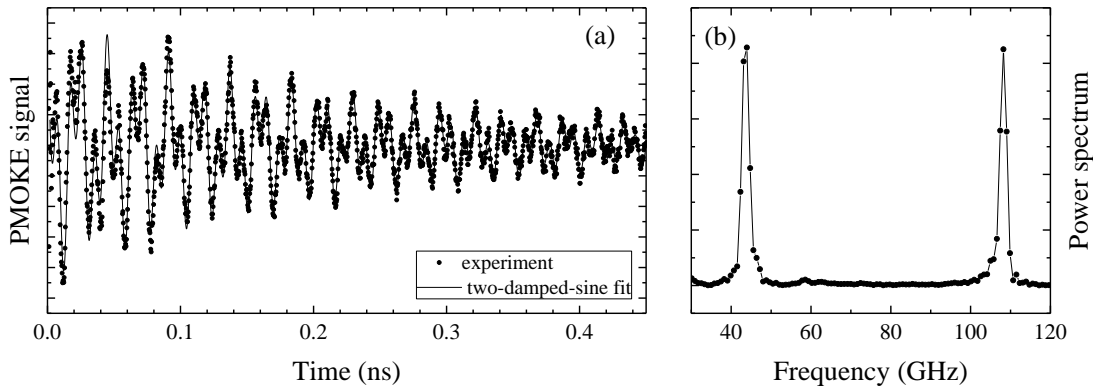


**Figure 4.12:** (a) Transient TR-PMOKE measurement and (b) its power spectrum performed on a 4 nm Gallenol layer for a magnetic field strength of  $B = 3$  T and direction of  $\varphi_B = -22^\circ$ . The line in (a) corresponds to a regression using two damped sin-functions (equation 4.10). The resonance in (b) at approx. 44 GHz corresponds to the so-called Brillouin oscillations and the resonance at approx. 108 GHz corresponds to the magnetization precession.

two damped sin-functions accordingly to equation 4.10 yield the frequencies of roughly 44 GHz and 108 GHz, respectively. A first estimation using the Kittel formula (equation 2.15) supposes a precession frequency of  $f_{\text{Kittel}}(3 \text{ T}) \approx 105$  GHz and, therefore, indicates the second mode as the corresponding precession frequency of the ferromagnetic layer. The contribution of the lower mode at roughly 44 GHz in figure 4.12(b) corresponds to so-called Brillouin oscillations, which are due to the detection of the propagating strain pulse in the GaAs substrate (see section 2.2.2). The corresponding observed frequency can be derived by

$$f_{\text{Brillouin}} = \frac{2n_{\text{GaAs}}v_L}{\lambda_{\text{pr}}} \quad (4.11)$$

$$\approx 45 \text{ GHz},$$

where  $n_{\text{GaAs}} = 3.679$  [100],  $\lambda_{\text{pr}} = 780$  nm and  $v_l = 4.731$  nm ps<sup>-1</sup> [53]. Due to the acoustic origin of the Brillouin oscillations, the same oscillations have to be observed in a reflection measurement. Figure 4.13(a) presents a reduced reflection signal without the thermal background. The full signal including the thermal background is shown in the corresponding inset. The reduced reflection signal clearly indicates an oscillating behavior, where the corresponding power spectrum in figure 4.13(b) yields a similar

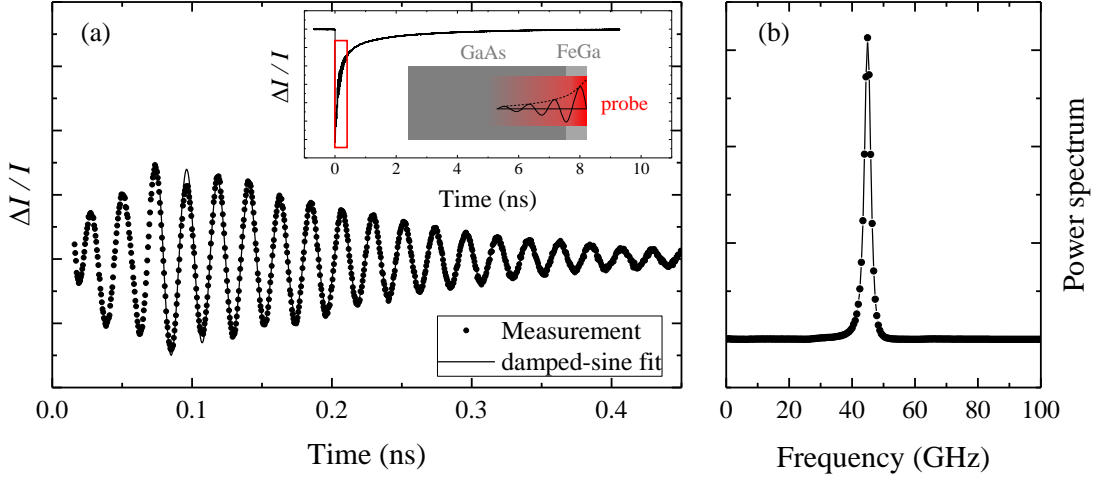


**Figure 4.13:** Analysis of a transient reflection signal measured on a 4 nm-thin Gallenol layer at  $B = 0$  T. (a) While the inset shows the measured transient signal in the time window of 10 ns, the main plot presents detected Brillouin oscillations of the signal with a subtracted background within the first half of a ns after the excitation at  $t = 0$ . (b) This plot demonstrates the power spectrum of the subtracted signal shown in (a). It can be clearly seen that only one frequency contributes to the signal.

frequency of roughly 45 GHz as for the calculated frequency of the Brillouin oscillations. The rising time of the transient reflection signal up to roughly 80 ps is due to the propagating strain pulse through the non-homogeneous probe profile inside the GaAs substrate [101]. The probe profile inside the GaAs substrate is described by a so-called sensitivity function, where its maximum lies usually not directly at the surface of the substrate but several hundreds of nm inside the substrate (see illustration in figure 4.13(a)) [59]. Therefore, the reduced transient reflection signal finds its maximum at the time, where the propagating strain pulse travels through the probe pulse's maximum sensitivity (for further information see figure 2.9 on page 18). It is important to mention that the observed Brillouin oscillations are contributing to all measured PMOKE signals, where the optical absorption depth of the probe pulse  $\zeta_{\text{pr}}$  is larger than the layer thickness  $h$ , i.e.  $\zeta_{\text{pr}} > h$ . But in the case of small magnetic fields, i.e.  $< 1$  T, the contribution given by the Brillouin oscillations is negligible with respect to the contribution by the magnetization precession.





## Chapter 5

# Strong Magnon-Phonon Coupling in a Ferromagnetic Nanograting

In spintronics, the usage of radio-frequency acoustic waves is a promising tool for the spin control in nanostructured magnetic devices [102],[103],[15]. The manipulation of the spin system is realized by the magneto-elastic coupling between excited spin waves (magnons) and elastic waves (phonons). In the case of strong coupling and respective long lifetimes, the interacting magnons and phonons can result in a formation of a hybridized state, which is known as magnon polaron [25],[26]. The transient observation of a magnon polaron in ferromagnetic metals is being extremely challenging due to short lifetimes and a weak magneto-elastic coupling<sup>1</sup>. The main part of this chapter presents the overcoming of these limitations by means of a selective interaction of corresponding magnon and phonon modes in a shallow Gallenol nanograting (NG).

The investigated sample is characterized in section 5.1. Then, high-Q phonon modes, which are localized in the NG are theoretically discussed and experimentally evaluated in sections 5.2 and 5.3.1, respectively. The experimental observation of magnon polarons is given in section 5.3.2, where two magnon-phonon resonances are characterized separately and, finally, analyzed within the model of coupled harmonic oscillators. Afterwards in section 5.4, the magnetic field dependence of localized magnon modes is discussed for three azimuthal angles of  $\varphi_B = 0^\circ, 45^\circ$  and  $90^\circ$ .

---

<sup>1</sup>The first observation of strong magnon-phonon coupling in Nickel nanomagnets was reported last year [27].

## 5.1 Sample Characterization

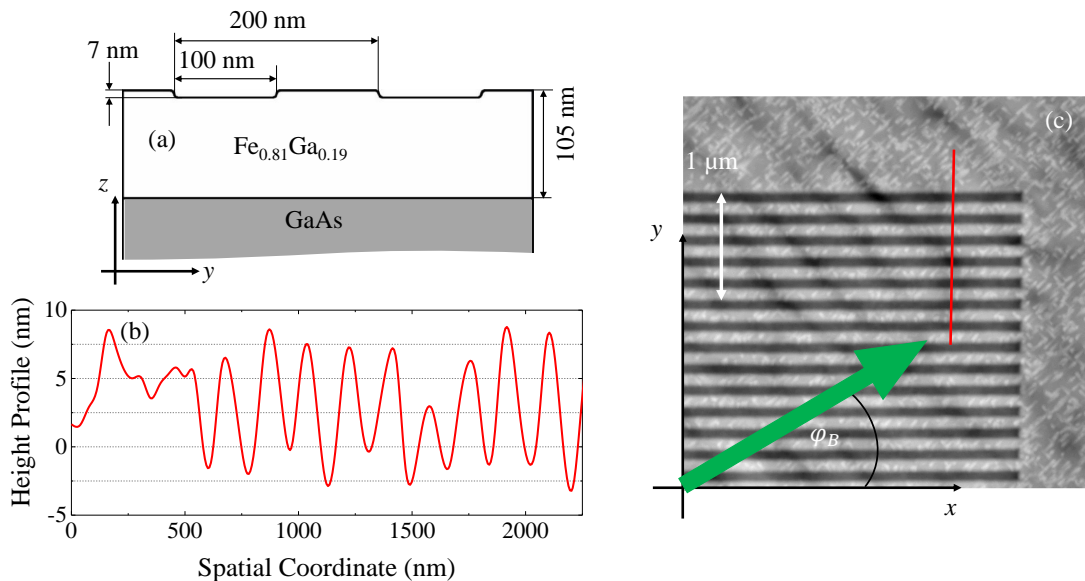


**Figure 5.1:** (a) Side view of the used sample containing a NG with an average depth of roughly 7 nm. (b) Experimentally measured height profile of the NG using an atomic force microscope by Bruker with a NCHV-A probe. (c) A two-dimensional height profile shows the surface structure and a corner of the NG. The red line indicates the slice used for the one-dimensional height profile in (b). The AFM measurement has been produced jointly with Dmytro D. Yaremkevich.

The sample is given by a physical nanograting (NG), which was formed by milling parallel grooves in the Gallenol sample surface along the [100]-crystallographic direction by means of a focused beam of Ga ions<sup>2</sup>. As in the previous chapter the 105 nm Gallenol ( $\text{Fe}_{0.81}\text{Ga}_{0.19}$ ) nanolayer was epitaxially grown on a (001) semi-insulating GaAs substrate and, finally, capped with a 3 nm Cr layer. Figure 5.1(a) shows a schematic of the nanolayer with the introduced NG. The NG of  $25 \times 25 \mu\text{m}^2$  size possesses a symmetric patterning with a width of  $w = 100 \text{ nm}$  and a period of  $p = 200 \text{ nm}$ . The average NG depth of roughly  $h = 7 \text{ nm}$  is being estimated using an atomic force microscope by Bruker with a NCHV-A probe; see figure 5.1(b). A two dimensional AFM height profile of a corner of the NG is presented in figure 5.1(c), where the red line corresponds to the one dimensional height profile in figure 5.1(b). The milled grooves along the [100]-crystallographic direction are clearly seen as parallel black lines. The profile outside of the NG shows the surface, where the surface roughness is estimated to be of several nm. The small white spots around the sample surface may indicate the grain structures of Gallenol [104] and Chromium [105]. The geometry of the applied magnetic field is the same as it is in chapter 4, where the magnetic field is applied in-plane with an angle

<sup>2</sup>The NG was produced by Raith using a VELION FIB-SEM fabrication tool.

$\varphi_B$  to the [100]-crystallographic direction.

## 5.2 Localized Phonon Modes

In chapter 4, the magnetization precession of different Gallenol nanolayers was discussed in detail. Corresponding magnetization precession frequencies lie in the range of several GHz ( $B < 300$  mT). In order to manipulate such magnetization responses, radio-frequency (rf) acoustic waves are of primarily interest in the work. A physical NG, as it is introduced in the previous section, is utilized as an acoustic resonator, which modulates the shape of the nanolayer. Due to the periodic pattern of the NG, only certain acoustic modes with specific frequencies are localized within the NG [15]. Such localized acoustic waves can be considered as standing waves<sup>3</sup>. Due to the localization at the surface of the layer, the mentioned acoustic waves are better known as Rayleigh waves or surface acoustic waves (SAW) [106] (see section 2.2.2). The corresponding frequencies in the NG are mainly determined by the lateral sizes of the NG, i.e. the width  $w = 100$  nm and period  $p = 200$  nm. In a simplified manner, the NG period determines the SAW wavelengths, which correspond to frequencies of roughly  $\frac{p}{v_1/2} \approx 13$  GHz<sup>4</sup>.

A more detailed analysis of localized SAWs in NGs is provided by COMSOL Multiphysics<sup>®</sup> (COMSOL) [107]. COMSOL is a finite element analysis software, which combines a variety of different physical modules, e.g. acoustics, wave optics and heat transfer. The geometry of the sample is modeled using a finite mesh. As a result, the atom displacements and strain distributions of all localized SAWs can be calculated and visualized. In addition, the wave optics and heat transfer modules can be used to calculate only optically excitable SAWs by a fs pump pulse<sup>5</sup>. Figure 5.2 shows the atom displacements of two calculated excitable SAWs in an NG of 7 nm depth. The mode illustrated in figure 5.2(a) is a Rayleigh-like standing wave with a dominant displacement along the  $z$ -direction, which is perpendicular to the surface (red arrows indicate the direction of displacement). As the wave vector is determined perpendicular to the grating grooves, i.e. along the  $y$ -axis, the mentioned acoustic mode is further referred to as quasi-transverse acoustic (QTA) mode. The other mode illustrated in figure 5.2(b) possesses a dominant in-plane displacement along the  $y$ -direction (blue arrows indicate the direction of displacement) and is known as surface skimmed longitudinal mode [24]. Because of its dominant in-plane polarization, this mode is further referred to as quasi-longitudinal acoustic (QLA) mode [108]. Both modes possess a symmetry of

<sup>3</sup>The used pump spot with a diameter of roughly  $10 \mu\text{m}$  is much larger than the optical absorption depth of 20 nm (see sections A.1 and 3.3.2).

<sup>4</sup>The sound velocities for SAWs is half of the respective sound velocities in bulk.

<sup>5</sup>The optical excitation is calculated using the two-temperature model (see section 2.2.1).

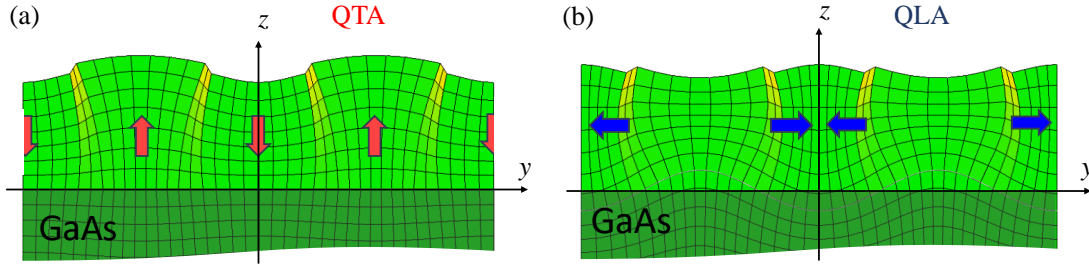


**Figure 5.2:** Calculated deformed meshes illustrating the atom displacement of two symmetric localized acoustic modes in a 7 nm deep NG. The layer thickness is 105 nm. (a) This mode corresponds to a quasi-transversal acoustic (QTA) mode and is characterized by a larger displacement perpendicular to the surface. (b) This mode is called quasi-longitudinal acoustic (QLA) mode due to its larger in-plane displacement. The coloured arrows indicate the directions of the atom displacement. Both modes are Rayleigh-like standing waves. All spatial profiles presented in this chapter were calculated by Serhii M. Kukhtaruk.

displacement with respect to the center of the grooves and are further called symmetric modes. The calculated frequencies for the QTA and QLA modes in a 7 nm deep NG are 13.1 GHz and 15.3 GHz, respectively. Moreover, calculations show that both modes are excited simultaneously with similar amplitudes and lifetimes, where the main damping mechanisms are given by an escape to the substrate and non-idealities of the grating parameters.

The above discussed excitable acoustic modes are characterized by a symmetric distribution of displacement with respect to the centre of the grooves; see figure 5.2. The relation between the excitability and symmetry of displacement is understood considering the overlap integral of the introduced temperature gradient by the fs pump pulse and the atom displacement. Due to the normal incidence of the fs pump pulse, only the  $z$ -direction has to be considered. This results in a symmetric normalized temperature gradient  $\frac{\partial \tilde{T}_1}{\partial z}$ <sup>6</sup>. Hence, only displacements with a symmetric distribution of the normalized displacement  $\tilde{u}_z$  lead to non-zero overlap integrals, i.e.  $\int \tilde{u}_z \frac{\partial \tilde{T}_1}{\partial z} dz \neq 0$ <sup>7</sup>. Besides the discussed excitable symmetric modes, so-called antisymmetric counterparts are localized within the NG. In the following, the case of symmetric and antisymmetric modes is exemplarily discussed for the QTA mode. Visualizations of atom displacements of the cosine-like symmetric QTA mode and the sine-like anti-symmetric QTA\* mode are presented in figure 5.3. The QTA and QTA\* modes slightly lift their degeneracy in frequency due to Bragg reflections and interferences in the NG [109], however their calculated frequency splitting does not exceed 0.1 GHz. In addition, calculations show that both modes possess similar lifetimes. Due to the antisymmetric distribution of

<sup>6</sup>  $\int \left( \frac{\partial \tilde{T}_1}{\partial z} \right)^2 dV = 1$ , where  $dV$  is a dimensionless unit volume element.

<sup>7</sup>  $\int \tilde{u}_z^2 dV = 1$ , where  $dV$  is a dimensionless unit volume element.

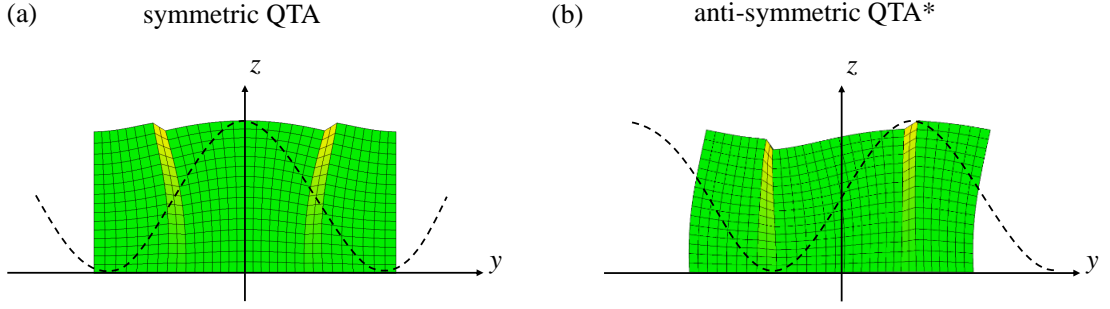


**Figure 5.3:** Calculated deformed meshes illustrating the atom displacement  $\tilde{u}_z$  of the (a) symmetric QTA and (b) antisymmetric QTA\* mode in a 7 nm deep NG.

the atom displacement  $u_z$  of the QTA\* mode, the QTA\* mode can neither be optically excited nor detected by normal incident pump and probe pulses, i.e.  $\int \tilde{u}_z \frac{\partial \tilde{T}_1}{\partial z} dz = 0$ .

Due to the NG symmetry only the  $yz$ -plane has to be considered. Therefore, there are only two non-zero components of the atom displacement, i.e.  $u_y$  and  $u_z$ . This means that the introduced acoustic modes have only three non-zero dynamical strain components, i.e.  $\eta_{zz}$ ,  $\eta_{yy}$  and  $\eta_{yz}$ . The consideration of dynamical strain components is

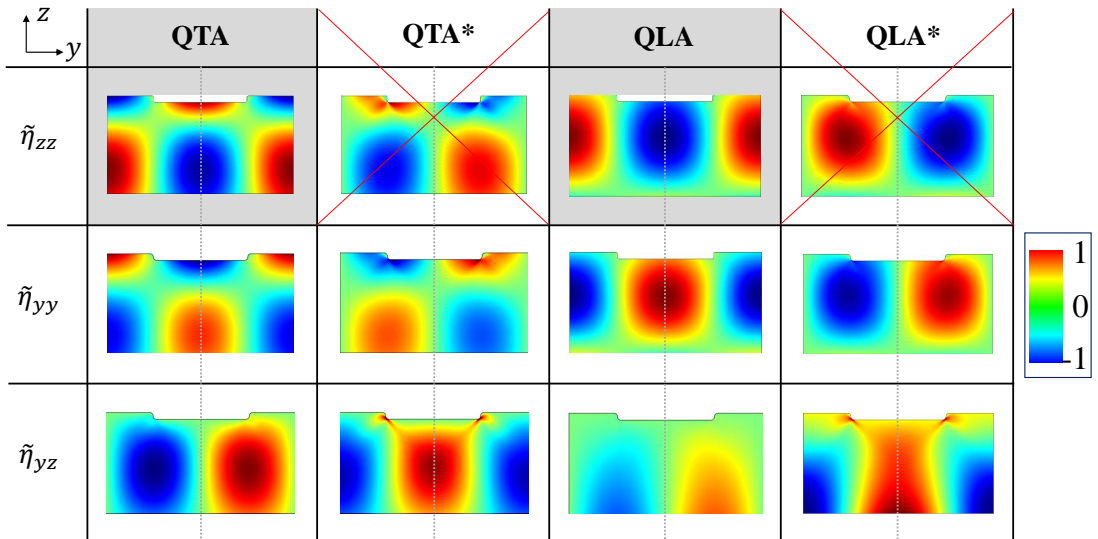


**Figure 5.4:** Spatial distributions of all normalized non-zero dynamical strain components, i.e.  $\tilde{\eta}_{zz}$ ,  $\tilde{\eta}_{yy}$  and  $\tilde{\eta}_{yz}$ . The grey box indicates optically excitable phonon modes with symmetric  $\tilde{\eta}_{zz}$  components. Due to the symmetric temperature distribution introduced by the optical pump pulse, only such symmetric phonon modes are excitable. The red cross, however, indicates non-excitable phonon modes with antisymmetric  $\tilde{\eta}_{zz}$  components. The dotted gray line indicates the plane of symmetry.

important in the next section, when the magnon-phonon coupling is discussed in detail.

Figure 5.4 illustrates normalized non-zero dynamical strain components for the QTA, QTA\*, QLA and QLA\* mode<sup>8</sup>. The grey marked modes indicate the excitable QTA and QLA mode due to their symmetric  $\tilde{\eta}_{zz}$  distributions. The QTA\* and QLA\* mode, however, possess antisymmetric  $\tilde{\eta}_{zz}$  distributions, which indicate prohibited excitations by the fs pump pulse (red cross). The main idea of figure 5.4 is to show that each phonon mode possesses both symmetric and antisymmetric strain distributions. A close look shows that if the axial strain components  $\eta_{zz,yy}$  are symmetric, then, the shear strain component  $\eta_{yz}$  is antisymmetric and vice versa. Moreover, the similar axial strain components  $\eta_{zz,yy}$  have their only difference in a  $\pi$ -phase shift to each other. The variety of strain distributions in figure 5.4 is discussed in detail later in this chapter, when the selective coupling of certain phonon and magnon modes is considered.

To conclude, two excitable phonon modes are localized in the NG, i.e. a quasi-transverse acoustic (QTA) and a quasi-longitudinal acoustic (QLA) mode with respective calculated frequencies of 13.1 and 15.3 GHz. Both modes possess non-excitable anti-symmetric counterparts with similar frequencies and lifetimes.

---

<sup>8</sup>The components are normalized according to  $\int \tilde{\eta}_{yy,yz}^2 dV = 1$  ( $dV$  is a unit volume element).

### 5.3 Characterization of Magnon-Phonon Resonances

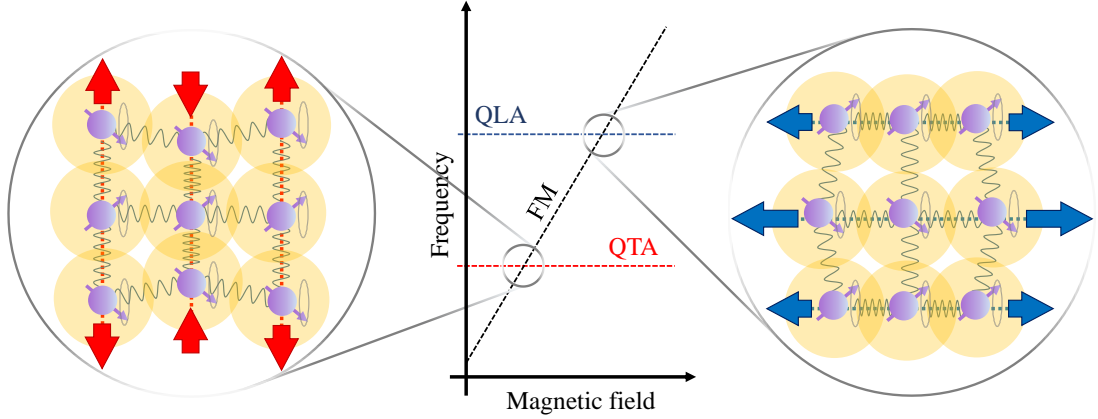


**Figure 5.5:** Principle of magnon-phonon resonance experiments. The schematic shows electron spins (purple), which are coupled through the lattice (grey springs) and the exchange interaction (yellow areas). The motion of precession is indicated as well as the lattice displacement (coloured arrows).

The basic principle of magnon-phonon resonance experiments is illustrated in figure 5.5. In this case, the magnetization precession is tuned into resonance with excited phonon modes by means of a uniform external magnetic field  $B$ . The occurring crossing points characterize magnon-phonon resonances, which result in the hybridization of respective magnon and phonon modes. Quantitatively, the hybridization is described by the cooperativity

$$C = \frac{4K^2}{\Delta f_{\text{ph}} \cdot \Delta f_{\text{mag}}}, \quad (5.1)$$

where  $K$  is the coupling strength and  $\Delta f_{\text{ph}}$  and  $\Delta f_{\text{mag}}$  are respective individual linewidths (FWHMs) of the phonon and magnon mode. The main object of study is the interaction of the so-called fundamental magnon (FM) mode of the patterned Galfenol nanolayer with two localized phonon modes, i.e. QTA and QLA; see figure 5.5. The magnetization precession in an unpatterned 105 nm Galfenol nanolayer was carefully discussed in the previous chapter. Due to the absence of localized phonon modes in the unpatterned nanolayer, the unperturbed linewidth of the FM mode can be estimated to  $\Delta f_{\text{FM}} = 0.34 \text{ GHz}$  (see table 4.1 on page 57). The experimental evaluation of unperturbed phonon lifetimes is given in the following section.

### 5.3.1 Experimental Evaluation of Unperturbed Phonon Lifetimes

In Gallenol NGs, the magnetic field orientation  $\varphi_B$  determines the interaction between the dynamical strain and the dynamical magnetization [15]. In particular, the  $z$ -component of the torque density acting on the magnetization precession reads [15]

$$Q_z = -b_1 M_s \eta_{yy} \sin(2\varphi_B), \quad (5.2)$$

where  $\eta_{yy}$  is the in-plane dynamical strain component. Therefore, a magnetic field orientation parallel to the grooves along the [100]-crystallographic direction ( $\varphi_B = 0^\circ$ ) results in a vanishing influence of the dynamical strain on the magnetization precession. Due to a systematic error in the alignment of the magnetic field orientation, a magnetic field of  $B = 250$  mT is used in order to additionally shift the excited magnetization precession to high frequencies far above the phonon frequencies. Hence, the excited phonon modes can be considered as unperturbed by the magnetization precession for the discussed experimental configuration.

Figure 5.6(a) presents an experimentally measured transient reflection signal using frontside excitation and the experimental conditions of  $\varphi_B = 0^\circ$  and  $B = 250$  mT. Pump and probe energy densities per pulse are  $5.5$  mJ/cm<sup>2</sup> and  $1.4$  mJ/cm<sup>2</sup>, respectively. The probe polarization is adjusted perpendicular to the grooves in order to have a maximum strain contribution to the reflection signal (see section A.6). The inset of figure 5.6(a) shows a fraction of the transient signal with subtracted thermal background. In addition, a regression using a damped-sine function (see equation 4.10) is shown in red. The evaluated phonon frequency and linewidth read  $f_{\text{QTA}} = 12.94$  GHz and  $\Delta f_{\text{QTA}} = (0.059 \pm 0.001)$  GHz, respectively. With respect to the calculated QTA mode with a frequency of  $13.1$  GHz, the observed phonon mode is identified as the QTA

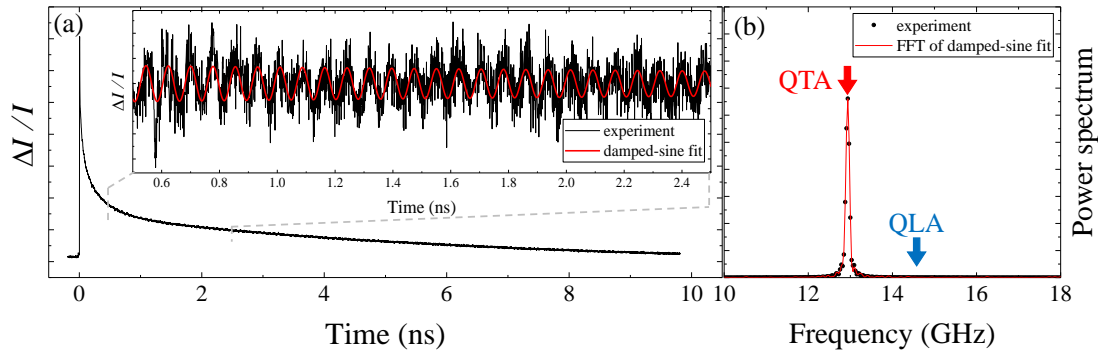


**Figure 5.6:** Evaluation of a transient reflection signal of a 7 nm deep NG using frontside excitation, where  $\varphi_B = 0$  and  $B = 250$  mT. The evaluated phonon frequency  $f_{\text{QTA}} = 12.94$  GHz and the evaluated linewidth  $\Delta f_{\text{QTA}} = (0.059 \pm 0.001)$  GHz.



mode<sup>9</sup>. By considering the frequency spectrum in figure 5.6(b) the narrow line of the QTA mode is clearly seen at 13 GHz. The absence of the QLA mode in the reflection signal is due to its specific polarization and material specific photo-elastic constants; see section 2.2.2, especially equation 2.32. However, its contribution is clearly detected in transient PMOKE signals, where the frequency is estimated to  $f_{\text{QLA}} = 14.6$  GHz.

### 5.3.2 Selective Coupling of Optically Excited Magnon and Phonon Modes

The previous section focused on the reduction of the magneto-elastic interaction in order to evaluate the unperturbed lifetime of the QTA mode. For the investigation of strong magneto-elastic coupling, however, a maximal magneto-elastic interaction is intended. Therefore, all following measurements are performed for a magnetic field orientation of  $\varphi_B = 45^\circ$  (see equation 5.2) using backside excitation. Pump and probe energy densities are similar to the ones used in the previous section.

In the following, the magnetic field dependence of transient PMOKE signals is of primary interest. In this case, the probe polarization is adjusted parallel to the grooves in order to have a minimum strain contribution to the reflection signal (see section A.6). In order to discuss the magnetic field dependence of measured PMOKE signals in the frequency domain, FFTs are performed for each transient PMOKE signal, where the magnetic field range varies from 0 to 250 mT with a step size of 5 mT. Figure 5.7 summarizes the main experimental observations. Figure 5.7(a) shows a so-called colour plot presenting the magnetic field dependence of evaluated PMOKE spectra. The colour is a measure for the spectral amplitude in the frequency domain. The colour plot contains two horizontal lines with frequencies at 13.0 and 14.6 GHz, respectively. Both modes correspond to the already mentioned QTA and QLA mode, i.e.  $f_{\text{QTA}} = 13.0$  GHz and  $f_{\text{QLA}} = 14.6$  GHz. The magnetic field dependent mode, which finds two resonance conditions with both localized phonon modes, corresponds to the FM mode of the 105 nm Galfenol nanolayer. Considering magnetic fields  $> 60$  mT, the FM mode possesses a linear frequency dependence on  $B$  according to<sup>10</sup>

$$f_{\text{FM}} = (7.12 \pm 1.23) \text{ GHz} + (0.05 \pm 0.01) \text{ GHz mT}^{-1} \cdot B. \quad (5.3)$$

Therefore, the detuning of the FM mode's precession frequency relatively to the phonon modes is realized by changing the external magnetic field strength. The main focus is on the magnon-phonon resonance conditions at roughly  $B_{\text{QTA}} = 110$  mT, where

---

<sup>9</sup>The visible mode cannot be the QTA's antisymmetric counterpart, QTA\*, because the mode is visible and therefore excited.

<sup>10</sup>The frequency offset of roughly 7 GHz is determined by anisotropy contributions to the free energy density and mainly influenced by the orientation of the external magnetic field (see figure 4.3 on page 52).

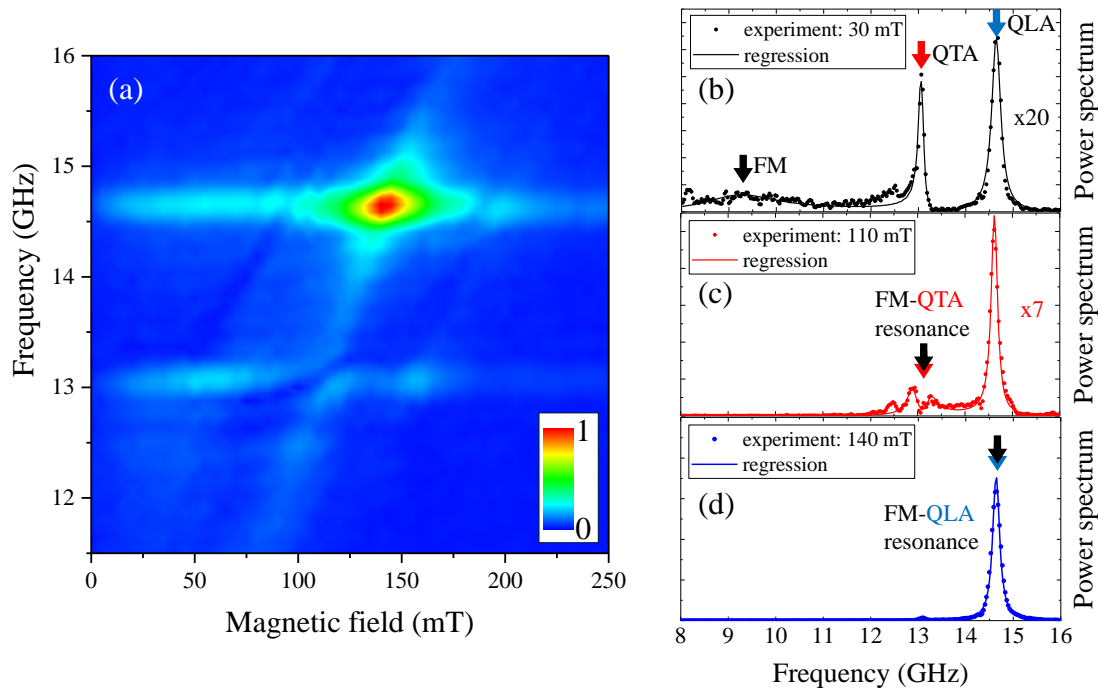


**Figure 5.7:** (a) Colour plot of PMOKE spectra for backside excitation. Moreover, exemplary PMOKE spectra at (b) 30, (c) 110 and (d) 140 mT. The latter two correspond to the FM-QTA and FM-QLA resonance, respectively. A careful discussion of the transient analysis is given in section A.4.

$f_{\text{FM}} = f_{\text{QTA}}$ , and  $B_{\text{QLA}} = 140$  mT, where  $f_{\text{FM}} = f_{\text{QLA}}$ , respectively. Both resonances are further referred to as FM-QTA and FM-QLA resonance. Exemplarily evaluated PMOKE spectra at magnetic fields of  $B = 30$ , 110 and 140 mT are additionally shown in figure 5.7(b), (c) and (d)<sup>11</sup>. For small magnetic fields at  $B = 30$  mT the indicated FM mode is clearly out of resonance with both phonon modes, however, non-zero spectral amplitudes are observed for the QTA and QLA mode. A possible explanation is given by the interaction with high-order magnon modes in the 105 nm Galfenol nanolayer [88] (see last chapter) or NG specific magnon modes [110] (see section 5.4).

Figures 5.7(c) and (d) show respective evaluated power spectra for the FM-QTA and the FM-QLA resonance. The lower FM-QTA resonance is characterized by a frequency splitting around  $f = f_{\text{FM}} = f_{\text{QTA}}$ , which indicates the avoided crossing effect. The observed avoided crossing is a direct evidence for the hybridization of optically excited magnon and phonon modes, i.e. the formation of a magnon polaron. It is the first observation of the formation of a magnon polaron in ferromagnetic metals in transient experiments. The higher FM-QLA resonance is characterized by a strong amplification of the PMOKE's spectral amplitude, which is clearly seen as a red spot in figure

<sup>11</sup>The detailed fitting procedure is presented in section A.4.

5.7(a). The large PMOKE amplitude in resonance is the result of resonant phonon driving, which is similar to the results in earlier reports [111],[14],[15]. However, despite the phonon driving no avoided crossing is observed for the FM-QLA resonance as it is observed for the FM-QTA resonance. The understanding of these two qualitative differences in the resonant behaviour is the aim of this section.

In order to determine the observed frequency splitting of the avoided crossing, figure 5.8(a) presents an evaluation of spectral amplitudes around the FM-QTA resonance. The evaluated frequency splitting reads  $\Gamma \approx 0.4$  GHz, which leads to a cooperativity at the FM-QTA resonance of

$$C_{\text{QTA}} = \frac{\Gamma^2}{\Delta f_{\text{QTA}} \Delta f_{\text{FM}}} \approx 7.8 \gg 1, \quad (5.4)$$

where  $\Gamma \approx 2K_{\text{QTA}}$ . The high cooperativity is a clear evidence for the strong magnon-phonon coupling regime and ensures the periodic conversion of energy between the magnonic and phononic system at high fidelity. Due to the coupled state of the excited magnon and phonon mode, a similar avoided crossing is expected in the reflection signal, which serves to detect the dynamical strain in the NG, i.e. phonons. Figure 5.8(b) presents a normalized colour plot of experimentally measured reflection spectra around the FM-QTA resonance similar to figure 5.8(a). An absence of the avoided crossing is

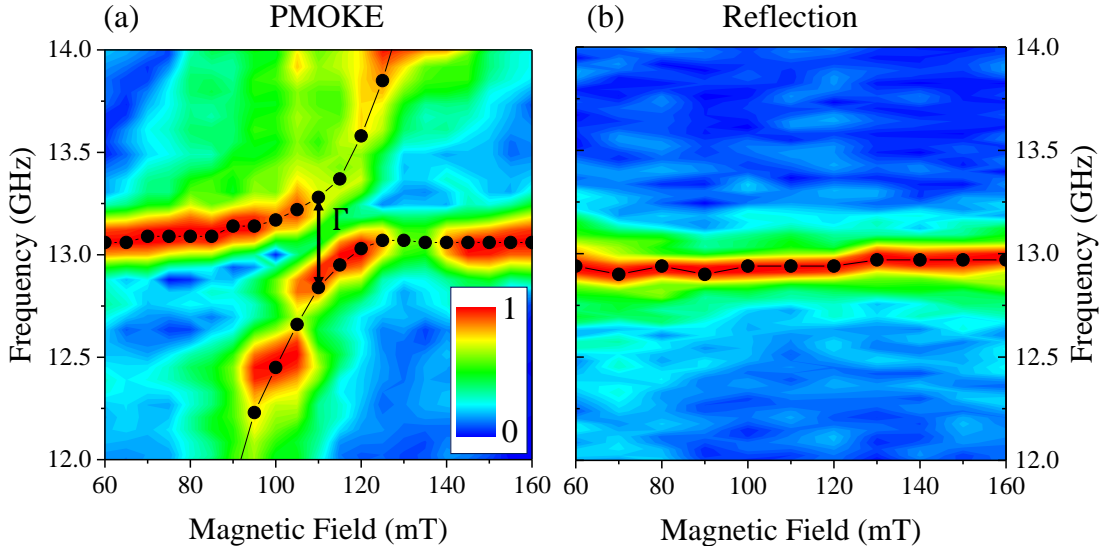


**Figure 5.8:** (a) Normalized fragment around the FM-QTA resonance of the colour plot presented in figure 5.7(a). The observed frequency splitting  $\Gamma \approx 0.4$  GHz. (b) Normalized fragment around the FM-QTA resonance of a colour plot consisting of reflection spectra. The black dots mark respective evaluated lines.

clearly seen. Hence, the observed phonon mode at 13.0 GHz cannot be responsible for the avoided crossing in the colour plot in figure 5.8(a). Another candidate is the QTA mode's antisymmetric counterpart QTA\*, which possesses almost the same frequency as the QTA mode, but is neither excitable nor detectable due to its antisymmetric  $\eta_{zz}$  distribution (see section 5.2). By taking a close look to the phonon frequencies out of resonance, slightly different frequencies are obtained for each phonon mode. The small frequency shift of roughly 0.1 GHz is a first hint at the contribution of different phonon modes for each colour plot.

In the following, the coupling strength between magnon and phonon modes is considered in detail. Since Verba et al, the magnon-phonon coupling strength is determined by the spatial overlap of the dynamical magnetization  $\delta\mathbf{m}$  of the magnon mode and dynamical strain components  $\eta_{ij}$  of the phonon mode [29]. In this respect, the interacting magnon and phonon modes can be considered as coupled oscillators [29]. Due to the in-plane applied magnetic field, the  $z$ -component of the steady state magnetization can be considered as zero (see equation 2.9). Hence, the magnon-phonon coupling can be modelled by considering only two dynamical strain components:  $\eta_{yy}$  and  $\eta_{yz}$  [15]. In this case, the magnon-phonon coupling strength in resonance is defined by two overlap integrals

$$K = \beta_1 \int \tilde{\eta}_{yy} \delta\tilde{m}_y dV + \beta_2 \int \tilde{\eta}_{yz} \delta\tilde{m}_z dV, \quad (5.5)$$

where  $\delta\tilde{m}_{y,z}$  and  $\tilde{\eta}_{yy,yz}$  are normalized projections of the dynamical magnetization and strain components, respectively<sup>12</sup>. The coefficients  $\beta_1$  and  $\beta_2$  are material specific and possess the dimension of frequency. The coefficients are defined by the saturation magnetization, the mass density, the external magnetic field orientation, the resonant frequency, as well as a combination of magneto-elastic constants  $b_i$ . The latter mixed contribution is due to a mixed polarization of Rayleigh-like phonon modes and can be estimated by numerical calculations using COMSOL. In the case of pure longitudinal and transverse waves, however,  $\beta_1$  and  $\beta_2$  are completely determined by respective magneto-elastic coefficients,  $b_1$  and  $b_2$ , and can be calculated analytically [32].

In order to evaluate the overlap integrals in equation 5.5, spatial distributions of respective phonon and magnon modes have to be calculated. A variety of calculated spatial strain distributions of the QTA and QTA\* mode were already introduced in section 5.2. Figure 5.9(a) only presents such strain components, which correspond to the overlap integrals in equation 5.5, i.e.  $\tilde{\eta}_{yy}$  and  $\tilde{\eta}_{yz}$ . Regarding the spatial distribution of the dynamical magnetization, the previous chapter on localized magnon modes

---

<sup>12</sup>The projections are normalized according to  $\int \delta\tilde{m}_{y,z}^2 dV = \int \tilde{\eta}_{yy,yz}^2 dV = 1$  ( $dV$  is a unit volume element).

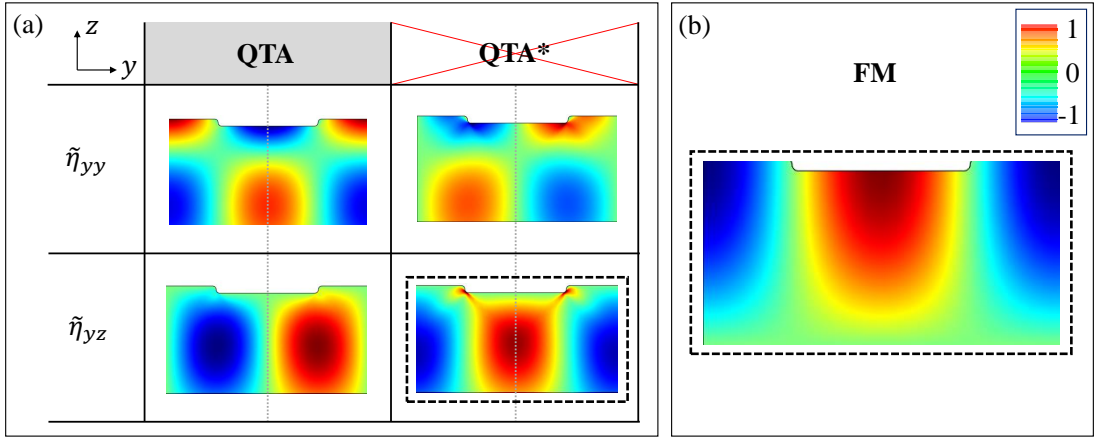


**Figure 5.9:** Spatial profiles of the (a) QTA, QTA\* and (b) FM mode

showed that fixed boundary conditions for the FeGa/Cr and the FeGa/GaAs interfaces well describe the experimental observation (see section 4.3). In the considered case of a physical NG, however, the Cr layer is being partly removed by the focused ion beam milling (FIB). Hence, an open surface is introduced. Therefore, mixed magnetic boundary conditions are assumed: fixed boundary conditions for the FeGa/GaAs interface and open boundary conditions for the patterned surface of the NG. Thus, the non-zero dynamical magnetization components for the FM mode can be written as

$$\delta m_y = \delta m_z = \delta m_0 \cos\left(\frac{2\pi}{p}y\right) \sin\left(\frac{\pi}{2h}z\right) \quad (5.6)$$

with amplitude  $\delta m_0$ , grating period  $p$  and layer thickness  $h$ . A visualization of the resulting normalized spatial distribution of  $\delta \mathbf{m}$  of the FM mode in equation 5.6 is shown in figure 5.9(b). Without any further calculations it is evident that the symmetric FM mode has a vanishing overlap with antisymmetric strain components, i.e.  $\tilde{\eta}_{yz}$  of the QTA mode and  $\tilde{\eta}_{yy}$  of the QTA\* mode. Calculations of the remaining overlap integrals with the FM mode show a value below  $10^{-3}$  for the symmetric  $\tilde{\eta}_{yy}$  component of the QTA mode, but a non-zero value for the symmetric  $\tilde{\eta}_{yz}$  component of the QTA\* mode. Hence, the coupling strength in equation 5.5 is solely given by the symmetric  $\tilde{\eta}_{yz}$  component of the QTA\* mode and reads  $K_{\text{QTA}^*} \approx 0.77\beta_2$ . With respect to the experimentally observed avoided crossing, the evaluated coupling constant reads  $K_{\text{QTA}^*} \approx \Gamma/2 = 0.2 \text{ GHz}$ . We conclude, that the avoided crossing in the experimentally observed colour plot in figure 5.7(a) is obtained due to the hybridization of the FM mode and the antisymmetric counterpart of the optically excited QTA mode, i.e. the non-excitable QTA\* mode. The non-excitability of the interacting QTA\* mode also explains the absence of phonon driving, which is observed for the higher FM-QLA resonance.

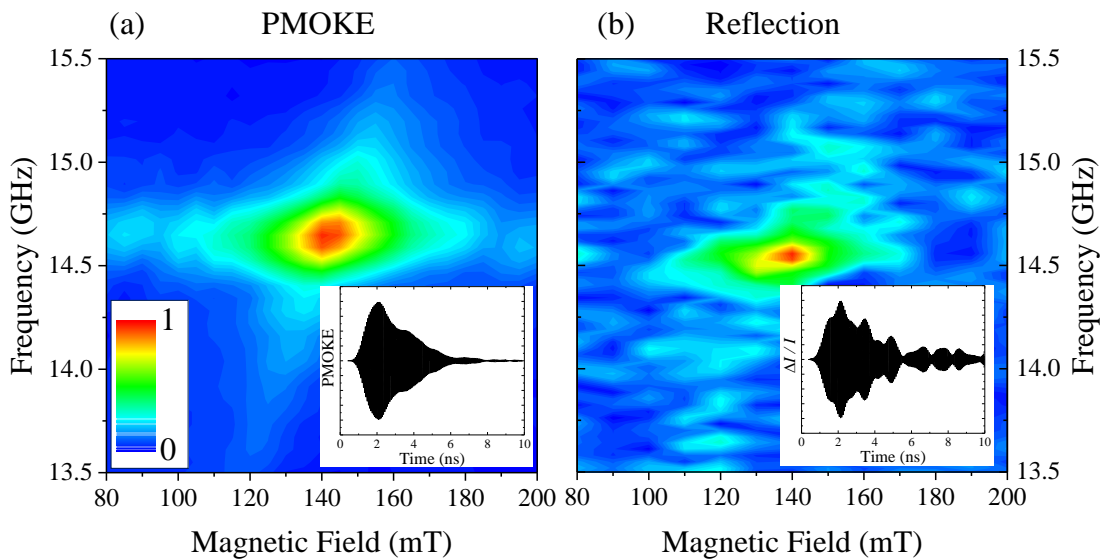


**Figure 5.10:** (a) Normalized fragment around the FM-QLA resonance of the colour plot presented in figure 5.7(a). (b) Normalized fragment around the FM-QLA resonance of a colour plot consisting of reflection spectra. The insets show respective transient signals at the FM-QLA resonance.

Figure 5.10(a) presents a fragment of the colour plot in figure 5.7(a), which shows a strong increase of the spectral amplitude for the FM-QLA resonance at  $B = 140$  mT, i.e. phonon driving. In order to check the influence of the phonon driving in the reflection signal, figure 5.10(b) shows a colour plot fragment consisting of reflection spectra. In contrast to the reflection spectra shown for the FM-QTA resonance, the FM-QLA resonance clearly contributes to the reflection signal. Such contribution to the reflection signal at resonance is still under debate, however, a detailed discussion is beyond the scope of this work. Nevertheless, two possible explanations are discussed shortly: On the one hand, the increase can be attributed to the FM-QLA interaction, which affects the polarization of the phonon mode similarly to the case of bulk [112] and surface acoustic waves [113]. As already discussed in section 5.3.1, the QLA mode is not visible in reflection due to its specific polarization and material specific photo-elastic constants. However, by altering the in-plane shear component  $\eta_{yx}$  the QLA mode contributes to the reflection signal. Hence, an increase of the QLA mode's spectral amplitude in the reflection signal is observed at resonance with the FM mode. On the other hand, the PMOKE signal can contribute to the reflection signal due to the quadratic MOKE (QMOKE) [50] (see section 2.1.2). In this case, the introduction of a physical NG alters the boundary conditions of the sample surface resulting in a contribution of the magnetization precession to the reflection signal. Insets of figure

5.10 show transient PMOKE and reflection signals at the FM-QLA resonance<sup>13</sup>. Both transient signals show a very similar behaviour, which is characterized by an increase up to 1 ns followed by a slow decrease. Hence, a contribution of the magnetization precession to the photo-elastic effect cannot be excluded.

In order to determine the coupling strength of the FM mode and the optically excited QLA mode, equation 5.5 is evaluated for respective spatial magnetization and strain distributions. Figure 5.11(a) presents normalized strain distributions of the QLA and QLA\* mode, respectively. 5.11(b) again presents the assumed dynamical magnetization distribution of the FM mode. Due to the symmetric FM mode all spatial overlap

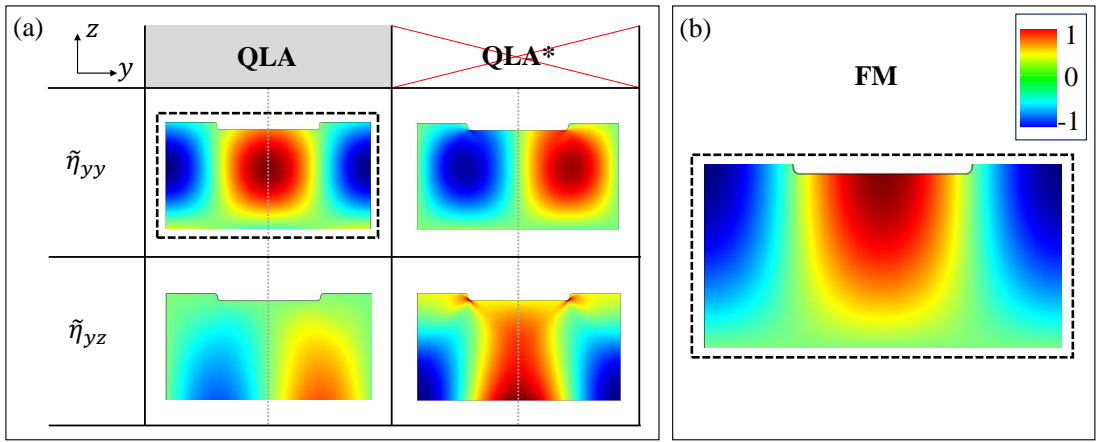


**Figure 5.11:** Spatial profiles of the (a) QLA, QLA\* and (b) FM mode.

integrals with antisymmetric strain distributions are vanishing. A numerical calculation of all overlap integrals yield only one non-zero overlap integral of the FM mode, i.e. the  $\tilde{\eta}_{yy}$  component of the QLA mode. The corresponding coupling strength reads  $K_{\text{QLA}} \approx \beta_1$ . Hence, the non-zero spatial overlap is given by the optically excited QLA mode, which efficiently drives the magnetization precession. This is in accordance with the experimental observation of a strong increase of the PMOKE amplitude in the FM-QLA resonance. The absence of the avoided crossing for the FM-QLA resonance can be related to a small value of  $K_{\text{QLA}}$  and a corresponding moderate magneto-elastic coupling. The coupling strength<sup>14</sup>

$$K_{\text{QLA}} = \frac{1}{2} \sqrt{(\Delta f_{\text{R}} - \Delta f_{\text{QLA}})(\Delta f_{\text{FM}} - \Delta f_{\text{R}})} \approx 0.07 \text{ GHz} \quad (5.7)$$

<sup>13</sup>The reflection signal in the inset in figure 5.10(b) is filtered using a high pass filter  $> 13.5$  GHz in order to avoid a contribution by the 13 GHz QTA mode. The filtering affects the very first hundreds of ps and slightly modulates the amplitude, but does not change the overall behaviour of the reflection signal.

<sup>14</sup>The derivation of the used formula can be found in section A.5.

relates to the linewidth of the interacting modes in and out of resonance [114]. The linewidths out of resonance are known and read  $\Delta f_{\text{QLA}} = 0.06$  GHz and  $\Delta f_{\text{FM}} = 0.34$  GHz, respectively. The linewidth in resonance can be evaluated using figure 5.7(d) on page 78, which yields  $\Delta f_{\text{R}} = 0.2$  GHz. The evaluated coupling strength yields a cooperativity  $C_{\text{QLA}} \approx 1$ , which confirms the case of moderate coupling. Therefore, the magnon polaron formation is still happening [18], but the avoided crossing is masked by the energy transfer from the strongly excited phonon mode to the magnon mode. A more detailed and quantitative explanation concerning the *masking effect* is given a bit later.

In the above discussion, specific magnon and phonon modes were pointed out, which are responsible for different manifestations of the magnon-phonon coupling. As already mentioned, the magnon-phonon coupling between certain magnon and phonon modes can be described by a system of coupled oscillators according to (see equation 2.69)

$$\frac{1}{2\pi} \frac{da_j}{dt} - if_j a_j + \frac{\Delta f_j}{2} a_j + i \sum_l K_{jl} a_l = A_j, \quad (5.8)$$

where  $a_j$  are complex amplitudes,  $\Delta f_j$  are spectral linewidths,  $A_j$  are excitation amplitudes and  $j = \text{QTA}^*, \text{QLA}, \text{FM}$ . The specific magnon-phonon coupling of the considered magnon and phonon modes is described by a symmetric coupling tensor

$$\hat{K} = \begin{pmatrix} 0 & 0 & K_{\text{QTA}^*} \\ 0 & 0 & K_{\text{QLA}} \\ K_{\text{QTA}^*} & K_{\text{QLA}} & 0 \end{pmatrix}. \quad (5.9)$$

For the sake of completeness, figure 5.12(a) shows once again the experimentally observed PMOKE colour plot with two characteristic magnon-phonon resonances. The presented colour plot is solely given by the spectral amplitude of the magnetization precession of the FM mode  $|\tilde{a}_{\text{FM}}|$ . Therefore, the calculated colour plot in figure 5.12(b) only presents FFTs of  $a_{\text{FM}}$ , i.e.  $|\tilde{a}_{\text{FM}}|$ , where all used parameters for equation 2.68 are listed in table 5.1. The excitation amplitudes  $A_j$  are chosen in a way that the non-excitable QTA\* mode has a vanishing excitation amplitude, i.e.  $A_{\text{QTA}^*} = 0$ , and that the strongly excited QLA mode has a much larger excitation amplitude than the FM mode, i.e.  $A_{\text{QLA}} = 10 \gg A_{\text{FM}} = 1$ . The calculated colour plot is in good accordance

Mode	$f$ (GHz)	$\Delta f$ (GHz)	$K$ (GHz)	$A$
FM	$7.12 + 0.05 / \text{mT} \cdot B$ [mT]	0.34	-	1
QTA*	13.0	0.06	0.2	0
QLA	14.6	0.06	0.07	10

**Table 5.1:** This table shows the used parameters for the calculated colour plot in figure 5.12(b).



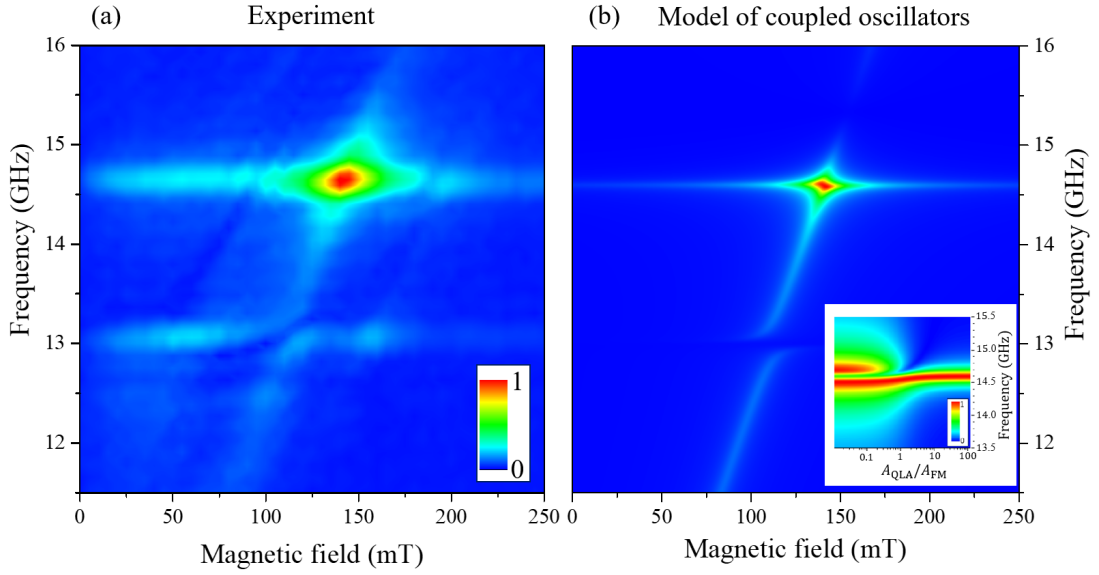


**Figure 5.12:** (a) Experimentally evaluated colour plot of PMOKE spectra for backside excitation (similar to figure 5.7(a)). (b) Calculated colour plot for the discussed system of coupled oscillators. The used equation and parameters can be found in 5.8 and 5.1, respectively. The inset demonstrates the *masking effect* of a given avoided crossing due to a large difference in the excitation amplitudes  $A_i$ .

with the experimentally observed avoided crossing for the FM-QTA\* resonance and the phonon driving for the FM-QLA resonance. Hence, the model of coupled oscillators, where the magnon-phonon coupling strength is determined by respective spatial overlap integrals, sufficiently describes the selective magnon-phonon coupling observed in ferromagnetic NGs.

The origin of the masking effect in PMOKE (and reflection) is shown in the inset of the calculated colour plot in figure 5.12(b), where normalized FFTs of  $a_{\text{FM}}$  for different relations of  $A_{\text{QLA}}$  and  $A_{\text{FM}}$ , i.e.  $A_{\text{QLA}}/A_{\text{FM}}$ , are presented. This colour plot indicates the presence of two regimes: For  $A_{\text{QLA}}/A_{\text{FM}} < 1$  the frequency splitting is clearly visible, while for  $A_{\text{QLA}}/A_{\text{FM}} \geq 1$  only one line contributes to  $|\tilde{a}_{\text{FM}}|$ . The latter regime characterizes the FM-QLA resonance. It is important to emphasize that the shown spectra are normalized, because spectral amplitudes for the case of  $A_{\text{QLA}}/A_{\text{FM}} \geq 1$  are much larger than for the case of  $A_{\text{QLA}}/A_{\text{FM}} < 1$ .

In order to show the impact of the excitation amplitudes on the manifestations of occurring magnon-phonon resonances, figure 5.13 shows a variety of calculated colour plots for different sets of excitation amplitudes  $A_i$ . While the excitation amplitudes are changing, all other parameters remain the same. Figure 5.13(a) shows the case, where only the FM mode is excited ( $A_{\text{FM}} = 1$ ), but not the phonon modes ( $A_{\text{QTA}^*, \text{QLA}} = 0$ ).

In this case, no phonon driving occurs, but both magnon-phonon resonances show avoided crossings with different frequency splittings. In figure 5.13(b) both phonon modes are much larger excited ( $A_{QTA^*,QLA} = 10$ ) than the FM mode ( $A_{FM} = 1$ ). Here, both resonances show phonon driving. While the FM-QLA resonance is masked by the moderate coupling, the FM-QTA\* resonance still shows an avoided crossing due to the strong coupling regime. Figure 5.13(c) presents the case, where the lower mode is strongly excited ( $A_{QTA^*} = 10$ ), but not the upper one ( $A_{QLA} = 0$ ). In this scenario both resonances show some driving behaviour, where the upper resonance possesses an asymmetric shape indicating a so-called Fano resonance [115]. The last colour plot in figure 5.13(d) shows the opposite case of the previous figure 5.13(c), i.e. strongly excited QLA mode ( $A_{QLA} = 10$ ), but no excitation of the QTA\* mode ( $A_{QTA^*} = 0$ ). As already discussed, this set of excitation amplitudes well describes the experimentally observed colour plot in figure 5.12(a).

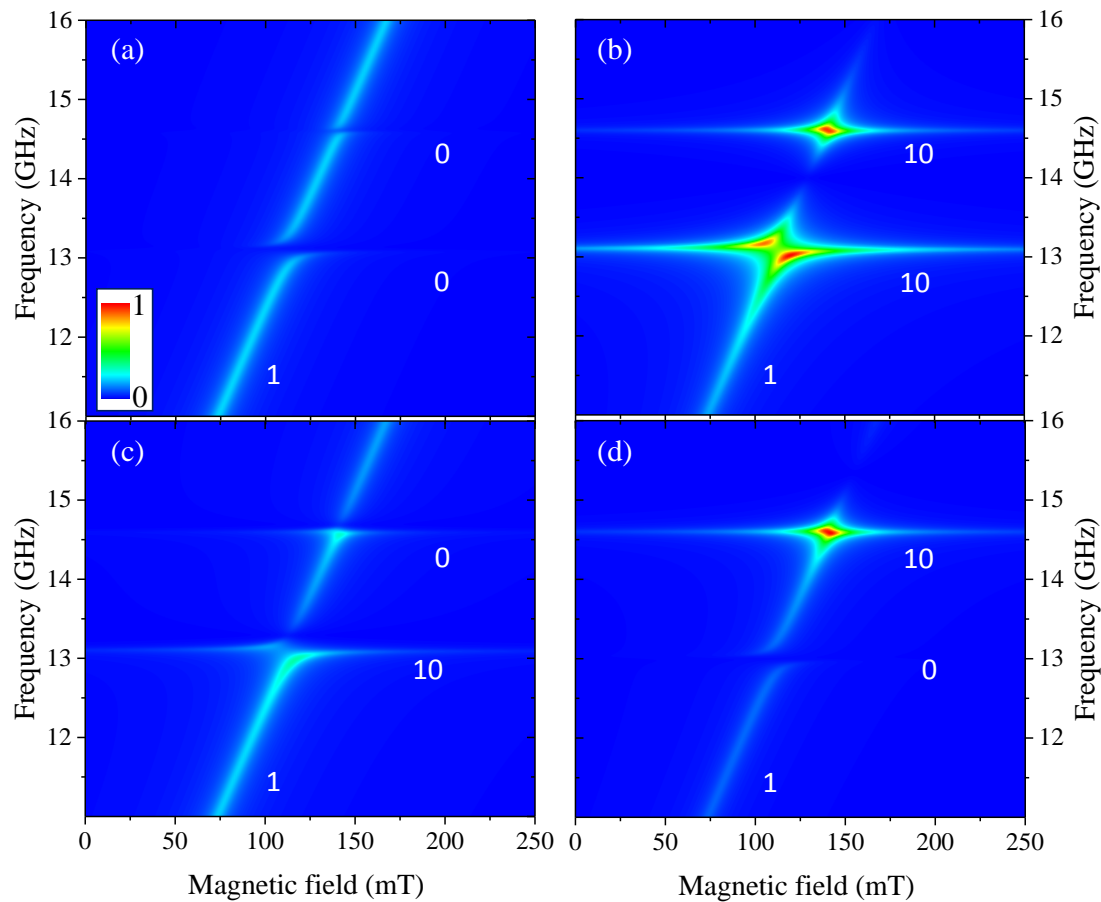


**Figure 5.13:** Summary of calculated colour plots having different sets of excitation amplitudes (as indicated in each plot). All other parameters are constant and listed in table 5.1. (a)  $A_{FM} = 1$ ,  $A_{QTA^*} = 0$ ,  $A_{QLA} = 0$ . (b)  $A_{FM} = 1$ ,  $A_{QTA^*} = 10$ ,  $A_{QLA} = 10$ . (c)  $A_{FM} = 1$ ,  $A_{QTA^*} = 10$ ,  $A_{QLA} = 0$ . (d)  $A_{FM} = 1$ ,  $A_{QTA^*} = 0$ ,  $A_{QLA} = 10$ .

To conclude, the performed analysis of both magnon-phonon resonances shows that optically excited magnon polarons are formed via the selective interaction of specific localized magnon and phonon modes. As a tool, the model of coupled harmonic oscillators is sufficient to describe the different manifestations of magnon-phonon resonances. In this case, the magnon-phonon coupling strength is determined by a spatial overlap integral of calculated magnon and phonon modes. This approach avoids the *ab initio* consideration of respective equations of motion; as it is done in [32]. Moreover, COMSOL calculations provide the ability to identify optically excitable modes, which is important for pump-and-probe experiments on ferromagnetic metals.

## 5.4 Angular Dependence of Localized Magnon Modes

The focus in the previous section was on the FM-QTA and FM-QLA resonances. In this respect, only the FM mode was discussed in detail, however, additional high-order magnon modes are present in the 105 nm Galfenol nanolayer. Such multi-mode magnetization precession in an **un**patterned 105 nm Galfenol nanolayer was carefully discussed in section 4.3. Therefore, additional magnon-phonon resonances are also expected in a patterned Galfenol nanolayer. Due to mixed magnetic boundary conditions of the patterned nanolayer<sup>15</sup>, allowed wave vectors in  $z$ -direction read

$$k_n^z = \frac{n\pi}{2d}. \quad (5.10)$$

While mode numbers with  $n = 0$  and  $n = 1$  correspond to the uniform and FM mode, respectively, high-order magnon modes are characterized by  $n > 1$ . Figure 5.14(a) presents schematic spatial profiles of the certain localized magnon modes.

Besides a change of respective wave vectors, the introduced NG also affects the free energy density of the ferromagnet. Therefore, a phenomenological anisotropy can be defined, which describes the influence of the NG on the magnetization direction and precession frequency. Due to the introduction of parallel grooves into the ferromagnet, the equilibrium direction of the static magnetization near the surface is forced to be parallel to the grooves. The parallel alignment of the static equilibrium magnetization is a result of a minimization of the demagnetization field, which is introduced by the NG (see equation 2.5). Hence, the [100]-crystallographic direction parallel to the grooves determines the easy magnetization axis of the NG, i.e.  $x$ -direction. By slightly rotating the static magnetization away from the [100]-crystallographic direction, a non-zero demagnetizing field is being introduced. The maximum demagnetizing field is reached for a magnetization perpendicular to the grooves, i.e. along the  $y$ -direction. Therefore, the

---

<sup>15</sup>Fixed boundary conditions for the FeGa/GaAs interface and open boundary conditions for the patterned surface of the NG.

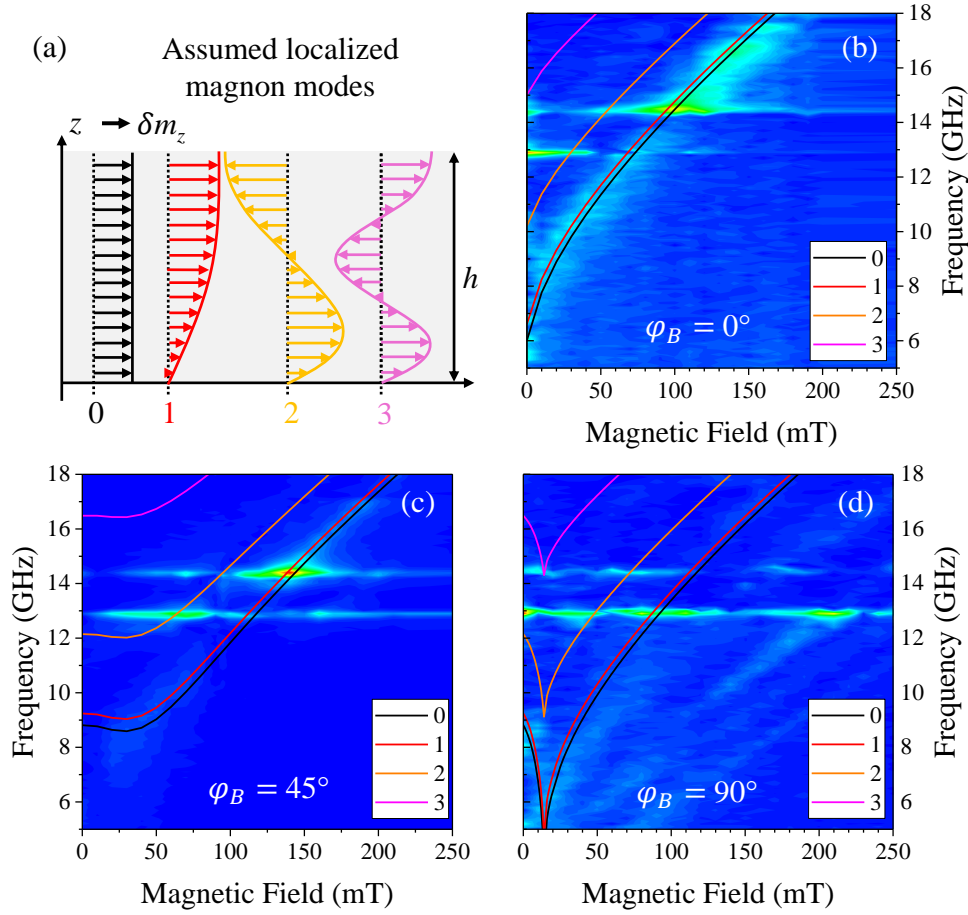


**Figure 5.14:** (a) Localized magnon modes in a patterned Galfenol nanolayer. Corresponding calculated precession frequencies are presented in figures (b) - (d) using equation 5.13. (b) PMOKE colour plot for  $\varphi_B = 0^\circ$ . The magnetic field step size is 10 mT, but not from 200 to 250 mT, where a step size of 50 mT is used. (c) PMOKE colour plot for  $\varphi_B = 45^\circ$  with a step size of 5 mT. (d) PMOKE colour plot for  $\varphi_B = 90^\circ$  with a step size of 5 mT.

$y$ -direction denotes the hard magnetization axis of the NG. Finally, the contribution of the NG to the free energy density can be phenomenologically written as

$$F^{\text{NG}} = -K_{\text{NG}}m_x^2, \quad (5.11)$$

where  $K_{\text{NG}}$  is an anisotropy coefficient describing the demagnetizing field introduced by the NG. Hence, the free energy density of an unpatterned nanolayer in equation 4.8 can be extended to

$$\begin{aligned} F^{\text{layer,NG}} = & -\mathbf{m}\mathbf{B} + K_1 (m_x^2m_y^2 + m_x^2m_z^2 + m_y^2m_z^2) \\ & - K_u (m_x + m_y)^2 - K_{\text{NG}}m_x^2 + B_d m_z^2. \end{aligned} \quad (5.12)$$

Resulting precession frequencies of the patterned Galfenol nanolayer are given by equation 4.2 and read

$$f_n = \gamma_e \sqrt{F_{\varphi\varphi}^{\text{layer,NG}} \cdot F_{\theta\theta}^{\text{layer,NG}} + \left( F_{\varphi\varphi}^{\text{layer,NG}} + F_{\theta\theta}^{\text{layer,NG}} \right) \cdot Dk_n^2}. \quad (5.13)$$

Figure 5.14 presents three normalized colour plots containing evaluated PMOKE spectra for three different azimuthal angles of  $\varphi_B = 0^\circ$ ,  $45^\circ$  and  $90^\circ$ . In this case, the excitation geometry is frontside excitation and the power densities of the pump and probe pulses are similar to the previous section. All colour plots provide the same magnetic field range between 0 and 250 mT. The colour plot for  $\varphi_B = 0^\circ$  in figure 5.14(b) is characterized by two horizontal lines, which are identified as the QTA and QLA modes. The broad magnetic field dependent line corresponds to the magnetiza-

Layer (nm)	$K_1$ (mT)	$K_u$ (mT)	$\mu_0 M_s$ (T)	$D$ (mT/nm <sup>2</sup> )	$K_{\text{NG}}$ (mT)
105	18	5	1.8	23	10

**Table 5.2:** Used parameters for the calculated curves in figure 5.14.

tion precession and is identified as the FM mode of the Galfenol nanolayer. Besides the FM-QTA and FM-QLA resonances, additional resonances appear for frequencies higher than the FM mode. By using the FED approach in equation 5.13 and the parameters in table 5.2, the FM mode and additional localized magnon modes can be calculated (coloured lines). It is clearly seen that the broad visible magnon mode is identified as the FM mode within the FED approach<sup>16</sup>. In addition, high-order magnon modes are presented, which can be responsible for other magnon-phonon resonances. These magnon-phonon resonances can be treated similarly to the approach discussed in the previous section, but the careful analysis of all magnon-phonon resonances is far beyond the scope of this work. The aim of this section is to show the influence of the azimuthal angle on the localized magnon modes and a way to control the selective interaction of magnon and phonon modes. For the used azimuthal angle of  $\varphi_B = 0^\circ$ , the magnetic field orientation is parallel to the grooves and, thus, the NG has no influence ( $K_{\text{NG}} = 0$ ). This changes for the intermediate orientation of  $\varphi_B = 45^\circ$ .

Figure 5.14(c) presents a colour plot for an intermediate orientation, i.e.  $\varphi_B = 45^\circ$ . As expected, the magnetic field independent phonon modes remain unchanged with respect to the previous orientation. The magnetic field dependence of the localized magnon modes is changed due to the influence of the anisotropy contributions to the free energy density, i.e. cubic anisotropy, uniaxial anisotropy and the NG anisotropy. The anisotropy coefficient of the NG anisotropy is estimated to be  $K_{\text{NG}} = 10$  mT, which indicates a small contribution to the free energy density. As before, the bright

<sup>16</sup>The FM mode is degenerated with the uniform mode, whereas no clear separation is possible.

magnon-phonon resonances are due to the interaction with localized magnons in the nanolayer. However, other resonances occur additionally to the already identified ones; especially, below the FM mode at magnetic fields of roughly  $B = 160$  and  $200$  mT. Hence, additional magnon modes are assumed to be present in the studied NG.

Figure 5.14(c) presents a colour plot for a perpendicular orientation, i.e.  $\varphi_B = 90^\circ$ . In this case, a lot of additional magnon modes appear in the PMOKE spectra. It is clearly seen that for this orientation the used FED approach is unable to characterize the observed rich PMOKE spectra. The reason lies in the formation specific magnon modes, which are determined by the NG shape and, therefore, additionally quantized in the  $y$ -direction [9], [110]. Hence, the assumed homogeneous magnon distributions shown in figure 5.14 are not valid anymore due to the introduced shape of the nanolayer. Therefore, micromagnetic simulations are needed in order to calculate shape specific dispersion relations of localized magnon modes. COMSOL calculations show that the spatial profile of localized magnon modes is drastically changed for different azimuthal angles  $\varphi_B$  [110], which enables the way to address localized phonon modes by specific magnon modes by altering their spatial distributions for different  $\varphi_B$ .

Another important characteristic in figures 5.14 (b), (c) and (d) is the value of the evaluated PMOKE amplitude. While the colour plot for  $\varphi_B = 45^\circ$  possesses a nice smooth blue background indicating large PMOKE amplitudes, which are far above the noise level, the other plots for  $\varphi_B = 0^\circ$  and  $90^\circ$  are characterized by small PMOKE amplitudes near the noise level. This observation of small PMOKE amplitudes for  $\varphi_B = 0^\circ$  and  $90^\circ$  is in accordance with numerical calculations using COMSOL [110].

To conclude, the patterned Galfenol nanolayer contains a rich spectrum of localized magnon modes, which is determined by the NG shape and the azimuthal angle  $\varphi_B$ . Experimentally observed PMOKE spectra show that the FED approach sufficiently describes the observed magnon spectrum for  $\varphi_B \leq 45^\circ$ . For such magnetic field orientations the influence of the NG shape on the magnetization can be considered as small. In contrast to that,  $\varphi_B$  close to  $90^\circ$  strongly alter the magnon spectrum, where micromagnetic simulations are needed.

## Chapter 6

# Conclusion and Outlook

The work at hand presents the experimental observation of magnon polarons in a shallow ferromagnetic nanograting (NG) via the selective interaction of specific localized magnon and phonon modes (see chapter 5). To the best of our knowledge, the transient observation of a magnon polaron in a ferromagnetic metal has not been reported yet.

In contrast to the common FMR technique, this work utilizes the polar magneto-optical Kerr effect (PMOKE), which serves to detect the coherent magnetization dynamics in the ferromagnetic metal. In this respect, a unique two-colour pump and probe setup is being built, where the asynchronous optical sampling (ASOPS) technique is used to trace the transient evolution of the PMOKE (see chapter 3). The whole experimental setup is remotely controllable using special software developed in MATLAB (see section A.2). The utilized pump and probe setup is all-optical and provides two different excitation geometries: on the one hand, the pump and probe pulses incident on the same side of the sample (frontside excitation) and on the other hand, the pump and probe pulses incident on opposite sides of the sample (backside excitation). Both excitation geometries provide characteristic transient reflection signals (see section 3.3.3). For frontside excitation the absorbed pump pulse introduces a huge temperature gradient, which is traced by the probe pulse. In this case, the detected area is strongly influenced by the introduced heat of the pump pulse. The geometry of backside excitation, however, avoids a contribution of the direct impact of the pump pulse on the detection. Depending on the interest, the geometry of backside excitation may be preferred; however, the overall results are similar for both excitation geometries.

Before the consideration of magnon-phonon resonances in a ferromagnetic NG, unpatterned Gallenol nanolayers with different layer thicknesses are investigated in detail in chapter 4. Due to the spatial confinement of intermediate nanolayers, a number of discrete localized magnon modes are optically excited and detected. The observed magnon modes are analysed within the free energy density (FED) approach, where each

mode is identified with a specific mode number. Moreover, the amplitude and lifetime of each magnon mode decrease with an increasing mode number. These observations are explained by either a selective excitation efficiency of each mode and a damping mechanism, which linearly depends on the precession frequency, i.e. spin-orbit coupling, eddy currents or two-magnon scattering. Due to the frequency dependent damping, the lowest magnon mode provides the longest lifetime of roughly 1 ns.

In order to isolate the lowest mode from other localized modes, the layer thickness is reduced to several nm. In this case, the introduced thermal distribution by the pump pulse can be considered as homogeneous, which prohibits the excitation of modes with sign-changing profiles. Hence, ultrathin Galfenol nanolayers are characterized by a single-mode magnetization precession (see section 4.4). The observed single-mode magnetization precession is analysed within the FED approach, which clearly indicates the cubic and uniaxial anisotropy of a Galfenol nanolayer. In addition, the azimuthal dependence of the mode's linewidth gives a hint at the contribution of two-magnon scattering, which was recently observed in a Galfenol nanolayer on a MgO substrate [89]. The well-observed magnetization precession of roughly 100 GHz at a magnetic field strength of  $B = 3$  T reveals Galfenol as a promising candidate for the study of long-living and high frequency magnetization precession. Especially, the evaluation of the magnetic field dependent linewidth indicates a purely intrinsic damping mechanism by the spin-orbit coupling. It is expected that the detection of precession frequencies reaching the THz range (300 GHz) is possible in Galfenol nanolayers.

The characterization of two magnon-phonon resonances in a shallow ferromagnetic nanograting (NG) is presented in chapter 5. In this case, the so-called fundamental magnon (FM) mode of the patterned 105 nm Galfenol nanolayer is of primary interest. By changing the magnetic field strength, the changing FM mode's precession frequency finds two resonance conditions with two Rayleigh-like surface acoustic waves, i.e. a quasi-transversal acoustic (QTA) mode at 13 GHz and a quasi-longitudinal acoustic (QLA) mode at 14.6 GHz. In addition, both phonon modes possess non-excitable anti-symmetric counterparts with similar frequencies and lifetimes, i.e. QTA\* and QLA\*.

The occurring magnon-phonon resonances have different manifestations: While the lower FM-QTA resonance provides an avoided crossing, the higher FM-QLA resonance shows efficient phonon driving. The experimental observation of an avoided crossing and a corresponding high cooperativity of  $C \approx 8$  is a clear evidence for the formation of a magnon polaron in a ferromagnetic nanograting. In order to understand the different manifestations of magneto-elastic coupling, spatial overlap integrals of the dynamical magnetization of the FM mode and several strain distributions of the phonon modes are calculated. Since Verba et al [29], such spatial overlap integrals determine the coupling



---

strength between respective modes. In this case, the absence of the phonon driving for the lower FM-QTA resonance is explained by a non-zero spatial overlap integral with the QTA's antisymmetric counterpart, i.e. QTA\*. Due to vanishing spatial overlap integrals of the FM mode with all strain components of the QTA mode, the QTA cannot be responsible for the avoided crossing. The only non-zero spatial overlap integral and, therefore, a non-zero coupling strength is calculated for the antisymmetric counterpart QTA\*. Due to the antisymmetric spatial profile, the QTA\* mode cannot be optically excited nor detected. The non-excitability of the QTA\* mode also explains the absence of phonon driving, which is observed for the higher FM-QLA resonance. In case of the FM-QLA resonance, the only non-zero coupling strength is calculated for the optically excited QLA mode, which yields to efficient phonon driving. Due to the moderate coupling regime with a cooperativity of  $C \approx 1$ , the avoided crossing is masked by the energy transfer from phonons to magnons. Finally, the model of coupled oscillators, where the coupling strength is determined by respective overlap integrals, qualitatively explains the different manifestations of both observed magnon-phonon resonances. Hence, the approach by Verba et al. can be used to calculate the coupling strength of certain magnon and phonon modes with specific spatial profiles. Thus, this approach is very helpful in the investigation of selectively coupled magnon and phonon modes. This approach avoids the ab initio consideration of respective equations of motion. In addition, COMSOL calculations provide the ability to identify optically excitable modes, which is important for pump-and-probe experiments on ferromagnetic metals.

One possibility to alter the spatial profile of localized magnon modes is determined by the magnetic field orientation with respect to the NG grooves [110] (see section 5.4). The magnetic field orientation has a significant impact on the spatial profile of the magnon modes and, therefore, on the magnon-phonon coupling strength. Hence, for further experiments the magnetic field orientation can be utilized to control the selective interaction of localized magnon modes with phonon modes.

Besides localized spin waves within a certain structure, nano-sized structures can be used to excite propagating short-wavelength spin waves in ferromagnetic layer of YIG [116] and Galfenol [117]. The phenomenon of sending, manipulating and receiving of propagating spin and acoustic waves is well studied, both theoretically and experimentally. For example, there are lenses [118], [119], filters [120] and amplifiers [121] for propagating spin-waves. By using selectively coupled magnon polarons it could be possible to enhance or arbitrarily manipulate such propagating waves.



# List of Figures

2.1	Magnetization curves for Iron . . . . .	7
2.2	Isosurface of the cubic anisotropy for $K_1 > 0$ . . . . .	8
2.3	Excitation process of the magnetization precession . . . . .	9
2.4	Magnetization precession and spin waves . . . . .	10
2.5	Methods for the detection of certain magnetization components via the magneto-optical Kerr effect. . . . .	12
2.6	Illustration of strain and stress . . . . .	15
2.7	Ultrafast optically excitation . . . . .	16
2.8	Polarization of elastic waves . . . . .	18
2.9	Detection of strain by means of an reflected probe pulse . . . . .	18
2.10	Illustration of magnetostriction . . . . .	21
2.11	Formation of magneto-elastic waves . . . . .	23
2.12	Single and coupled harmonic oscillators . . . . .	25
2.13	Coupled oscillators and avoided crossing . . . . .	26
2.14	Two regimes of coupled oscillators . . . . .	28
3.1	Magnetostrictive constants for different Gallium concentrations . . . . .	32
3.2	Illustration of a conventional pump and probe setup using a mechanical delay line . . . . .	34
3.3	Illustration of the ASOPS technique . . . . .	34
3.4	Schematic of the pump and probe setup . . . . .	37
3.5	Images of the sample's surface including the pump and probe spots taken by the webcam . . . . .	39
3.6	Experiment to estimate the optical absorption depth in Galfenol . . . . .	42
3.7	Comparison of the transient change in reflection for different excitation geometries . . . . .	43
3.8	Pump power dependence of transient reflection signals . . . . .	45
4.1	Galfenol nanolayers with different layer thicknesses . . . . .	48
4.2	Localized magnon modes in a ferromagnetic nanolayer with fixed bound- ary conditions . . . . .	49

4.3	Magnetic field dependence PMOKE signals performed on a 105 nm Galfenol layer at $B = 200$ mT . . . . .	52
4.4	Angular dependencies of the precession frequencies of a 105 nm-thick Galfenol layer . . . . .	53
4.5	Tail analysis of a TR-PMOKE measurement performed on a 105 nm Galfenol layer at $B = 200$ mT . . . . .	55
4.6	Comparison of normalized PMOKE signals and their power spectra for different Galfenol layers . . . . .	56
4.7	Magnetic field dependence of measured precession frequencies of a 4, 5, 20, 60 and 105 nm Galfenol layer . . . . .	58
4.8	Selective excitation of high-order magnon modes in metallic nanolayers .	60
4.9	Magnetic field and angular dependencies of the uniform mode's precession frequency of a 4 nm-thin Galfenol layer . . . . .	61
4.10	Magnetic field and angular dependencies of the precession amplitude of a 4 nm-thin Galfenol layer . . . . .	62
4.11	Magnetic field dependencies of $\Delta f_{\text{eff}}$ in a 4 nm-thin Galfenol layer . . . .	64
4.12	Transient PMOKE signal and its power spectrum for a 4 nm-thin Galfenol layer at $B = 3$ T and $\varphi_B = -22^\circ$ . . . . .	66
4.13	Transient reflection signal and power spectrum of a 4 nm Galfenol layer at $B = 0$ T . . . . .	67
5.1	Schematics of the used Galfenol nanolayer with an introduced NG . . . .	70
5.2	Calculated deformed mesh illustrating the atom displacement of localized acoustic modes in a nanograting . . . . .	72
5.3	Symmetric and antisymmetric modes in a nanograting . . . . .	73
5.4	Spatial distributions of non-zero dynamical strain components of localized acoustic modes in the NG . . . . .	73
5.5	Principle of magnon-phonon resonance experiments . . . . .	75
5.6	Evaluation of a transient reflection signal of a 7 nm deep NG, where $\varphi_B = 0$ and $B = 250$ mT . . . . .	76
5.7	Colour plot of PMOKE spectra for backside excitation . . . . .	78
5.8	Comparison of colour plots of PMOKE and reflection spectra . . . . .	79
5.9	Spatial profiles of the QTA, QTA* and FM mode . . . . .	81
5.10	Comparison of colour plots of PMOKE and reflection spectra . . . . .	82
5.11	Spatial profiles of the QLA, QLA* and FM mode . . . . .	83
5.12	Comparison of an experimentally observed colour plot with a calculated colour plot . . . . .	85
5.13	Summary of calculated colour plots having different sets of excitation amplitudes . . . . .	86
5.14	Azimuthal dependence PMOKE color plots . . . . .	88

A.1 Estimated size of pump spots for different excitation geometries . . . . . 112

A.2 Software for remote control . . . . . 113

A.3 Software for remote control . . . . . 115

A.4 Three signals with different amplitude and lifetime . . . . . 117

A.5 Presentation of transient PMOKE measurements in a NG with additional regression and their corresponding FFT spectra at certain magnetic fields . . . . . 119

A.6 Probe polarization dependence of reflection spectra in an NG . . . . . 121



# Bibliography

- [1] Gallagher, W. J. and Parkin, S. S. P. *IBM Journal of Research and Development* **50**(1), 5–23 (2006).
- [2] Zhu, J.-G., Zhu, X., and Tang, Y. *IEEE Transactions on Magnetics* **44**(1), 125–131 (2008).
- [3] Kawahara, T., Ito, K., Takemura, R., and Ohno, H. *Microelectronics Reliability* **52**(4), 613–627 (2012).
- [4] Degen, C. L., Poggio, M., Mamin, H. J., Rettner, C. T., and Rugar, D. *Proceedings of the National Academy of Sciences* **106**(5), 1313–1317 (2009).
- [5] Dehoux, T., Ghanem, M. A., Zouani, O. F., Rampnoux, J.-M., Guillet, Y., Dilhaire, S., Durrieu, M.-C., and Audoin, B. *Scientific Reports* **5**(1) (2015).
- [6] Chen, T., Dumas, R. K., Eklund, A., Muduli, P. K., Houshang, A., Awad, A. A., Durrenfeld, P., Malm, B. G., Rusu, A., and Akerman, J. *Proceedings of the IEEE* **104**(10), 1919–1945 (2016).
- [7] Sato, K. *Spintronics for next generation innovative devices*. John Wiley & Sons Inc, Chichester, West Sussex, United Kingdom, (2015).
- [8] Kittel, C. *Physical Review* **110**(6), 1295–1297 (1958).
- [9] Langer, M., Gallardo, R. A., Schneider, T., Stienen, S., Roldán-Molina, A., Yuan, Y., Lenz, K., Lindner, J., Landeros, P., and Fassbender, J. *Physical Review B* **99**(2) (2019).
- [10] Hiebert, W. K., Stankiewicz, A., and Freeman, M. R. *Physical Review Letters* **79**(6), 1134–1137 (1997).
- [11] Borgnis, F. E. and Papas, C. H. In *Elektrische Felder und Wellen / Electric Fields and Waves*, 285–422. Springer Berlin Heidelberg (1958).
- [12] van Kampen, M., Jozsa, C., Kohlhepp, J. T., LeClair, P., Lagae, L., de Jonge, W. J. M., and Koopmans, B. *Physical Review Letters* **88**(22) (2002).

- [13] Scherbakov, A. V., Salasyuk, A. S., Akimov, A. V., Liu, X., Bombeck, M., Brüggemann, C., Yakovlev, D. R., Sapega, V. F., Furdyna, J. K., and Bayer, M. *Physical Review Letters* **105**(11) (2010).
- [14] Jäger, J. V., Scherbakov, A. V., Glavin, B. A., Salasyuk, A. S., Campion, R. P., Rushforth, A. W., Yakovlev, D. R., Akimov, A. V., and Bayer, M. *Physical Review B* **92**(2) (2015).
- [15] Salasyuk, A. S., Rudkovskaya, A. V., Danilov, A. P., Glavin, B. A., Kukhtaruk, S. M., Wang, M., Rushforth, A. W., Nekludova, P. A., Sokolov, S. V., Elistratov, A. A., Yakovlev, D. R., Bayer, M., Akimov, A. V., and Scherbakov, A. V. *Physical Review B* **97**(6) (2018).
- [16] Godejohann, F., Scherbakov, A. V., Kukhtaruk, S. M., Poddubny, A. N., Yaremkevich, D. D., Wang, M., Nadzeyka, A., Yakovlev, D. R., Rushforth, A. W., Akimov, A. V., and Bayer, M. *arXiv:1909.01886v4* (2019).
- [17] Joule, J. *The London, Edinburgh, and Dublin Philosophical Magazine and Journal of Science* **30**(199), 76–87 (1847).
- [18] Kittel, C. *Physical Review* **110**(4), 836–841 (1958).
- [19] Akhiezer, A. I., Bar’iakhtar, V. G., and Peletminskii, S. V. *Sov. Phys. JETP* **35**, 157–164 (1959).
- [20] Belyaeva, O. Y., Karpachev, S. N., and Zarembo, L. K. *Soviet Physics Uspekhi* **35**(2), 106–122 (1992).
- [21] Jäger, J. V., Scherbakov, A. V., Linnik, T. L., Yakovlev, D. R., Wang, M., Wadley, P., Holy, V., Cavill, S. A., Akimov, A. V., Rushforth, A. W., and Bayer, M. *Applied Physics Letters* **103**(3), 032409 (2013).
- [22] Bombeck, M., Salasyuk, A. S., Glavin, B. A., Scherbakov, A. V., Brüggemann, C., Yakovlev, D. R., Sapega, V. F., Liu, X., Furdyna, J. K., Akimov, A. V., and Bayer, M. *Physical Review B* **85**(19) (2012).
- [23] Deb, M., Popova, E., Hehn, M., Keller, N., Mangin, S., and Malinowski, G. *Physical Review B* **98**(17) (2018).
- [24] Janušonis, J., Chang, C. L., van Loosdrecht, P. H. M., and Tobey, R. I. *Applied Physics Letters* **106**(18), 181601 (2015).
- [25] Kikkawa, T., Shen, K., Flebus, B., Duine, R. A., Ichi Uchida, K., Qiu, Z., Bauer, G. E., and Saitoh, E. *Physical Review Letters* **117**(20) (2016).
- [26] Hayashi, H. and Ando, K. *Physical Review Letters* **121**(23) (2018).



- 
- [27] Berk, C., Jaris, M., Yang, W., Dhuey, S., Cabrini, S., and Schmidt, H. *Nature Communications* **10**(1) (2019).
- [28] Atulasimha, J. and Flatau, A. B. *Smart Materials and Structures* **20**(4), 043001 (2011).
- [29] Verba, R., Lisenkov, I., Krivorotov, I., Tiberkevich, V., and Slavin, A. *Physical Review Applied* **9**(6) (2018).
- [30] Ruderman, M. A. and Kittel, C. *Physical Review* **96**(1), 99–102 (1954).
- [31] Honda, K. and Kaya, S. *Sci. Rep. Tohoku Univ.* **15**, 721 (1926).
- [32] J. W. Rampton, V. W. T. *Microwave Ultrasonics in Solid State Physics*. North Holland, (1972).
- [33] Kittel, C. *Reviews of Modern Physics* **21**(4), 541–583 (1949).
- [34] Farle, M. *Reports on Progress in Physics* **61**(7), 755–826 (1998).
- [35] Zingsem, B. W. Master's thesis, Universität Duisburg-Essen, (2016).
- [36] Encinas-Oropesa, A. and Dau, F. N. V. *Journal of Magnetism and Magnetic Materials* **256**(1-3), 301–305 (2003).
- [37] Parkes, D. E., Cavill, S. A., Hindmarch, A. T., Wadley, P., McGee, F., Staddon, C. R., Edmonds, K. W., Campion, R. P., Gallagher, B. L., and Rushforth, A. W. *Applied Physics Letters* **101**(7), 072402 (2012).
- [38] Kats, V. N., Linnik, T. L., Salasyuk, A. S., Rushforth, A. W., Wang, M., Wadley, P., Akimov, A. V., Cavill, S. A., Holy, V., Kalashnikova, A. M., and Scherbakov, A. V. *Physical Review B* **93**(21) (2016).
- [39] NIST. visited 20.07.2020.
- [40] Griffiths, J. H. E. *Nature* **158**(4019), 670–671 (1946).
- [41] Barman, A. and Sinha, J. *Spin Dynamics and Damping in Ferromagnetic Thin Films and Nanostructures*. Springer International Publishing, (2018).
- [42] Kamberský, V. *Czechoslovak Journal of Physics* **26**(12), 1366–1383 (1976).
- [43] Almeida, N. S. and Mills, D. L. *Physical Review B* **53**(18), 12232–12241 (1996).
- [44] Arias, R. and Mills, D. L. *Physical Review B* **60**(10), 7395–7409 (1999).
- [45] Twisselmann, D. J. and McMichael, R. D. *Journal of Applied Physics* **93**(10), 6903–6905 (2003).

- [46] Cochran, J. F., Heinrich, B., and Arrott, A. S. *Physical Review B* **34**(11), 7788–7801 (1986).
- [47] Banerjee, C., Pal, S., Ahlberg, M., Nguyen, T. N. A., Åkerman, J., and Barman, A. *RSC Advances* **6**(83), 80168–80173 (2016).
- [48] Kerr, J. *The London, Edinburgh, and Dublin Philosophical Magazine and Journal of Science* **3**(19), 321–343 (1877).
- [49] Yamamoto, S. and Matsuda, I. *Applied Sciences* **7**(7), 662 (2017).
- [50] Postava, K., Jaffres, H., Schull, A., Dau, F. N. V., Gorian, M., and Fert, A. R. *Journal of Magnetism and Magnetic Materials* , 172–199 (1997).
- [51] RockMechs. visited 20.07.2020.
- [52] Clark, A. E. In *Handbook of Ferromagnetic Materials*, 531–589. Elsevier (1980).
- [53] Madelung, O. *Semiconductors*. Springer Berlin Heidelberg, (2013).
- [54] Chen, J., Tzou, D., and Beraun, J. *International Journal of Heat and Mass Transfer* **49**(1-2), 307–316 (2006).
- [55] Spitzer, F., Glavin, B. A., Belotelov, V. I., Vondran, J., Akimov, I. A., Kasture, S., Achanta, V. G., Yakovlev, D. R., and Bayer, M. *Physical Review B* **94**(20) nov (2016).
- [56] Inc, E. O. visited 20.07.2020.
- [57] Rayleigh, L. *Proceedings of the London Mathematical Society* **s1-17**(1), 4–11 (1885).
- [58] Peterie, S. L., Miller, R. D., and Ivanov, J. *Kansas Geological Survey - Public Information Circular* **37** (2014).
- [59] Thomsen, C., Grahn, H. T., Maris, H. J., and Tauc, J. *Physical Review B* **34**(6), 4129–4138 (1986).
- [60] Matsuda, O., Larciprete, M. C., Voti, R. L., and Wright, O. B. *Elsevier Ultrasonics* **56**, 3–20 (2015).
- [61] Gibbs, M. R. J. *Modern Trends in Magnetostriction Study and Application*. Springer Netherlands Imprint Springer, Dordrecht, (2001).
- [62] Carr, W. J. and Smoluchowski, R. *Physical Review* **83**(6), 1236–1243 (1951).
- [63] Lee, E. W. *Reports on Progress in Physics* **18**(1), 184–229 (1955).

- 
- [64] Haus, H. A. *Waves and Fields in Optoelectronics (Prentice-Hall series in solid state physical electronics)*. Prentice Hall, (1983).
- [65] Novotny, L. *American Journal of Physics* **78**(11), 1199–1202 (2010).
- [66] Clark, A. E., Hathaway, K. B., Wun-Fogle, M., Restorff, J. B., Lograsso, T. A., Keppens, V. M., Petculescu, G., and Taylor, R. A. *Journal of Applied Physics* **93**(10), 8621–8623 (2003).
- [67] Gopman, D. B., Sampath, V., Ahmad, H., Bandyopadhyay, S., and Atulasimha, J. *IEEE Transactions on Magnetics* **53**(11), 1–4 (2017).
- [68] Clark, A. E., Wun-Fogle, M., Restorff, J. B., and Lograsso, T. A. *MATERIALS TRANSACTIONS* **43**(5), 881–886 (2002).
- [69] Clark, A. E. *Journal of Intelligent Material Systems and Structures* **4**(1), 70–75 (1993).
- [70] Guruswamy, S., Jayaraman, T. V., Corson, R. P., Garside, G., and Thuanboon, S. *Journal of Applied Physics* **104**(11), 113919 (2008).
- [71] Zhang, Y. and Wu, R. *IEEE Transactions on Magnetics* **47**(10), 4044–4049 (2011).
- [72] Antonucci, L., Bonvalet, A., Solinas, X., Daniault, L., and Joffre, M. *Optics Express* **23**(21), 27931 (2015).
- [73] Breuer, M., Beck, M., Wolfring, B., Paasch-Colberg, T., Bartels, A., Bayer, M., and Handloser, M. *Pro-Physik*, 24 (2017).
- [74] Fermann, M. E. (1997).
- [75] New Focus, Inc. *10-MHz Adjustable Balanced Photoreceivers - Models 2107 and 2117*, 200331, rev. a edition, (2004).
- [76] Ordal, M. A., Bell, R. J., Alexander, R. W., Newquist, L. A., and Querry, M. R. *Applied Optics* **27**(6), 1203 (1988).
- [77] Skauli, T., Kuo, P. S., Vodopyanov, K. L., Pinguet, T. J., Levi, O., Eyres, L. A., Harris, J. S., Fejer, M. M., Gerard, B., Becouarn, L., and Lallier, E. *Journal of Applied Physics* **94**(10), 6447–6455 (2003).
- [78] H. S. Carslaw, J. C. J. *Conduction of Heat in Solids*. Oxford University Press, (1986).
- [79] Bird, R. B., Stewart, W. E., and Lightfoot, E. N. *Transport Phenomena*. John Wiley & Sons, (1960).

- [80] Anwar, M. S. and Zia, W. *Review of Scientific Instruments* **81**(12), 124904 (2010).
- [81] Young, H. D. *University Physics*. Addison-Wesley, 7th edition, (1991). Table 15-5.
- [82] Sokolov, A. V. *Optical Properties of Metals*. London, Blackie, (1967). p. 311.
- [83] Pincus, P. *Physical Review* **118**(3), 658–664 (1960).
- [84] Fan, Y., Zhao, H. B., Lüpke, G., Hanbicki, A. T., Li, C. H., and Jonker, B. T. *Physical Review B* **85**(16) (2012).
- [85] Rado, G. T. and Weertman, J. R. *J. Phys. Chem. Solids* **11**, 315–333 (1959).
- [86] Shihab, S., Riahi, H., Thevenard, L., von Bardeleben, H. J., Lemaître, A., and Gourdon, C. *Applied Physics Letters* **106**(14), 142408 (2015).
- [87] Inst., A. G. I. P.-T., Petersburg, S., Gurevich, R., and Melkov, G. A. *Magnetization Oscillations and Waves*. Taylor & Francis Inc, (1996).
- [88] Scherbakov, A., Danilov, A., Godejohann, F., Linnik, T., Glavin, B., Shelukhin, L., Pattnaik, D., Wang, M., Rushforth, A., Yakovlev, D., Akimov, A., and Bayer, M. *Physical Review Applied* **11**(3) (2019).
- [89] Budhathoki, S., Sapkota, A., Law, K. M., Nepal, B., Ranjit, S., KC, S., Mewes, T., and Hauser, A. J. *Journal of Magnetism and Magnetic Materials* **496**, 165906 (2020).
- [90] Carpenne, E., Mancini, E., Dazzi, D., Dallera, C., Puppini, E., and Silvestri, S. D. *Physical Review B* **81**(6) (2010).
- [91] Kisielewski, J., Kirilyuk, A., Stupakiewicz, A., Maziewski, A., Kimel, A., Rasing, T., Baczewski, L. T., and Wawro, A. *Physical Review B* **85**(18) (2012).
- [92] Chen, L., Mankovsky, S., Wimmer, S., Schoen, M. A. W., Körner, H. S., Kronseder, M., Schuh, D., Bougeard, D., Ebert, H., Weiss, D., and Back, C. H. *Nature Physics* **14**(5), 490–494 (2018).
- [93] Linnik, T. L., Scherbakov, A. V., Yakovlev, D. R., Liu, X., Furdyna, J. K., and Bayer, M. *Physical Review B* **84**(21) (2011).
- [94] Besse, V., Golov, A., Vlasov, V., Alekhin, A., Kuzmin, D., Bychkov, I., Kotov, L., and Temnov, V. *Journal of Magnetism and Magnetic Materials* **502**, 166320 (2020).
- [95] Lenz, K., Wende, H., Kuch, W., Baberschke, K., Nagy, K., and Jánossy, A. *Physical Review B* **73**(14) (2006).

- 
- [96] Woltersdorf, G. and Heinrich, B. *Physical Review B* **69**(18) (2004).
- [97] Damon, R. W. *physica status solidi (b)* **8**(2), K89–K93 (1965).
- [98] Zhai, Y., Ni, C., Xu, Y., Xu, Y. B., Wu, J., Lu, H. X., and Zhai, H. R. *Journal of Applied Physics* **101**(9), 09D120 (2007).
- [99] C. K. Mewes, T. M. *Handbook of Nanomagnetism*, chapter Relaxation in Magnetic Materials for Spintronics, 71–96. Pan Stanford Publishing, Singapore (2015).
- [100] Aspnes, D. E., Kelso, S. M., Logan, R. A., and Bhat, R. *Journal of Applied Physics* **60**(2), 754–767 (1986).
- [101] Scherbakov, A. V., Bombeck, M., Jäger, J. V., Salasyuk, A. S., Linnik, T. L., Gusev, V. E., Yakovlev, D. R., Akimov, A. V., and Bayer, M. *Optics Express* **21**(14), 16473 (2013).
- [102] Körmann, F., Grabowski, B., Dutta, B., Hickel, T., Mauger, L., Fultz, B., and Neugebauer, J. *Physical Review Letters* **113**(16) (2014).
- [103] Man, H., Shi, Z., Xu, G., Xu, Y., Chen, X., Sullivan, S., Zhou, J., Xia, K., Shi, J., and Dai, P. *Physical Review B* **96**(10) (2017).
- [104] Nivedita, L. R., Kumar, V. V. S., Asokan, K., and Rajendrakumar, R. T. *Materials Research* **18**(5), 946–952 (2015).
- [105] Dotsenko, S. A., Galkin, N. G., Koval, L. V., and Polyarnyi, V. O. *e-Journal of Surface Science and Nanotechnology* **4**, 319–329 (2006).
- [106] Nardi, D., Travagliati, M., Siemens, M. E., Li, Q., Murnane, M. M., Kapteyn, H. C., Ferrini, G., Parmigiani, F., and Banfi, F. *Nano Letters* **11**(10), 4126–4133 (2011).
- [107] COMSOL Multiphysics® v. 5.4., <http://www.comsol.com>, COMSOL AB, Stockholm, Sweden.
- [108] Hadj-Larbi, F. and Serhane, R. *Sensors and Actuators A: Physical* **292**, 169–197 (2019).
- [109] Sadhu, J., Lee, J. H., and Sinha, S. *Applied Physics Letters* **97**(13), 133106 (2010).
- [110] Kukhtaruk, S. M., Rushforth, A. W., Godejohann, F., Scherbakov, A. V., and Bayer, M. *arXiv:2006.14394v1* (2020).
- [111] Weiler, M., Dreher, L., Heeg, C., Huebl, H., Gross, R., Brandt, M. S., and Goennenwein, S. T. B. *Physical Review Letters* **106**(11) (2011).

## BIBLIOGRAPHY

---

- [112] Matthews, H. and LeCraw, R. C. *Physical Review Letters* **8**(10), 397–399 (1962).
- [113] Scott, R. Q. and Mills, D. L. *Physical Review B* **15**(7), 3545–3557 (1977).
- [114] Herskind, P. F., Dantan, A., Marler, J. P., Albert, M., and Drewsen, M. *Nature Physics* **5**(7), 494–498 (2009).
- [115] Fano, U. *Physical Review* **124**(6), 1866–1878 (1961).
- [116] Liu, C., Chen, J., Liu, T., Heimbach, F., Yu, H., Xiao, Y., Hu, J., Liu, M., Chang, H., Stueckler, T., Tu, S., Zhang, Y., Zhang, Y., Gao, P., Liao, Z., Yu, D., Xia, K., Lei, N., Zhao, W., and Wu, M. *Nature Communications* **9**(1) (2018).
- [117] Khokhlov, N., Gerevenkov, P., Shelukhin, L., Azovtsev, A., Pertsev, N., Wang, M., Rushforth, A., Scherbakov, A., and Kalashnikova, A. *Physical Review Applied* **12**(4) (2019).
- [118] Toedt, J.-N., Mundkowski, M., Heitmann, D., Mendach, S., and Hansen, W. *Scientific Reports* **6**(1) (2016).
- [119] Whitehead, N. J., Horsley, S. A. R., Philbin, T. G., and Kruglyak, V. V. *Applied Physics Letters* **113**(21), 212404 (2018).
- [120] Hämäläinen, S. J., Madami, M., Qin, H., Gubbiotti, G., and van Dijken, S. *Nature Communications* **9**(1) (2018).
- [121] Khitun, A., Nikonov, D. E., and Wang, K. L. *Journal of Applied Physics* **106**(12), 123909 (2009).
- [122] Kobecki, M., Scherbakov, A. V., Linnik, T. L., Kukhtaruk, S. M., Gusev, V. E., Pattnaik, D. P., Akimov, I. A., Rushforth, A. W., Akimov, A. V., and Bayer, M. *Nature Communications* **11**(1) aug (2020).
- [123] MATLAB<sup>®</sup> v. R2016b, [www.mathworks.com](http://www.mathworks.com).
- [124] Weisstein, E. W. Wolfram Web Resource. <https://mathworld.wolfram.com/LorentzianFunction.html>, checked on 19.08.2020.

# Scientific Contributions

## Publications

”Long distance waveguiding of sub-terahertz phonon bunch beneath nano-corrugated surface”

D. Yaremkevich, A. V. Scherbakov, S. M. Kukhtaruk, T. L. Linnik, N. E. Khokhlov, **F. Godejohann**, O. A. Dyatlova, A. Nadzeyka, R. P. Campion, D. P. Pattnaik, A. W. Rushforth, V. E. Gusev, A. V. Akimov and M. Bayer (in preparation)

”Controlling magnon characteristics in thin ferromagnetic nanogratings by changing the direction of in-plane magnetic fields”

S. M. Kukhtaruk, A. W. Rushforth, **F. Godejohann**, A. V. Scherbakov, A. V. Akimov and M. Bayer, arXiv:2006.14394 (June 2020)

”Magnon polaron formed by selectively coupled coherent magnon and phonon modes of a surface patterned ferromagnet”

**F. Godejohann**, A. V. Scherbakov, S. M. Kukhtaruk, A. N. Poddubny, D. D. Yaremkevich, M. Wang, A. Nadzeyka, D. R. Yakovlev, A. W. Rushforth, Andrey V. Akimov, Manfred Bayer, arXiv:1909.01886 (September 2019)

”Optical Excitation of Single- and Multimode Magnetization Precession in Fe-Ga Nanolayers”

A.V. Scherbakov, A.P. Danilov, **F. Godejohann**, T.L. Linnik, B.A. Glavin, L.A. Shelukhin, D.P. Pattnaik, M. Wang, A.W. Rushforth, D.R. Yakovlev, A.V. Akimov and M. Bayer, Physical Review Applied 11(3) (March 2019)

---

## Talks and Conferences

DPG spring meeting 2018 in Berlin, Germany: Poster: 'Resonant Interaction of Coherent Magnons and Phonons in a Ferromagnetic Nanograting'

Laser Ultrasonics Conference 2018 in Nottingham, UK (13.7.2018): 20 min oral presentation: 'Driving of Magnetization Precession by Laser Ultrasonics in Ferromagnetic Nanogratings'

9th Joint European Magnetic Symposia (JEMS) Conference 2018 in Mainz, Germany: Poster: 'Ultrafast Magnon-Phonon Dynamics in Lateral Gallenol Nanogratings'

The European School on Magnetism 2018 in Krakau, Poland: Poster: 'Driving of the Magnetization Precession by Coherent Phonons in Nanoscale-patterned Ferromagnetic Films'

7<sup>th</sup> Son Et Lumière school 2019 in Les Houches, France: Poster: 'Strong Interaction of Optically Excited Coherent Phonons and Magnons in a Nanoscale-patterned Ferromagnetic Film'

International Collaborative Research Centre TRR 160 seminar at the TU Dortmund, Germany (09.05.2019): 45 min oral presentation: 'Magneto-Elastic Coupling in Ferromagnetic Nanogratings'

4<sup>th</sup> Ultrafast Magnetism Conference 2019 in York, UK (14.10.2019): 15 min oral presentation: 'Coherent dynamics of strongly coupled magnons and phonons in ferromagnetic nanogratings'



# Acknowledgments

First and foremost I would like to thank Prof. Dr. Manfred Bayer for the opportunity to perform these studies within the "Nanomagnetron" project. I am also greatly thankful to Dr. Alexey Scherbakov for his support and assistance during the experimental research and paper works. Without his advises, I could not attained this level and completed this thesis. A special Thank You deserves Dr. Serhii Kukhtaruk for his theoretical support and our lovely discussions about physics and life. Moreover, I want to thank Prof. Dr. Andrew Rushforth for being my second referee and Dr. Kai Göpel for proofreading my thesis. Finally, I would like to thank all E2-members for a great working atmosphere and, of course, my family and friends, especially my girlfriend Jessi, for their lovely non-scientific support. Thank you for everything.



# Appendix A

## Appendix

### A.1 Pump Pulse Characteristics

The laser pulse's intensity perpendicular to the propagation direction is distributed as Gaussian function according to

$$I(x,y) = I_0 \exp\left(-\ln(2)\frac{x^2 + y^2}{r_{1/2}^2}\right), \quad (\text{A.1})$$

where  $I_0 = I(0,0)$  is the intensity at the center of the pump pulse and  $r_{1/2}$  is the half width at half maximum (HWHM) of the laser intensity, i.e. the laser spot's radius. The corresponding power to equation A.1 reads

$$P = \int_{-\infty}^{\infty} \int_{-\infty}^{\infty} I_0 \exp\left(-\ln(2)\frac{x^2 + y^2}{r_{1/2}^2}\right) dx dy = I_0 \frac{\pi r_{1/2}^2}{\ln(2)}. \quad (\text{A.2})$$

For a pulsed laser system with a repetition rate  $f$ , the energy density per pump pulse reads

$$E_p = I_0 f = \frac{\ln(2) P f}{\pi r_{1/2}^2}. \quad (\text{A.3})$$

Hence, the absorbed power of a laser pulse with optical absorption depth  $\zeta_{\text{pu}}$  reads

$$P(z) = \frac{(1 - R_{\text{pu}}) E_p}{\zeta_{\text{pu}}} \exp\left(-\frac{z}{\zeta_{\text{pu}}}\right), \quad (\text{A.4})$$

where  $R_{\text{pu}}$  is the pulse's reflection coefficient. By additionally considering the transient pulse duration  $\tau_{\text{fs}}$  (full width half maximum (FWHM)) of a femtosecond-optical pulse, equation A.4 can be extended to [122](Supplementary Information)

$$P(z,t) = P(z) \cdot \sqrt{\frac{2}{\pi}} \frac{1}{\tau_{\text{fs}}} e^{-2\frac{t^2}{\tau_{\text{fs}}^2}}. \quad (\text{A.5})$$

In order to quantify the sizes of the pump spots for both excitation geometries, transient reflection signals for different positions of the pump pulse relatively to the probe pulse are measured. In the case of frontside excitation, the amplitude of the sharp increase is used to quantify the spatial overlap of the pump and probe pulses. Such a sharp

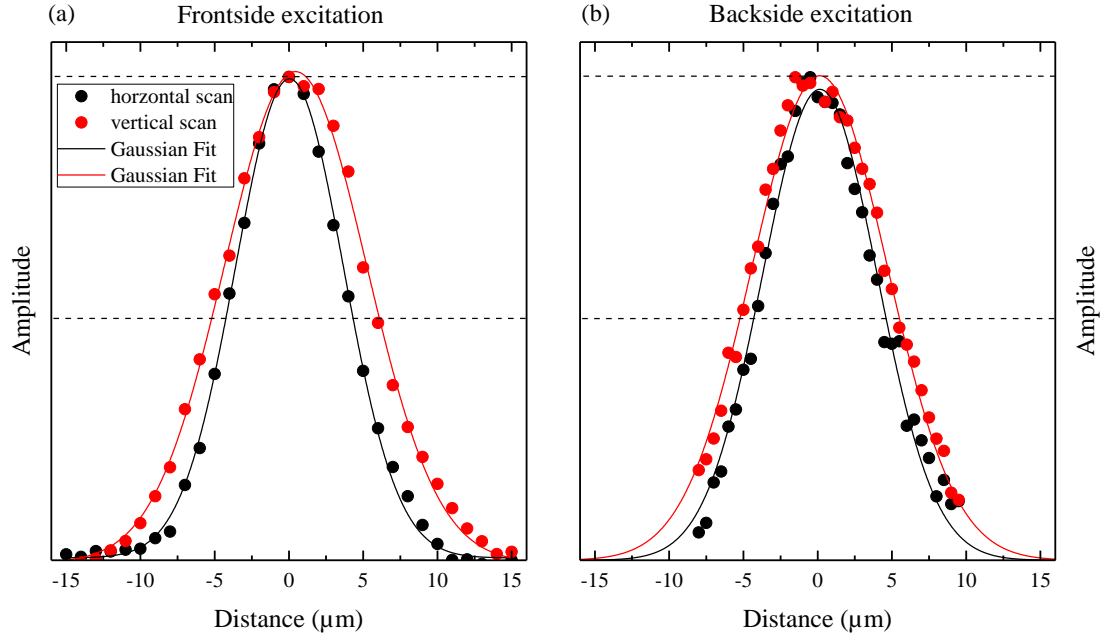


**Figure A.1:** Estimated size of pump spots for different excitation geometries. The regression have been performed according to equation A.1. (a) Excitation from the frontside of the sample, whereas the pump pulse has an angle of incidence of  $45^\circ$  with respect to the surface normal. (b) Excitation from the backside of the sample, whereas the pump pulse has an angle of incidence of  $90^\circ$  with respect to the surface normal.

increase is presented in figure 3.7(a), especially in its inset. For the case of backside excitation, the positive amplitude of the bipolar strain pulse is considered (upper inset in figure 3.7(b)). Figure A.1 summarizes the results of horizontal ( $x$ -direction) and vertical ( $y$ -direction) scans for each excitation geometry. These measurements have been performed by means of an automatized MATLAB program, which controls a piezoelectric translation stage with nm precision. Regressions according to equation A.1 are performed and presented in figure A.1 for the  $x$ - and  $y$ -direction. The evaluated spot radii (HWHM) for frontside excitation read

$$\text{HWHM}_{\text{FS}}^{\text{horizontal}} = (4.3 \pm 0.1) \mu\text{m}, \quad (\text{A.6})$$

$$\text{HWHM}_{\text{FS}}^{\text{vertical}} = (5.6 \pm 0.1) \mu\text{m} \quad (\text{A.7})$$

For backside excitation the spot radii read

$$\text{HWHM}_{\text{BS}}^{\text{horizontal}} = (4.6 \pm 0.1) \mu\text{m}, \quad (\text{A.8})$$

$$\text{HWHM}_{\text{BS}}^{\text{vertical}} = (5.4 \pm 0.3) \mu\text{m}, \quad (\text{A.9})$$

which results in an average radius of roughly  $5 \mu\text{m}$  for both excitation geometries.

## A.2 MATLAB® Software for Remote Control and Data Analysis

The software used for remote control of the setup and for fast data analysis is realized in MATLAB® (MATLAB) [123]. Depending on the purpose of the measurement, different kind of programs with convenient graphical user interfaces (GUIs) have been developed. In the following the most powerful and important programs are shortly discussed.

### A.2.1 Software for Remote Control

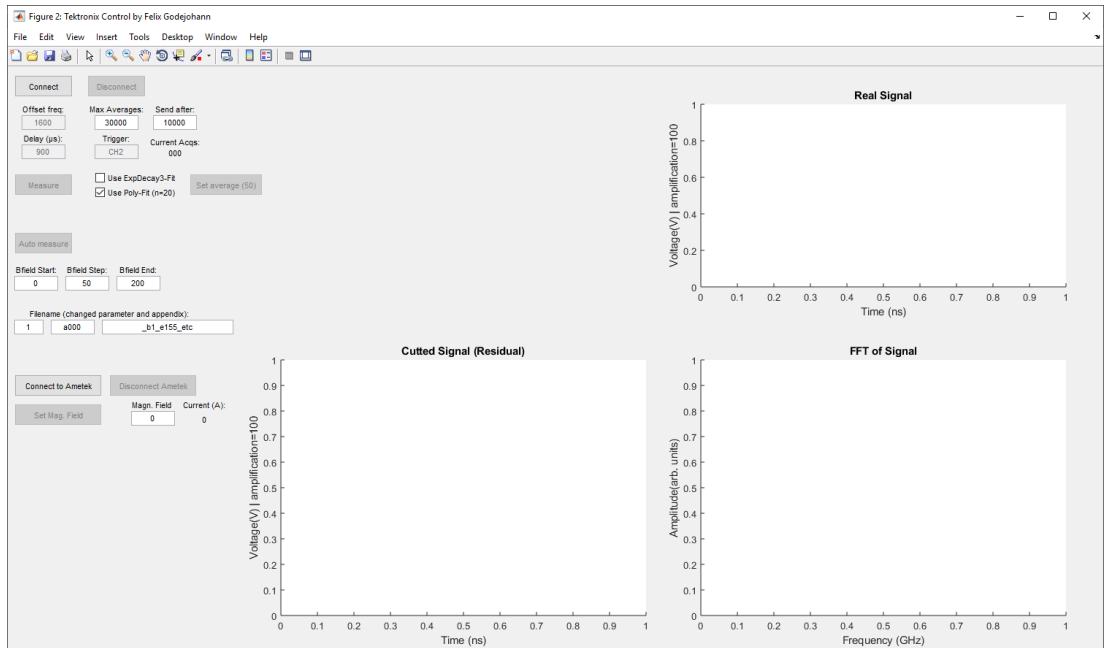


**Figure A.2:** GUI, which is used for data acquisition. The program is able to communicate with the oscilloscope and the power supply of the magnet. After each measurement a rough analysis of the oscillating signal is given. Besides single measurements, also automatized magnetic field dependent measurements are possible.

The program displayed in figure A.2 is mainly used for the experiments in this work. It is able to connect to an oscilloscope and to pre-set all import parameters, which have been introduced in the previous section. Using editable text boxes the accumulation

of each measurement is adjustable. Hereby, a first accumulation is done on the internal memory of the oscilloscope (*Sent after*), which is sent to the computer afterwards. On the computer another accumulation of each signal send by the oscilloscope is done (*Max. averages*). This is necessary, because the maximum accumulation of the internal memory is given by  $10^4$  samples, while reasonable signal to noise ratios usually need an amount of samples between  $10^4$  and  $10^6$ . In order to adjust the magnetic field strength, the program is able to operate a power supply via a USB connection. Once connected to the power supply an arbitrary positive magnetic field in mT is set by filling the text box and pressing the *Set Mag. Field* button. The linear relation between the applied current and the resulting magnetic field is shown in equation 3.6. In addition to single measurements, it is possible to scan through a magnetic field range with a certain step size. This scanning is realized by filling the corresponding text boxes and by pressing the *Auto measure* button. It is important to mention that the sample starts to be displaced for magnetic fields  $> 100$  mT. The total displacement for high magnetic fields can reach several microns. Therefore, scans within a broad magnetic field range may have additional features given by the displacement. Nevertheless, such fast and automatized scans are used to get a first impression on a magnetic field dependence of changes in the reflection or PMOKE. A possible solution to compensate the drift of the sample is given by an autofocus module provided by MATLAB, which controls the piezo-electrical stage and ensures an optimized focus of the sample's surface and the probe spot.

The measured data is displayed by several plots: the first plot at the top right displays the accumulated time-resolved raw data. The second and third plot show the corresponding transient signals with its corresponding Fast Fourier Transformation (FFT), respectively, where the background is removed by, either a sum of three exponential functions, or a 20<sup>th</sup>-order polynomial function. In general, a rectangular window as FFT window is used, however every other window can be easily set in the MATLAB code. Using these three plots, a fast data analysis of every transient signal is done immediately after every measurement. For further analysis, another more powerful software can be used, which is discussed in section A.2.2.

For spatially resolved PMOKE or reflection measurements another program controlling the piezoelectric translation stage is used. As mentioned in section 3.2.3, this translation stage is used to adjust the position of the microscope objective in three dimensions. For communication the MATLAB interface to the Microsoft<sup>®</sup> .NET Framework is used. A GUI leads to a convenient operation by the user. With the help of this program spatially scans with a certain angle in one and two dimensions are possible. An experimental example using this software is given in section A.1, where the pump spot sizes for different excitation geometries are investigated.

## A.2.2 Software for Data Analysis

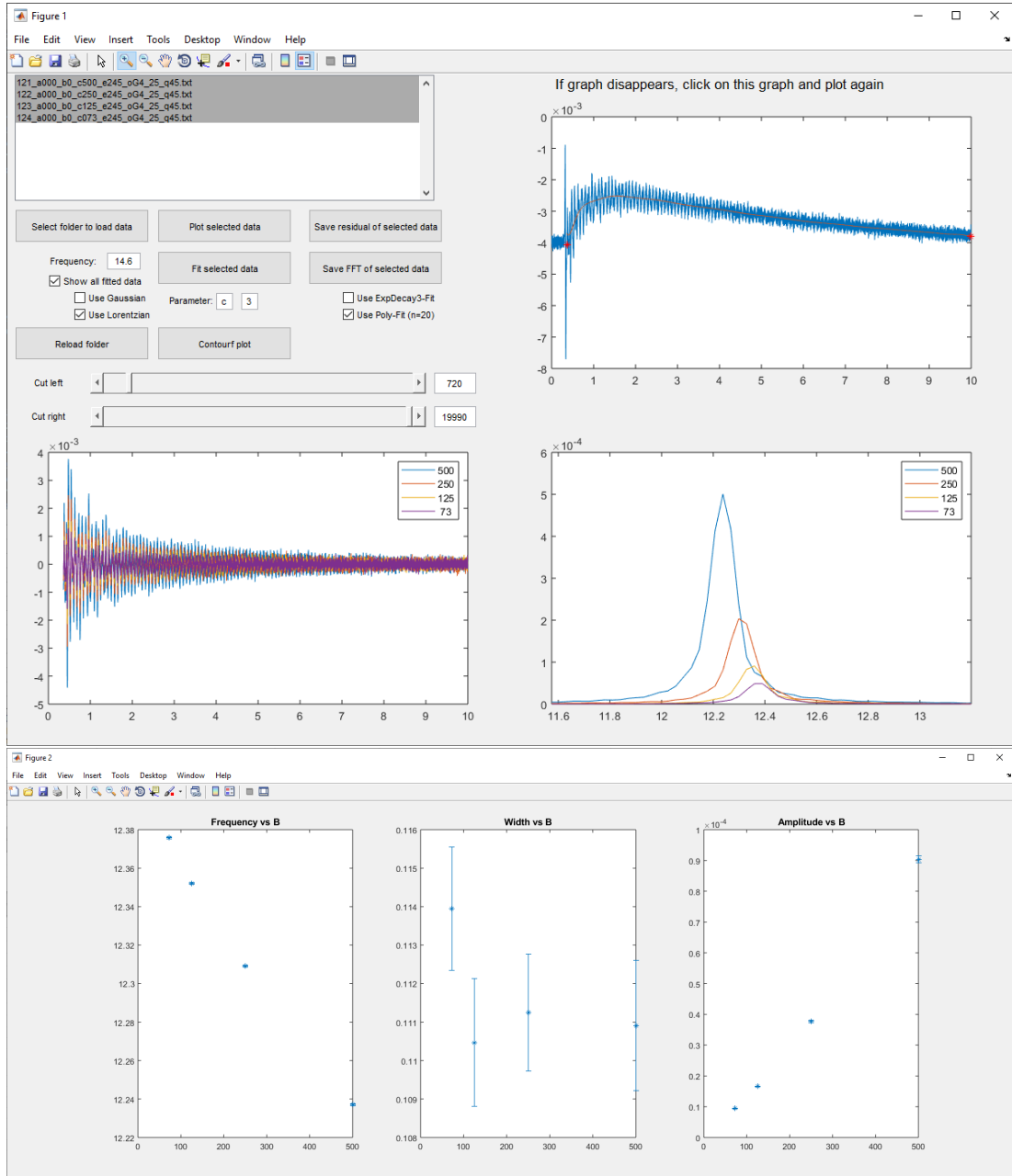


**Figure A.3:** (top) This figure demonstrates the GUI used for a careful and fast data analysis. It is possible to import data from directory and selectively plot certain files. By selecting several files, a full set can be analyzed at once. Depending on the parameter of interest, a quantitative analysis can be done, as well. (bottom) Using the *Fit selected data* button Lorentzian regressions are used to fit one line in the power spectrum in order to directly see the dependence on the selected parameter. In This particular case the power dependence of an acoustic mode in a nanograting is shown.

In order to have a fast data analysis, a powerful GUI developed in MATLAB is used; see figure A.3(top). The program is able to load a folder of data into a list box

and to analyze the select data files of interest. During a series of measurements it is possible to insert new data files by a reload button, so that they can be checked and analyzed immediately. In order to check a signal and its spectrum in a particular time window, two sliders can be used to trim the transient signal. This can be also done by setting the interesting data points of the interval with two editable text boxes. For the sake of clarity in the top right graph the chosen interval with the calculated regression function of the raw data is displayed in red. The regression function can either be selected as a sum of three exponential functions or a 20<sup>th</sup>-order polynomial function. Having the so-called residual signal (bottom left plot in figure A.3(top)), a FFT yields the corresponding frequency spectrum (bottom right plot). Depending on the interest different FFT windows can be useful. By selecting several data files, the previously mentioned steps are performed for all selected signals. With the *Parameter* text boxes, a letter and its following amount of significant digits can be set. Now, several measurements can be plotted dependent on a certain parameter such as the external magnetic field strength indicated by the value  $a$ . In addition, there are buttons to save the residuals of the selected signals and their FFT spectra, as well. In order to quantitatively analyze peaks at a certain frequency of the selected FFT spectra, the *Fit selected data* button performs Lorentzian or Gaussian regressions of the selected signals depending on the chosen parameter. After doing so, new figures are generated showing the parameter dependence of the peak frequencies, widths and amplitudes; see figure A.3(bottom). Moreover, the calculated regression functions and the peaks of the FFT spectra are shown to assess the performed regressions on its validity.



### A.3 Comparison of an Analysis in Time and Frequency Domain

In general, there are two possible ways to determine characteristic values of oscillating signals: an analysis in time domain or in frequency domain. Figure A.4(a) shows three experimentally measured damped oscillating signals with different amplitudes and lifetimes (coloured open circles). For a quantitative analysis in time domain, an exponentially damped sin-function with amplitude

$$A(t) = A_0 e^{-\gamma t} \sin(2\pi f t + \Psi) \quad (\text{A.10})$$

can be used. Here,  $A_0$  is the initial precession amplitude,  $\gamma = \frac{1}{\tau}$  is the damping coefficient,  $\tau$  is the lifetime,  $f_0$  is the signal's frequency and  $\Psi$  is a phase. For an analysis in the frequency domain, however, a fast fourier transform (FFT) is being utilized (see figure A.4(b)). A quantitative analysis of the resulting power spectrum (coloured open circles) is described by a Lorentzian function

$$L(f) = \frac{L_0}{2\pi} \frac{\Delta f}{(f - f_0)^2 + \frac{\Delta f^2}{4}}, \quad (\text{A.11})$$

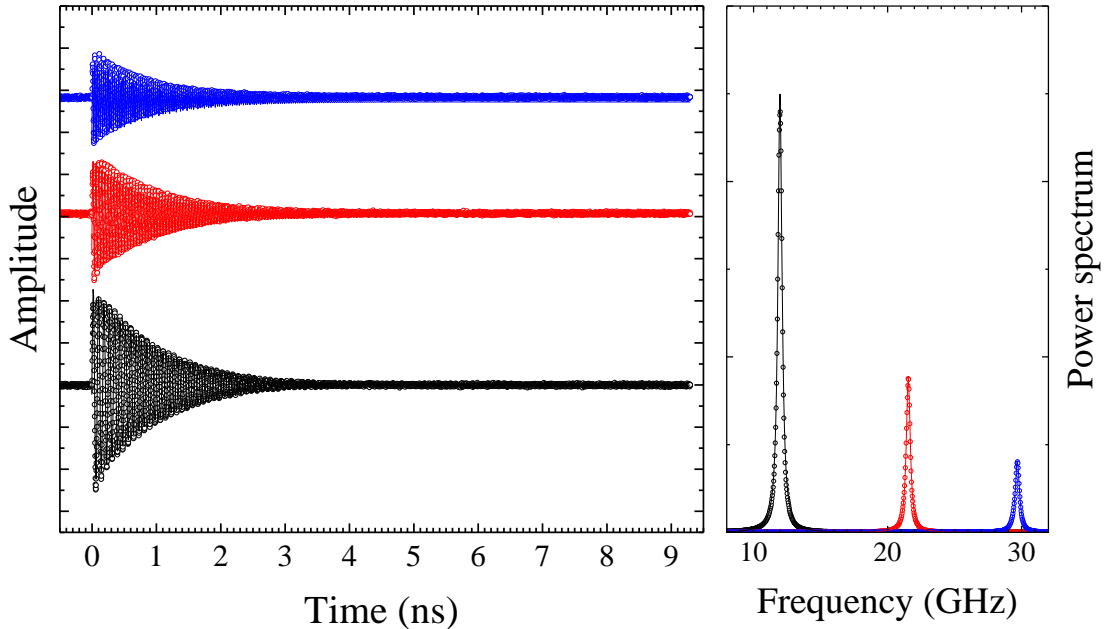


**Figure A.4:** Three experimentally measured damped oscillating signals with different amplitudes and lifetimes (open circles). Respective regressions using equation A.10 are presented, as well (line). (b) Corresponding power spectra of the signals in (a) (open circles). The shown resonances are fitted using equation A.11 (lines).

where  $L_0$  describes the maximum spectral power at  $f_0$  and  $\Delta f$  describes the resonance's full width at half maximum (FWHM) (coloured lines). The latter is also known as the spectral linewidth of the resonance. The relation between the damping coefficient  $\gamma$  in equation A.10 and  $\Delta f$  in equation A.11 is given by [124]

$$\gamma = \pi \Delta f. \quad (\text{A.12})$$

The latter equation can be used to calculate the signal's lifetime  $\tau = \frac{1}{\gamma} = \frac{1}{\pi \Delta f}$ <sup>1</sup>. An explicit quantitative analysis of the evaluated damping coefficients and linewidths of figure A.4 are listed in table A.1. The evaluated linewidths using equation A.11

Signal	$\frac{\gamma}{\pi}$ (GHz)	$\Delta f$ (GHz)
black	$0.315 \pm 0.001$	$0.3630 \pm 0.0001$
red	$0.300 \pm 0.010$	$0.3460 \pm 0.0001$
blue	$0.335 \pm 0.010$	$0.3770 \pm 0.0001$

**Table A.1:** Evaluated parameters of the regressions shown in figure A.4.

are always larger than the damping coefficients  $\gamma$  using equation A.10. The slight overestimation of the regressions in the frequency domain is due to the used fixed time window of the experimentally measured signals. The time window of 10 ns corresponds to a minimal linewidth of 0.2 GHz, which lies in the range of the evaluated signals' linewidths. Therefore, this work focuses on regressions in the time domain than in the frequency domain.

## A.4 Analysis of Transient PMOKE Signals at 30, 110 and 140 mT

Figure A.5 presents transient PMOKE signals and their corresponding power spectra for three different magnetic fields, i.e.  $B = 30, 110$  and  $140$  mT. These signals correspond to the signals shown in figure 5.7 on page 78. In addition to the measured signals, regressions using a sum of damped sine functions are displayed, as well. The sum of damped sine functions is defined according to

$$\delta m_z = \sum_{i=0}^n m_i^0 e^{-\gamma_i t} \sin(2\pi f_i t), \quad (\text{A.13})$$

where  $m_i^0$ ,  $\gamma_i = \pi \Delta f_i$  and  $f_i$  is the respective amplitude, damping parameter and frequency, respectively.  $\Delta f_i$  is the full width at half maximum (FWHM) of the corresponding power spectrum (see section A.3). The TR-PMOKE signal measured at

---

<sup>1</sup>This relation is very helpful to discuss damped oscillating signals both in time and frequency domain.

30 mT, contains three modes, which can be attributed to the FM, QTA and QLA mode (see figures A.5(a),(b)). A regression according to equation A.13 ( $n = 3$ ) nicely describes both the transient signal and its corresponding frequency spectrum. All evaluated frequencies ( $f_i$ ) and FWHMs ( $\Delta f_i$ ) are listed in table A.2. The non-zero amplitudes of the QTA and QLA modes can be explained by the resonance with high-order magnon modes (see chapter 4). Figures A.5(c),(d) discuss measured and fitted signals at  $B = 110$  mT. Similar to the previous regression at  $B = 30$  mT, a regression using eq. A.13 ( $n = 3$ ) has been performed, as well (see table A.2). The evaluated frequency splitting around the 13.1 GHz line reads  $\Gamma_{\text{eval}} = f_2 - f_1 \approx 0.35 \text{ GHz} \approx 0.4 \text{ GHz}$ . Figures A.5(e),(f) discuss measured and fitted signals at  $B = 140$  mT, where the QLA mode possesses a huge amplitude. Due to the single contributions to the transient signal for times  $> 0.7$  ns, only a regression using one frequency ( $n = 1$ ) has been used (see table A.2). The discrepancy between the regression and the measured signal in figure A.5(e) finds its origin in the beating between the contributions given by the QTA and QLA lines. A small contribution to the frequency spectrum at the QTA line can be also seen in figure A.5(f) at 13.1 GHz.

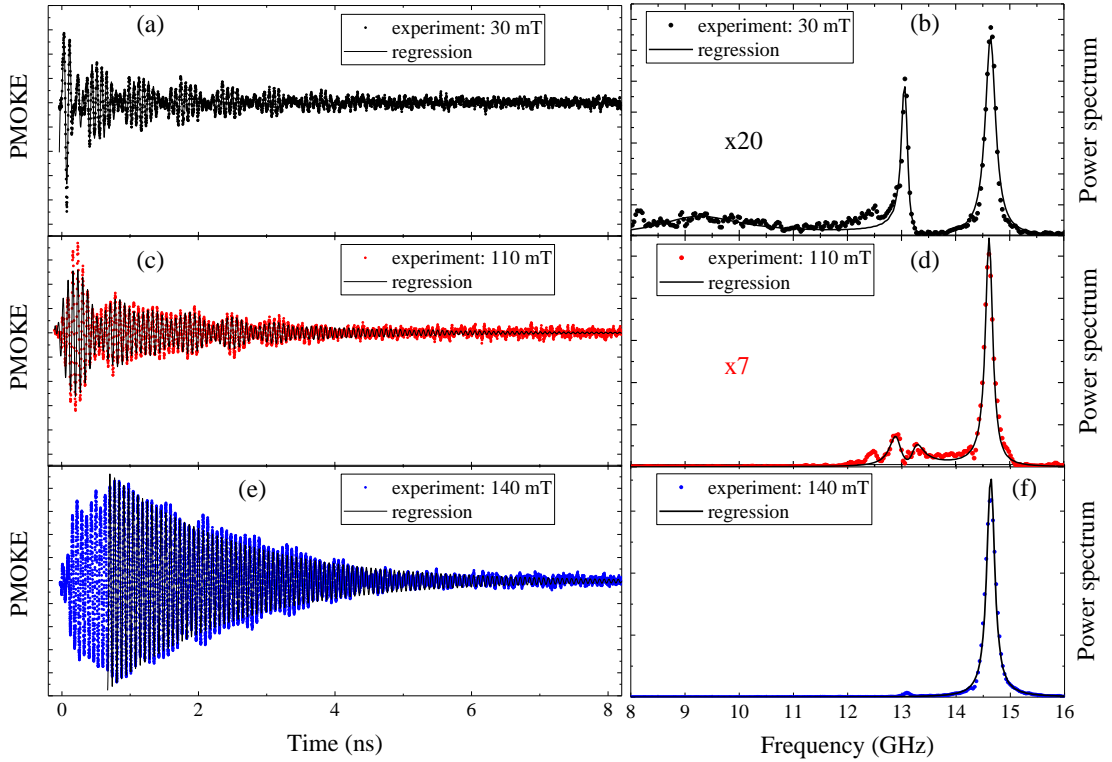


**Figure A.5:** Transient PMOKE measurements and their corresponding frequency spectra for magnetic field strengths of (a),(b) 30, (c),(d) 110 and (e),(f) 140 mT (circles). The regressions are performed using equation A.13 with  $n = 3$  (lines). The PMOKE measurement at 140 mT only contains one spectral line for times after 0.7 ns, whereas a regression using a single damped sine ( $n = 1$ ) is used.

$B$ (mT)	30	110	140
$f_1$ (GHz)	$9.17 \pm 0.02$	$12.91 \pm 0.02$	-
$\Delta f_1$ (GHz)	$1.88 \pm 0.02$	$0.27 \pm 0.02$	-
$f_2$ (GHz)	$13.06 \pm 0.02$	$13.25 \pm 0.02$	-
$\Delta f_2$ (GHz)	$0.13 \pm 0.02$	$0.27 \pm 0.02$	-
$f_3$ (GHz)	$14.64 \pm 0.02$	$14.61 \pm 0.02$	$14.64 \pm 0.02$
$\Delta f_3$ (GHz)	$0.23 \pm 0.02$	$0.16 \pm 0.02$	$0.16 \pm 0.02$

**Table A.2:** Evaluated parameters which correspond to figure A.5.

## A.5 Different Regimes of Coupling

The magneto-elastic coupling between certain magnon and phonon modes can be described by a system of coupled oscillators according to (see equation 2.69)

$$\frac{1}{2\pi} \frac{da_j}{dt} - if_j a_j + \frac{\Delta f_j}{2} a_j + i \sum_l K_{jl} a_l = A_j, \quad (\text{A.14})$$

where  $a_j$  are complex amplitudes,  $\Delta f_j$  are spectral linewidths (FWHM),  $A_j$  are excitation amplitudes and  $j = \text{QTA}^*, \text{QLA}, \text{FM}$ . The specific magneto-elastic interaction of the considered magnon and phonon modes is described by a coupling tensor

$$\hat{K} = \begin{pmatrix} 0 & 0 & K_{\text{QTA}^*} \\ 0 & 0 & K_{\text{QLA}} \\ K_{\text{QTA}^*} & K_{\text{QLA}} & 0 \end{pmatrix}. \quad (\text{A.15})$$

At the resonance of the magnon mode with the certain phonon mode the solutions for the resonance frequency read:

$$f_{\text{R},l} = f_l - i \frac{\Delta f_{\text{FM}} + \Delta f_l}{4} \pm \sqrt{K_l^2 - \left( \frac{\Delta f_{\text{FM}} - \Delta f_l}{4} \right)^2} \quad (\text{A.16})$$

where  $l$  stands for  $\text{QTA}^*$  or  $\text{QLA}$ ,  $f_l$  is the frequency of the uncoupled  $\text{QTA}^*$  or  $\text{QLA}$  modes. The real and imaginary part of  $f_{\text{R},l}$  gives the frequency and damping of the corresponding hybridized magnon-phonon mode. In the case of strong coupling, when  $K_l > \left| \frac{\Delta f_{\text{FM}} - \Delta f_l}{4} \right|$ , the hybridized state possesses the normal mode splitting and the linewidth for the split peaks is given by the arithmetic average  $\Delta f_{\text{R}} = \frac{\Delta f_{\text{FM}} + \Delta f_l}{2}$ . In the case of weak (or moderate) coupling, where  $K_l < \left| \frac{\Delta f_{\text{FM}} - \Delta f_l}{4} \right|$ , the coupling affects the linewidth for the coupled state, which reads

$$\Delta f_{\text{R}} = \frac{\Delta f_{\text{FM}} + \Delta f_l}{2} \pm \sqrt{\left( \frac{\Delta f_{\text{FM}} - \Delta f_l}{2} \right)^2 - 4K_l^2}. \quad (\text{A.17})$$

With assumption of the weak FM-QLA coupling, A.17 finally gives

$$K_{\text{QLA}} = \frac{1}{2} \sqrt{(\Delta f_{\text{R}} - \Delta f_{\text{QLA}})(\Delta f_{\text{FM}} - \Delta f_{\text{R}})}, \quad (\text{A.18})$$

where  $\Delta f_{\text{R}}$  is the spectral width of the line at the resonance  $f = f_{\text{FM}} = f_{\text{QLA}}$ .

## A.6 Polarization Dependence of the Reflection Signal

Figure A.6 presents polarization dependent reflection measurements. The figure shows spectral amplitudes measured for different polarization angles of the linearly polarized probe beam and the grooves of the nanograting. A zero polarization angle corresponds to a polarization parallel to the grooves. The black dots correspond to measured spectral amplitudes of the acoustic mode at 13.1 GHz (QTA mode) at a magnetic field of 0 mT. It is clearly see that a parallel alignment (zero angle) results in a small contribution to the reflection signal, while a perpendicular alignment results in a strong contribution<sup>2</sup>. Hence, a parallel alignment of the probe beam's polarization is preferred for PMOKE measurements, where a small contribution by the reflection signal is wanted. The perpendicular alignment is preferred for reflection measurements in order to get a maximum contribution by the acoustic modes. In order to show the symmetry of the polarization effect a regression using a sine-function is performed. The red dots correspond to the acoustic mode at 14.6 GHz (QLA mode). In order to investigate its probe polarization dependence a magnetic field of 140 mT is applied (see figure 5.10 on page 82). This polarization dependence shows a fourfold-symmetry instead of a twofold symmetry, as it is observed for the QTA mode. The difference in their dependences may be due to their specific polarizations.

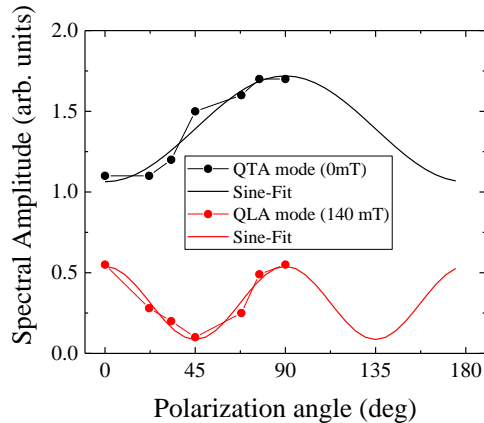


**Figure A.6:** Probe polarization dependence of reflection spectra in a shallow 7 nm-deep NG. The regressions are performed using sine functions.

<sup>2</sup>The same behaviour is also observed for non-zero magnetic fields.